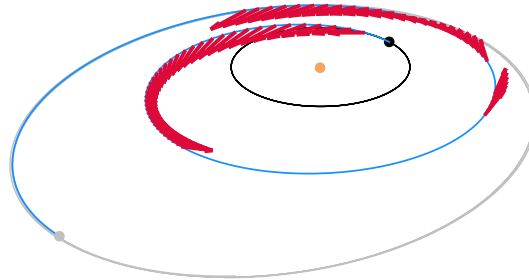




**TÉCNICO**  
LISBOA



**POLITECNICO**  
**DI TORINO**



## **Solar Electric Propulsion Transfers Optimization**

Application to The Comet Interceptor Mission Transfer

**Henrique Rego Costa**

Thesis to obtain the Master of Science Degree in

**Aerospace Engineering**

Supervisors: Prof. Lorenzo Casalino  
Prof. Paulo Jorge Soares Gil

### **Examination Committee**

Chairperson: Prof. José Fernando Alves da Silva  
Supervisor: Prof. Paulo Jorge Soares Gil  
Member of the Committee: Prof. Pedro Tiago Martins Batista

**January 2021**

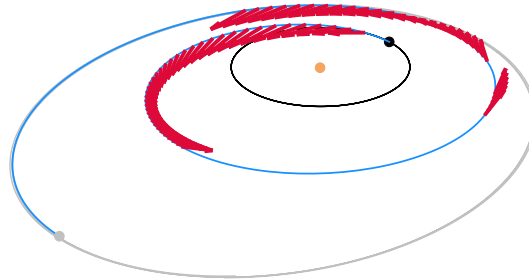




**TÉCNICO**  
LISBOA



**POLITECNICO**  
**DI TORINO**



## **Solar Electric Propulsion Transfers Optimization**

Application to The Comet Interceptor Mission Transfer

**Henrique Rego Costa**

Thesis to obtain the Master of Science Degree in

**Aerospace Engineering**

Supervisors: Prof. Lorenzo Casalino  
Prof. Paulo Jorge Soares Gil

### **Examination Committee**

Chairperson: Prof. José Fernando Alves da Silva  
Supervisor: Prof. Paulo Jorge Soares Gil  
Member of the Committee: Prof. Pedro Tiago Martins Batista

**January 2021**



To Miguel, Rita, Francisco and Inês



## Acknowledgments

I am grateful to Victor for his time and helpful — and always sharp — insights; Professor Paulo Gil for his enthusiastic lessons and his remarkable — and contagious — attention to detail, *O Pequeno Livro da Dissertação* should be read by every student before starting a dissertation; Prof. Lorenzo Casalino for triggering my interest in Electric Propulsion with his passionate classes in Politecnico and for accepting to be my supervisor remotely. I would also like to thank Francisco Cabral and João Branco for making a place for me at GMV Spain.

To my closest friends — Rita Soares, Francisco Aveiro, Inês Almeida, João Coelho, João Franco, João Moita, Rita Costa and Zeno Pavanello — my gratitude for being the best buddies I could ever wish for.

To Beatriz Rodrigues, for being my family away from home. To Inês, for showing me that the good things in life are in the small details. And to my family — Miguel, Rita and Francisco — for your unconditional love and support: you always knew I would not be an architect.



## Resumo

Os benefícios dos sistemas de Propulsão Eléctrica Solar já foram estabelecidos por missões como a Deep Space 1 e a Hayabusa; sistemas deste tipo são frequentemente considerados ao nível preliminar do planeamento de missões espaciais interplanetárias. À necessidade de pôr em prática métodos eficientes de comparação das múltiplas opções tecnológicas disponíveis, este trabalho responde com uma aplicação de optimização de trajectórias de impulso contínuo capaz de realizar análises comparativas ao nível dos sistemas de propulsão. O problema de optimização de trajectórias de impulso contínuo é formulado como um problema de Controlo Óptimo resolvido através de uma transcrição para um problema de Programação Não Linear. As ferramentas básicas do programa são utilizadas para o desenho de uma trajectória para um alvo secundário da missão Comet Interceptor. A aplicação é posteriormente estendida ao caso invulgar da trajectória principal da missão Comet Interceptor: a missão não tem um alvo definido até à data de lançamento. As possíveis posições de um encontro com o alvo principal são parametrizadas de forma a mapear cada localização a um valor de  $\Delta v$  necessário para a alcançar. De seguida, os resultados são comparados com dados da performance esperada de um sistema de propulsão impulsiva. A comparação estabelece a superioridade de um sistema de Propulsão Eléctrica Solar na óptica da maximização simultânea da massa útil da nave espacial e do número de posições alcançáveis para o encontro com o alvo.

**Palavras-chave:** Propulsão Eléctrica Solar, Optimização de Trajectórias, Análise de Missões Interplanetárias, Comet Interceptor



## Sommario

I benefici che la propulsione elettrica solare porta alle missioni interplanetarie sono stati stabiliti da missioni quali Deep Space 1 e Hayabusa tanto che ad oggi questa tecnologia è spesso presa in considerazione durante le prime fasi di design di una missione. In questo lavoro si indaga la necessità di confrontare diverse opzioni tecnologiche al livello di Preliminary Mission Design attraverso lo sviluppo di un software per l'ottimizzazione di traiettorie capace di compiere studi di trade-off a livello di sistema. Il problema dell'ottimizzazione di traiettorie a bassa spinta viene formulato come Problema di Controllo Ottimale e risolto tramite la traduzione in un problema di Programmazione Non Lineare. L'applicazione richiede un input minimale da parte dell'utente per quanto riguarda le caratteristiche della missione e usa un modello approssimato di traiettoria per generare stime iniziali per le variabili del Problema di Controllo Ottimale. Il software viene utilizzato per il design della traiettoria preliminare della missione Comet Interceptor. Il trasferimento supportato da energia solare verso una cometa di riserva e opzioni alternative al sistema di propulsione elettrica di riferimento sono studiati grazie alle capacità di base del programma. Il software è poi ampliato in modo da poter trattare le caratteristiche uniche del design preliminare della traiettoria della missione Comet Interceptor: fino a quando il veicolo spaziale non sia stato lanciato, non sarà possibile sapere quale sia di preciso la cometa bersaglio principale. I possibili luoghi di incontro vengono parametrizzati in modo da essere mappati a seconda del  $\Delta v$  richiesto dalla Propulsione Elettrica Solare. I risultati sono poi confrontati con dati disponibili dalle prestazioni del sistema di riferimento a Propulsione Chimica, stabilendo la superiorità del sistema a Propulsione Elettrica Solare nel massimizzare sia la massa del payload che la distanza delle posizioni raggiungibili.

**Parole Chiave:** Propulsione Elettrica Solare, Ottimizzazione di Traiettoria, Analisi di Missione Interplanetaria, Comet Interceptor



## Abstract

The benefits of Solar Electric Propulsion for interplanetary missions have been established by missions such as Deep Space 1 and Hayabusa and the technology is now frequently considered at early mission design phases. The need to compare multiple technological options at a preliminary mission design stage is addressed in this work through the development of a trajectory optimization software capable of performing trade studies at a system level. The low thrust trajectory optimization problem is formulated as an Optimal Control Problem solved after a direct transcription into a Nonlinear Programming Problem. The software is exploited for the preliminary trajectory design of The Comet Interceptor Mission. A solar powered transfer to a backup target and alternative options to the reference propulsion system are studied with the baseline capabilities of the program. The software is then extended to handle the unique characteristics of the preliminary trajectory design of the Comet Interceptor Mission: the primary target comet will not be known until after the spacecraft is launched. The possible encounter locations are parametrized to map each location to a required  $\Delta v$  to reach it with Solar Electric Propulsion. The results are then compared to available performance data for the Chemical Propulsion baseline system, establishing the superiority of the Solar Electric Propulsion option in maximizing both payload mass and reachable locations.

**Keywords:** Solar Electric Propulsion, Trajectory Optimization, Interplanetary Mission Analysis, Comet Interceptor



# Contents

Acknowledgments . . . . .	vii
Resumo . . . . .	ix
Sommario . . . . .	xi
Abstract . . . . .	xiii
List of Tables . . . . .	xvii
List of Figures . . . . .	xix
Nomenclature . . . . .	xxi
Glossary . . . . .	xxv
<b>1 Introduction</b>	<b>1</b>
1.1 Solar Electric Propulsion . . . . .	1
1.2 Review of Trajectory Optimization Methods . . . . .	2
1.2.1 Optimal Control Problem . . . . .	3
1.2.2 Initial Guess Generation . . . . .	4
1.3 Motivation . . . . .	6
<b>2 The Comet Interceptor Mission</b>	<b>7</b>
2.1 Target Comets . . . . .	8
2.2 Mission Timeline . . . . .	8
2.3 Transfer From SEL2 to Comet . . . . .	9
2.3.1 Transfer Geometry . . . . .	9
2.3.2 Transfer Dynamics . . . . .	10
2.3.3 Spacecraft and Propulsion System Assumptions . . . . .	12
<b>3 Methods and Models</b>	<b>15</b>
3.1 Solar Electric Propulsion . . . . .	15
3.1.1 Engine Model . . . . .	16
3.2 Interplanetary Transfers . . . . .	17
3.3 Optimal Control Problem . . . . .	17
3.3.1 Transcription to a Nonlinear Programming Problem . . . . .	19
3.4 Initial Guess Generation . . . . .	22
3.4.1 Grid Search Algorithm . . . . .	22

3.4.2	Describing the Trajectory Path with Chebyshev Polynomials . . . . .	22
3.4.3	Initial Guess Selection Policy . . . . .	26
3.4.4	Computing the Initial Guess Control Profile . . . . .	27
<b>4</b>	<b>Implementation</b>	<b>29</b>
4.1	External software . . . . .	29
4.2	Architecture . . . . .	30
4.2.1	Command Line Interface . . . . .	30
4.2.2	Software Modes . . . . .	32
4.3	Software Validation . . . . .	34
4.3.1	Comet Rendezvous Mission . . . . .	35
4.3.2	Near-Earth Asteroid Flyby Mission . . . . .	36
<b>5</b>	<b>Application to The Comet Interceptor Mission Transfer</b>	<b>39</b>
5.1	Probing Encounter Locations . . . . .	40
5.1.1	Selected transfers . . . . .	43
5.1.2	Comparison with Chemical Propulsion transfers . . . . .	46
5.1.3	Full Engine Capacity . . . . .	50
5.2	Transfer to backup target 73P/Schwassmann-Wachmann . . . . .	50
5.3	Trade Studies . . . . .	55
5.4	Discussion . . . . .	59
<b>6</b>	<b>Conclusions</b>	<b>63</b>
	<b>Bibliography</b>	<b>65</b>
<b>A</b>	<b>Trajectory Optimization Mode outputs</b>	<b>73</b>
<b>B</b>	<b>CRoMA data</b>	<b>76</b>
<b>C</b>	<b>Coefficients for the Engine Models</b>	<b>78</b>

# List of Tables

2.1	CReMA assumptions for detailed EP transfers analysis for backup targets. . . . .	13
2.2	Propulsion system reference design point at 1 au. . . . .	13
4.1	Kopff rendezvous scenario configuration. . . . .	35
4.2	Kopff scenario validation results. . . . .	35
4.3	Didymos flyby scenario configuration. . . . .	36
4.4	Didymos scenario validation results. . . . .	37
5.1	Trajectory Optimization Assumptions for the Comet Interceptor EP analysis. . . . .	39
5.2	Unfeasible encounter locations for 1-revolution trajectories. . . . .	42
5.3	Overall comparison of EP against CP. . . . .	49
5.4	Feasible trajectories for 73P. . . . .	52
5.5	0-revolution transfers from the CReMA (CR) and best LowWiz solution (L). . . . .	52
5.6	1-revolution transfers from the CReMA (CR) and best LowWiz solution (L). . . . .	54
5.7	Considered engines data for the engine trade study. . . . .	55
5.8	Minimum propellant mass savings for the different engines compared to the baseline option (neglecting Earth's gravity). . . . .	57
C.1	Engine Model Coefficients: Mass Flow . . . . .	78
C.2	Engine Model Coefficients: Thrust . . . . .	78
C.3	Engine Model: Minimum and Maximum Power . . . . .	78



# List of Figures

2.1	Comet Interceptor preliminary design for the three spacecraft. Image from ESA's Concurrent Design Facility (CDF) study for the mission. . . . .	7
2.2	Sketch of The Comet Interceptor Mission phases. The spacecraft trajectory is in green and the comet trajectory in red [51]. . . . .	9
2.3	Transfer geometry (not-to-scale) defining the departure (SEL2) and arrival positions. $R_c$ and $\vartheta$ define the encounter location relative to Earth. . . . .	10
2.4	SEL2 unstable manifolds. The Earth (blue dot) and SEL2 (purple dot) are shown in the Sun-Earth rotating frame of reference. The interior, Earth-bound manifold is in blue and the exterior manifold in red. Courtesy of GMV and ESA. . . . .	11
2.5	Sketch of the Moon flyby strategy. There is the possibility of two encounters with the Moon to modulate the Earth escape velocity, $v_\infty$ : encounter with the Moon in I or in II. . . . .	12
3.1	Polynomial model of the PPS 1350-G engine [56]. . . . .	16
3.2	Sims-Flanagan transcription [29]. . . . .	20
4.1	LowWiz architecture. . . . .	31
4.2	LowWiz Command Line Interface Logic . . . . .	31
4.3	Earth to Didymos transfer $\Delta v$ contour (Pork-Chop Diagram). A transfer to Didymos presents low $\Delta v$ ( $\Delta v < 1 \text{ km s}^{-1}$ ) opportunities over the entire launch window if the time-of-flight, $\Delta t$ , is allowed to vary between 200 d and 1000 d. . . . .	32
4.4	Engine Trade Studies mode output example. . . . .	33
4.5	Input Power Trade Studies mode output example. . . . .	34
4.6	Interplanetary transfer to the comet Kopff in the Heliocentric Earth Ecliptic reference frame. . . . .	35
4.7	Thrust magnitude profile for an interplanetary transfer to the comet Kopff. The available maximum thrust varies with the spacecraft to Sun distance. . . . .	36
4.8	Interplanetary transfer to Didymos in the Heliocentric Earth Ecliptic reference frame. . . . .	37
5.1	Results for a LowWiz run searching for 1-revolution trajectories with the Moon Flyby approach: not all the search grid points are reachable with a 1-revolution transfer. . . . .	40
5.2	0-revolution propellant mass map for EP transfers. Dir are direct transfers; MGA are Moon Gravity Assist transfers. . . . .	41

5.3	1-revolution propellant mass map for EP transfers. Dir are direct transfers; MGA are Moon Gravity Assist transfers. . . . .	42
5.4	2-revolution propellant mass map for EP transfers. Dir are direct transfers; MGA are Moon Gravity Assist transfers. . . . .	43
5.5	3-revolution propellant mass map for EP transfers. Dir are direct transfers; MGA are Moon Gravity Assist transfers. . . . .	43
5.6	Selected EP transfers (lowest propellant mass trajectory is selected for each $R_c-\vartheta$ pair). Dir are direct transfers; MGA are Moon Gravity Assist transfers. . . . .	44
5.7	Selected EP transfers (lowest time-of-flight trajectory is selected for each $R_c-\vartheta$ pair). Dir are direct transfers; MGA are Moon Gravity Assist transfers. . . . .	45
5.8	CP vs EP propellant mass comparison for minimum propellant mass trajectories. . . . .	47
5.9	CP vs EP time-of-flight comparison for minimum propellant mass trajectories. . . . .	48
5.10	CP vs EP propellant mass comparison for minimum time-of-flight trajectories. . . . .	48
5.11	CP vs EP time-of-flight comparison for minimum time-of-flight trajectories. . . . .	49
5.12	Comparison between baseline engine power and engine at full capacity (positive values are a decrease in the quantities for the engine at full capacity system). . . . .	50
5.13	$\Delta v$ contour for candidate trajectories for a 73P transfer. . . . .	51
5.14	Thrust profile for minimum $\Delta v$ transfer for 73P . . . . .	53
5.15	Minimum $\Delta v$ trajectory for a 73P transfer. . . . .	53
5.16	Best 1-revolution solution found with LowWiz. . . . .	54
5.17	Thrust profile for minimum $\Delta v$ transfer for 73P . . . . .	55
5.18	Engine trade study output (neglecting Earth's gravity). . . . .	56
5.19	Engine trade study output (considering Earth's gravity). . . . .	57
5.20	Trade study trajectories for the baseline engine (thrust arcs in red). . . . .	58
5.21	Propellant mass vs. Available input power at 1 au for different time-of-flight trajectories. . .	59
A.1	Earth to Kopff transfer. . . . .	73
A.2	Earth to Kopff transfer (3D). . . . .	74
A.3	Control profile for a transfer to Kopff. . . . .	74
A.4	Required power profile for a transfer to Kopff. . . . .	75
B.1	Selected CP transfers. . . . .	76
B.2	Selected CP transfers. Data from the CReMA. Dir are direct transfers; MGA are Moon Gravity Assist transfers. . . . .	77

# Nomenclature

## Greek symbols

$\Delta t$  Time-of-flight

$\Delta v$  Variation in velocity

$\eta$  Chebyshev polynomial basis function

$\Gamma$  Acceleration perturbation

$\kappa$  Mass ratio

$\lambda$  Angular velocity of the primaries in the Restricted Three Body Problem

$\mu$  Standard gravitational parameter

$\nu$  True anomaly

$\Omega$  Right ascension of the ascending node

$\omega$  Argument of the periapsis

$\varphi$  Longitude in the Heliocentric Ecliptic Frame of reference

$\Theta$  Sun incidence angle

$\theta$  Latitude in the Heliocentric Ecliptic Frame of reference

$\vartheta$  Comet-Sun-Earth angle at encounter position

## Roman symbols

**a** Acceleration

*a* Orbital semi-major axis

$A_{panels}$  Solar panel area

**B** Chebyshev basis function and basis function derivative vector

*b* Chebyshev coefficient

**c** Constraints vector

$c_m$	Coefficient for the engine mass flow polynomial model
$c_t$	Coefficient for the engine thrust polynomial model
$e$	Orbital eccentricity
$\mathbf{f}$	Fitness vector
$F$	Nonlinear Programming Problem objective function
$G$	Gravitational constant, $6.674\,08 \times 10^{-11} \text{ m}^3 \text{ kg}^{-1} \text{ s}^{-2}$
$g_0$	Standard acceleration due to gravity, $9.806\,65 \text{ m s}^{-2}$
$G_{SC}$	Solar constant, $1362 \text{ W m}^{-2}$
$h$	Orbital angular momentum
$i$	Orbital inclination
$I_{sp}$	Specific Impulse
$J$	Objective function
$L$	Lagrange point
$M$	Number of coefficients in a Chebyshev polynomial
$m$	Mass
$m_p$	Propellant mass
$m_{dry}$	Spacecraft mass without propellant
$m_{wet}$	Spacecraft mass with propellant
$N$	Number of discrete points in a trajectory transcription
$n$	Number of Nonlinear Programming Problem variables
$P$	Power
$\mathbf{r}$	Position vector
$r$	Euclidean norm of the position vector
$R_c$	Radius of Comet encounter position
$s$	Number of heliocentric revolutions of a trajectory
$\mathbf{T}$	Applied thrust vector
$T$	Magnitude of the applied thrust
$\mathbf{u}$	Control vector

$v$	Orbital velocity
$v_\infty$	Escape velocity
$\mathbf{x}$	Orbital state
$x, y, z$	Cartesian components of the position vector
$x_p^-, x_p^+$	Orbital state at $t_p$ after forward and backwards propagation
$\mathbf{y}$	Nonlinear Programming problem variables vector

### Subscripts

0	Initial
1au	Refers to quantity at 1au from the Sun
$av$	Available
$coast$	Refers to a coast arc (engine off)
$E$	Refers to engine model
$f$	Final
$\odot$	Sun
$\oplus$	Earth
$SEP$	Refers to Solar Electric Propulsion
$thrust$	Refers to a thrust or powered arc (engine on)
$x, y, z$	Cartesian components

### Superscripts

$T$	Transpose
-----	-----------



# Glossary

**2BP** Two-Body Problem.

**ARIEL** Atmospheric Remote-sensing Infrared Exoplanet Large-survey.

**CDF** Concurrent Design Facility.

**CP** Chemical Propulsion.

**CR3BP** Circular Restricted Three-Body Problem.

**CReMA** Consolidated Report on Mission Analysis.

**DART** Double Asteroid Redirection Test.

**DNC** Dynamically New Comet.

**EP** Electric Propulsion.

**ESA** European Space Agency.

**GNC** Guidance, Navigation and Control.

**HOCP** Hybrid Optimal Control Problem.

**ICE** International Cometary Explorer.

**JAXA** Japan Aerospace Exploration Agency.

**JPL** Jet Propulsion Laboratory.

**LPC** Long Period Comet.

**NAIF** Navigation and Ancillary Information Facility.

**NASA** National Aeronautics and Space Administration.

**NEA** Near-Earth Asteroid.

**NLP** Nonlinear Programming.

**NumPy** Numerical Python.

**OCP** Optimal Control Problem.

**ODE** Ordinary Differential Equation.

**PaGMO** Parallel Global Multiobjective Framework for Optimization.

**PPU** Power Processing Unit.

**PRR** Preliminary Requirements Review.

**PyGMO** Python Parallel Global Multiobjective Framework for Optimization.

**PyKEP** Python Keplerian Toolbox.

**SEL2** Sun-Earth Lagrange Point 2.

**SEP** Solar Electric Propulsion.

**SFT** Sims-Flanagan Transcription.

**SLSQP** Sequential Least-Squares Quadratic Programming.

**SOI** Sphere of Influence.

**SPC** Short Period Comet.

# Chapter 1

## Introduction

In this work a fast front end tool for preliminary low thrust trajectory design is developed. Specifically, the goal is to automate the process of generating feasible trajectories in interplanetary missions with Solar Electric Propulsion (SEP). For a SEP trajectory to be feasible it must respect physical laws but also stay within a spacecraft's system limitations such as maximum engine thrust and available power. By considering system limitations, the tool is expected to be used for Solar Electric Propulsion system-level trade studies, preliminary trajectory design, as an initial guess for more refined optimizers or as an input for navigation analysis tools.

### 1.1 Solar Electric Propulsion

Deep Space 1 was the first interplanetary mission using Solar Electric Propulsion (SEP) [1]. Launched in 1998, the spacecraft's ion-thruster worked for 1800 h, providing  $700 \text{ m s}^{-1}$  of  $\Delta v$  needing only 3% of its dry mass for propellant. Numerous missions followed: Hayabusa, JAXA's bold attempt at rendezvous with an asteroid, was equipped with ion engines that provided  $2.2 \text{ km s}^{-1}$  of  $\Delta v$  using only 47 kg of propellant (12% of the dry mass) [2]; ESA's SMART-1, launched in 2003, consisted in raising the orbit of the spacecraft from a Geostationary Transfer Orbit to a Moon Orbit to test Solar Electric Propulsion for deep space applications [3]; NASA's Dawn mission took off with an Ion Propulsion System that provided an impressive  $11 \text{ km s}^{-1}$  of  $\Delta v$  which was comparable to its launch vehicle [4]; building on the accomplishments of Hayabusa, JAXA launched Hayabusa 2 in 2014 which, after successfully rendezvousing with asteroid Ryugu in 2018, returned an asteroid sample in 2020; BepiColombo is a joint effort between ESA and JAXA [5] enroute to Mercury: interestingly, BepiColombo's electric engines' maximum thrust level will increase throughout the mission, as it gets closer to the Sun and more power is available [6]. Besides deep space missions, scientific and commercial Earth Orbit missions have exploited electrical propulsion and present satellite communication systems rely on the technology [7].

Current state-of-the-art Electric Propulsion (EP) technology provides significantly less thrust when compared to Chemical Propulsion (CP) technologies: EP systems deliver thrust in the order of magnitude of mN [8] whereas CP rockets can provide up to hundreds of kN of thrust. However, EP is typically

more efficient in terms of fuel consumption when compared to high thrust CP systems because EP systems have higher specific impulse,  $I_{sp}$  [8].

Besides the difference in terms of performance, EP and CP also differ in their effect on the trajectory dynamics. In a first approximation, modelling a chemical propulsion system is unnecessary and the maneuvers are considered impulsive. The result of an impulsive maneuver is a keplerian orbit for which there is an analytical solution for elementary cases. On the other hand, electric engines work for longer periods of time given their low thrust levels. Hence, a low thrust trajectory is not a keplerian orbit. This difference means that, albeit more efficient, continuous thrust trajectories are complex to model and optimize.

The low thrust trajectory optimization problem is nonlinear and does not have an analytical closed-form solution for the general case [9]. Adding to the complexity of the problem, the trajectory and the propulsion system are coupled. For each pair of spacecraft and propulsion system, the optimal trajectory may be different and comparing different technology combinations may be a daunting task. The optimization of a trajectory includes continuous mission variables, such as date of departure, initial orbit energy, time-of-flight, thrust direction and thrust magnitude. Additionally, an optimizer may have to choose bodies to perform gravity assists and decide on the number of flybys, thus the problem might also accommodate discrete variables. There may be thousands or millions of candidate trajectories to be evaluated for a given trajectory optimization problem [10].

The complexity of the SEP trajectory optimization problem has not hindered the technology. The potential of SEP for interplanetary missions was foreseen by NASA's Deep Space 1 [11] and confirmed by numerous missions thereafter [2–5]. Naturally, more and more systems have been developed and the technology is no longer a novelty [7]. This means that numerous options are at the disposal of spacecraft developers suggesting the need for new tools to compare different systems during preliminary mission design. Such tools have to be developed in the framework of the Trajectory Optimization Problem.

## 1.2 Review of Trajectory Optimization Methods

The Trajectory Optimization Problem has drawn a great deal of attention; numerous surveys have provided insights on the evolution of the state-of-the-art in the field [12–16]. As of 2020, the topic is still relevant as new computation trends emerge, such as machine learning techniques [15], and innovative propulsion technologies are developed such as solar sails [17]. The low thrust trajectory optimization problem aims to find the trajectory path and control history that minimize a cost index while satisfying boundary conditions and following the dynamics of celestial mechanics. The dynamical system is represented by the vector set of variables: spacecraft state (position and velocity) and the control variables (applied thrust vector). Since the problem consists in finding the control profile to minimize a cost function, it is considered an Optimal Control Problem (OCP) [12].

### 1.2.1 Optimal Control Problem

The OCP can be solved analytically or numerically [14]. As there is no closed-form solution for the Trajectory Optimization OCP, analytical methods require limiting assumptions (such as tangential thrust or quasi-circular trajectories) [18–21] which may lead to disagreements between simulation and reality in spacecraft motion. Nonetheless, analytical methods provide useful insights when solving OCPs. Numerical methods can be grouped into indirect, direct and stochastic methods [12, 14].

Indirect methods exploit the calculus of variations [22] to derive the optimality conditions of the problem and find the root of the resulting equations. The resulting equations require that a set of parameters known as Lagrange Multipliers, or co-states, are found such that they ensure the optimality of the solution. Within this framework, emerged the primer vector theory [23, 24]: the co-states provide the optimal thrust direction and magnitude and the optimal coast-thrust-coast structure; for the majority of the problems the optimal control profile is bang-bang, i.e., the engine is either off or at its maximum power. Despite the utility of the co-states in finding the optimal control function, they have no physical meaning. Additionally, to start the root solving algorithm, an initial guess must be generated for the co-states. Generating an initial guess for the co-states is not a trivial task hence some of the previous work focused on this problem [25, 26]. Existing work in the field of indirect trajectory optimization [23–26] discretizes the optimality conditions and employs Nonlinear Programming (NLP) solvers to find the solution. Despite ensuring the optimality of the solution, indirect methods suffer from two hindering limitations. First, the problems have small regions of convergence and are very dependent on the initial guess [12]. Secondly, indirect methods need analytical expressions for the optimality conditions that have to be derived explicitly for each specific problem, thus being less versatile than direct methods [27, 28].

Contrarily to indirect methods, direct methods do not involve the derivation of analytical optimality conditions. Consequently, the direct approach easily involves a broad number of constraints and is preferred for trade study analysis [27], where multiple mission scenarios are to be assessed. A direct method transforms the continuous optimal control problem into a discrete Nonlinear Programming Problem [28]; the optimization parameters are the control variables at a finite number of nodes and in some cases the trajectory states. The baseline direct approach — often referred to as Sims-Flanagan Transcription (SFT) — divides the trajectory into multiple legs with a finite number of nodes where maneuvers are considered impulsive [29, 30]. The dynamic system equations are integrated stepwise and the constraints appear as nonlinear equations or inequalities. The Sims-Flanagan Transcription can then be formulated as a NLP Problem to find the locally optimal trajectory and control profile [31–35]. The Sims-Flanagan Transcription was exploited and extended by previous work: a combination of a NLP solver with a globalization algorithm — Monotonic Basin Hopping — was employed to avoid convergence to local minima [31, 32]; the assumption of impulsive maneuvers at the control nodes was exchanged for the assumption of constant thrust between nodes for higher fidelity results [34]; the higher fidelity Sims-Flanagan Transcription [34] was used in a target search for a small Solar Electric Propulsion spacecraft mission leaving the Sun-Earth Lagrange Point 2 (SEL2) [35]. A direct method does not ensure the optimality of the solution but it has been found that these methods are able to converge to bang-bang solutions [23]. Nonetheless, direct methods are not without its shortcomings: the NLP solver can get

stuck at a local minimum; direct methods are hampered by the large number of NLP variables as more accuracy is desired. The direct approach does not require any guess for the co-states but it does require so for the states and control variables.

The indirect and direct numerical methods that exploit NLP solvers are considered gradient-based solvers. A third numerical approach exploits stochastic optimization methods. A stochastic method relies on meta-heuristic processes: these algorithms randomly select values for the problem variables and define decision-making policies to find the best solution. Stochastic methods are particularly useful for problems with discrete variables [12] such as multiple gravity assist trajectory optimization problems: these problems cannot be solved by calculus based methods and comparing all the possible solutions is prohibitive, hence the use of stochastic methods [14]. Meta-heuristics are attractive because the underlying algorithms ignore the dynamics of the problem and only compare stochastic solutions until the maximum number of iterations is reached. However, for problems where a gradient is available, calculus based methods typically converge faster [12].

Regardless of the numerical method used to solve the problem, the continuous OCP has to be transcribed into a discrete form. The transcription techniques typically used, single shooting or multiple shooting, are compared in [28]. The single shooting technique parametrizes the controls leaving the trajectory states as an implicit function of the controls. The trajectory is propagated from the initial to the final time instant and the error or defect at the final boundary condition is brought to zero [36]. A single shooting transcription requires fewer parameters when compared to multiple shooting but a small change in the initial conditions can generate large changes in the the final conditions. As a result the constraint equations are very nonlinear and difficult to solve [12]. The nonlinear effects that hinder the single shooting technique are dealt with by the multiple shooting technique. The multiple shooting technique parametrizes both the control profile and the trajectory states: the problem's time domain is broken into smaller segments and continuity constraints are enforced at the boundary of each segment [28]. Although the added constraints in the multiple shooting transcription increase the problem size they reduce the problem's sensitivity with respect to single shooting.

The three numerical methods considered in this work can be grouped into gradient-based methods (direct and indirect) and stochastic methods (meta-heuristics). Despite their differences, these methods are complementary as recent work in Hybrid Optimal Control Problem (HOCP) algorithms proves [37–39]. The meta-heuristics approach does not require an initial guess to solve the problem, however, its superiority is limited to combinatorial problems or when a gradient is not available [12]. For gradient-based approaches, there is the need of an initial guess for the NLP variables which is typically generated using a simplified or approximate trajectory model.

## **1.2.2 Initial Guess Generation**

Approximate trajectory descriptions are useful in expediting the initial search of the design space in trajectory optimization problems [14]. The most promising trajectories can be used as an initial guess for optimal control solvers.

The need for high fidelity optimizers to be fed with initial guesses [12] and the recent trend in hybrid optimization algorithms [14, 40] has driven research on the topic of automating the trajectory generation process. When approximating a low thrust trajectory, a trade-off between fidelity and computational cost is key since meaningful results are asked for but using complex models is time consuming when evaluating multiple candidate solutions. This trade-off calls for the most accurate description with the minimum number of parameters and, if possible, using linear relations: simple numerical procedures to satisfy boundary conditions are desired. Previous research in the field can be divided into shape-based approaches and pseudospectral methods.

The shape-based approach is widely used [14]. It assumes a predetermined shape for the solution and defines shape parameters to satisfy boundary conditions [41–44]. The exponential sinusoid shape model [41] describes the trajectory in terms of the polar coordinate where four coefficients are used to satisfy boundary conditions. The inverse polynomial shape [42] extends the exponential sinusoid method adding two parameters to fully satisfy the boundary conditions for rendezvous problems. Subsequently, the spherical shaping model is successful in generating feasible three dimensional trajectories in a fast way and it was shown to be a general case of the exponential sinusoid and the inverse polynomial shape [43]. These methods have limitations inasmuch as they fail in satisfying boundary conditions such as rendezvous [41] or require assumptions regarding thrust orientation [41–43]. Moreover, all need iterative methods to define the shape parameters. Despite this, shape-based methods are successfully used to automate initial search processes in trajectory optimization problems.

A distinct yet still shape-based approach is shaping the velocity instead of the position. Hodographic shaping of the velocity is acceptable for generating feasible and near-optimal trajectories and simplifies the satisfaction of boundary conditions of other shape-based methods [44]. However, its success relies on a problem-dependent choice of basis functions to describe the velocity vector diagram.

Contrarily to shape-based methods, pseudospectral methods do not assume a shape for the solution; instead they assume that the trajectory's shape may be approximated by a series expansion of a set of global basis functions [45–49]. Pseudospectral methods are interpolatory methods used to solve differential equations for an unknown function [50]. In particular, Finite Fourier Series are suitable for fast trajectory generation: a method to handle thrust constraints concurrently with the generation of candidate trajectories was developed for the two dimensional case [45, 46] and three dimensional case [47]. The technique was shown to be flexible in generating different trajectories both comparable and different to state-of-the-art shape-based methods [47]. Chebyshev polynomials were found to be flexible in approximating different continuous thrust trajectories [48, 49]. In particular, a self-contained method to autonomously search for candidate trajectories was developed, eliminating the need for initial guesses of the series' coefficients. Also, to satisfy the problem's boundary conditions, the work in [49] required only the solution of a linear algebraic set of equations.

These methods were not developed having thrust constraints satisfaction capabilities in mind; only the Finite Fourier Series method [45–47] incorporates the thrust constraints when computing the terms of the Fourier Series. Their shortcomings are the need for initial guesses for the series' coefficients and the degrading of the technique for difficult problems such as high eccentricity and high inclination

change transfers [45–47].

Overall, previous attempts of automating trajectory generation using approximate trajectory models were successful. Advances on the topic have been exploited for inner loops of hybrid optimization algorithms [31, 32, 39] or used to feed medium to high fidelity optimizers to solve for feasible thrust profiles [41, 43, 49]. A proof of concept framework for evaluating different SEP systems [48, 49] ensures the potential of the work done so far.

### 1.3 Motivation

This MSc Thesis exploits existing approximate trajectory models coupled with a NLP solver to parametrically evaluate different Solar Electric Propulsion technologies. A tool is developed that allows mission analysts to compare the benefits and costs of different trajectory, thruster and power system combinations. The software shall be able to efficiently cope with the obstacles of the continuous propulsion trajectory optimization problem: nonlinear system dynamics, possible discontinuities in the state variables, presence of time-dependent forces, boundary conditions often being optimization variables, and the structure of the solution not being known beforehand [9].

Additionally, this work was instigated by the need to reduce the computational cost of preliminary trajectory design while including system level constraints at an early stage of mission analysis. This need is in contrast with the coupling between trajectory and propulsion system: a different trajectory optimization problem has to be solved for different systems, slowing down the process of preliminary trade studies. The software shall be able to efficiently evaluate multiple SEP technologies.

A further aim of this work is to reduce the workload of mission analysis engineers in trajectory optimization problems. Low thrust trajectories require that a time-history of the control variables be specified to perform an orbit transfer in addition to the specification of variables such as date of departure, time of flight and initial orbit energy. To eliminate the need for analysts to possess *a priori* knowledge regarding the structure of the solution the tool shall only need a parametric mission description as an input.

However, not all interplanetary missions fit into a general parametric mission description and this should not hinder the software: the implementation of the tool must also be flexible and extensible. Specifically, the software shall be used for a preliminary trajectory design of the Comet Interceptor Mission [51]. The Comet Interceptor trajectory in particular cannot be designed with a generic parametrization valid for other missions: until the launch the mission may not have a known target.

This called for the implementation of a fast, flexible and extensible tool, named LowWiz, with a dual purpose: capability of providing feasible trajectories sufficiently accurate for trade studies while being compatible with higher fidelity optimizers, hybrid optimization algorithms and navigation analysis tools.

## Chapter 2

# The Comet Interceptor Mission

Previous comet exploring missions have studied Short Period Comets (SPCs) (orbital period  $< 200$  years): ICE performed a flyby of 21P/Giacobini–Zinner in 1985; Giotto visited the Halley comet in 1986 and 26P in 1990; in 2014, Rosetta notably met 67P/Churyumov-Geramisenko. The success of these and other missions to comets has returned large amounts of data that in 2020 is still generating new results on the field of cometary physics [52]. The study of SPCs, has advanced our knowledge about the formation of the solar system [53]. However, SPCs suffer from large transformations as a result of multiple revolutions around the Sun — the comets are warmed by the Sun and release gases forming the coma and in some cases a tail. The Comet Interceptor plans to be the first mission to visit a Dynamically New Comet (DNC) [51] — one that, by definition, is visiting the inner Solar System for the first time.

The Comet Interceptor's primary objective is to characterize the morphology, composition, and plasma environment of a relatively unprocessed comet. Specifically, the mission aims to determine the bulk composition of the nucleus' surface, assess the molecular composition of the coma and the structure of boundaries and regions in the plasma environment of a comet.

To fulfill its objective, the mission will be composed of three spacecraft. The three spacecraft, sketched in Figure 2.1, will be launched together and will separate before the encounter with the comet.

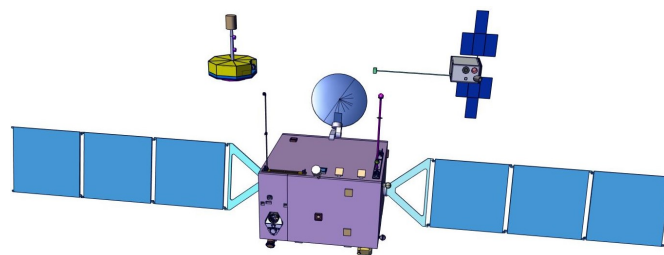


Figure 2.1: Comet Interceptor preliminary design for the three spacecraft. Image from ESA's Concurrent Design Facility (CDF) study for the mission <sup>1</sup>.

A comprehensive briefing on the objectives and all the guidelines for the mission analysis tasks are established by the Comet Interceptor CReMA <sup>2</sup>.

<sup>1</sup><https://www.cosmos.esa.int/web/comet-interceptor/mission-status>, last accessed on August 28th, 2020

<sup>2</sup>Comet Interceptor Consolidated Report on Mission Analysis, Courtesy of GMV and ESA.

## 2.1 Target Comets

The mission aims to visit a DNC. DNCs are Long Period Comets (LPCs) (period  $> 200\text{yr}$ ) with hyperbolic orbits and eccentricity close to 1 — therefore visit the inner Solar System. DNCs have yet to visit the inner part of the Solar System and thus are preserved ever since their constitution which is presumed to have been in the age of planetary formation. Consequently, DNCs are thought to be pristine objects containing crucial information to understand the origins of the Solar System [54].

DNCs are comets that have not been closely seen before: historically, they have been detected just a few months to a few years before their perihelion. However, an attractive target DNC is expected to be found in the 2020 decade and the likely time interval between the detection and perihelion passage of the target is five years [51].

The impromptu nature of DNCs — detected very shortly before their closest passage to the Sun — is incompatible with the typically long time frames for space mission design. The Comet Interceptor mission and spacecraft will have to be designed, and may be even launched, without a known target.

The unusual challenges of designing a mission for an unknown destination impacts the mission analysis and spacecraft design. To overcome the difficulties posed by the uncertainty in the encounter location, a parametric formulation to guide the study of transfers to different destinations was devised in the CReMA and explained in the Transfer Geometry Section 2.3.1.

### Backup Targets

Aside from the analysis to possible comet encounter locations, the mission analysis must consider the event of not finding a suitable target in time. A probabilistic reachability analysis was made in the CReMA relating the required  $\Delta v$  and mission duration with the probability of encountering at least one Long Period Comet during the mission timeframe: the baseline version of the mission yields a probability of 81 % of finding a Long Period Comet and 48 % of finding a DNC.

To cope with a scenario where a suitable target is not found, sixty-seven backup targets are identified in the CReMA. The list is cut down to ten and a request for community observations is issued in [55] to help in the prioritization of the backup targets.

In the CReMA, CP transfers are analyzed for the targets highlighted in [55]. Detailed EP transfers are optimized only for one backup target: 73P/Schwassmann-Wachmann.

## 2.2 Mission Timeline

The mission phases are sketched in Figure 2.2. The launch is scheduled for 2028 towards SEL2 where the spacecraft will wait in a parking orbit before starting a transfer to its target comet.

The launch will be on-board an Ariane 62 in a dual launch configuration with the Atmospheric Remote-sensing Infrared Exoplanet Large-survey (ARIEL) M4 mission as primary payload and the Comet Interceptor spacecraft as a secondary payload. After launch the two spacecraft will head towards SEL2 where the Comet Interceptor will wait for its target comet.

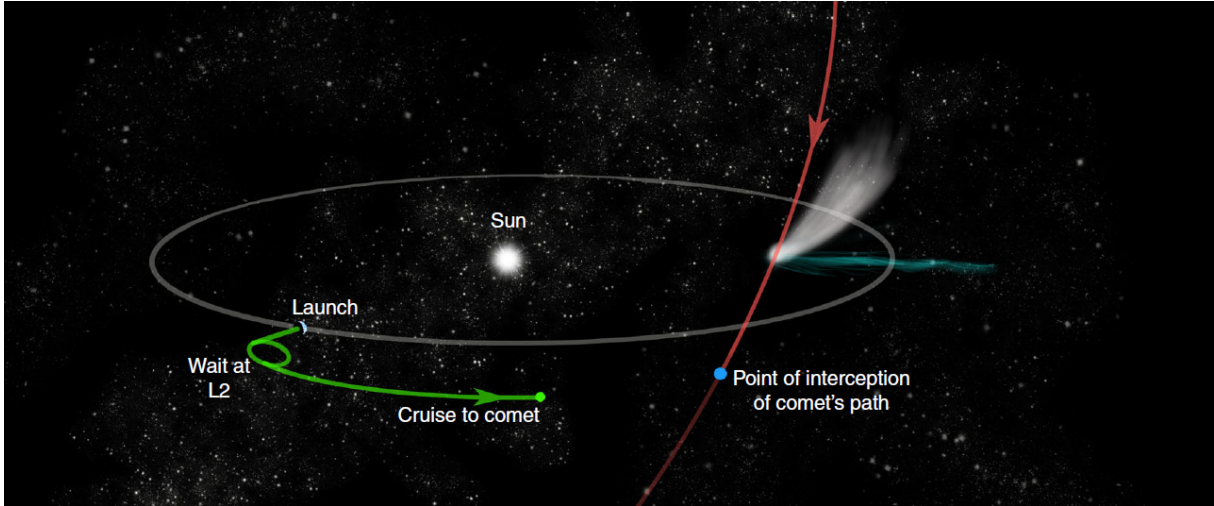


Figure 2.2: Sketch of The Comet Interceptor Mission phases. The spacecraft trajectory is in green and the comet trajectory in red [51].

The waiting phase in SEL2 will take up to three years. A parking orbit in SEL2 is suitable for the mission: it is cheap to maintain in terms of  $\Delta v$  and can provide favourable departure conditions for a transfer to the encounter. The spacecraft will leave the parking orbit at the optimal date to initiate the transfer from SEL2 to the encounter.

The transfer from SEL2 to the encounter is dependent on the encounter location and might take between six months and four years. This phase of the mission ends with the approach to encounter (30 d to 60 d before the flyby) and the encounter itself where the three spacecraft that compose the Comet Interceptor mission will separate. After the encounter, the science data gathered during the comet encounter will be transmitted by the primary.

The analysis in this work deals with the transfer from the waiting orbit at SEL2 to the target following the guidelines described in the CReMA.

## 2.3 Transfer From SEL2 to Comet

The transfer from SEL2 to the comet will be either performed by a CP system or by an EP system. The two systems require a dedicated analysis due to the distinct dynamics that apply to the respective trajectories. The mission analysis assumptions related to the transfer geometry and dynamics and spacecraft and propulsion system are detailed in Sections 2.3.1 to 2.3.3, respectively.

### 2.3.1 Transfer Geometry

The starting point of the trajectory is the SEL2. The transfer to the target is assumed to stay in the Earth Ecliptic plane to avoid inclination change maneuvers since they require prohibitive amounts of fuel. In the absence of a known target ephemeris to define the arrival point, the trajectory can be fully defined, in the Sun-Earth rotating frame of reference, by two parameters:  $R_c$  and  $\vartheta$ , the heliocentric radius and the comet-Sun-Earth angle at the encounter respectively, as in Figure 2.3. In Figure 2.3, the X-axis has

its origin in the Sun and points towards the Earth; the comet-Sun-Earth angle at encounter,  $\vartheta$ , is positive in the counter-clockwise direction. As per the CReMA specifications, the comet is said to be behind the Earth at the encounter if  $\vartheta > 0$  and ahead of the Earth if  $\vartheta < 0$ .

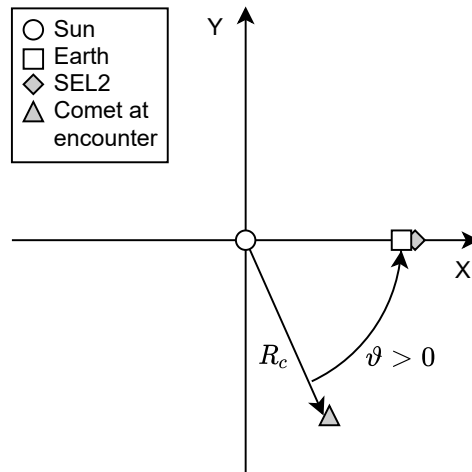


Figure 2.3: Transfer geometry (not-to-scale) defining the departure (SEL2) and arrival positions.  $R_c$  and  $\vartheta$  define the encounter location relative to Earth.

The departure from SEL2 and the two encounter parameters,  $R_c$  and  $\vartheta$ , set the trajectory in terms of initial orbital state (position and velocity of SEL2) and final position but leave the arrival velocity undefined. As specified in the CReMA, the analysis of the transfer geometries for unknown targets should consider that the spacecraft arrives at a circular orbit with heliocentric radius  $R_c$  at the moment of the encounter. Thus the arrival orbital velocity is fully defined by  $R_c$  and  $\vartheta$ : the magnitude of the velocity is given by the circular orbital speed equation,  $v_f = \sqrt{\mu_{\odot}/R_c}$ , and its direction is perpendicular to the arrival position vector and can be inferred from  $\vartheta$ .

### 2.3.2 Transfer Dynamics

The journey from the SEL2 to the comet predominantly follows the dynamics of the Two-Body Problem with the Sun as the central body. However, the SEL2 exists because the gravitational force of the Sun and the Earth cancel each other; the influence of the Earth in the initial trajectory segments should not be neglected altogether.

The effects of the Earth's gravity are mostly felt in the vicinity of SEL2. The dynamics of the Circular Restricted Three-Body Problem (CR3BP) problem can be exploited to deliver a quasi-free escape from SEL2 and insertion in the transfer orbit. An analysis of the escape from SEL2 is made in the CReMA and reported here to point out how meaningful results can be derived by studying the transfer to the comet in the simpler two-body problem with the Sun as the central body.

#### Escape from SEL2

The unstable manifold of SEL2 presents two directions in which the spacecraft will go after an infinitesimal perturbation: an interior Earth bound manifold and an exterior manifold as shown in Figure 2.4.

These SEL2 escape trajectories are reachable with only an infinitesimal  $\Delta v$ .

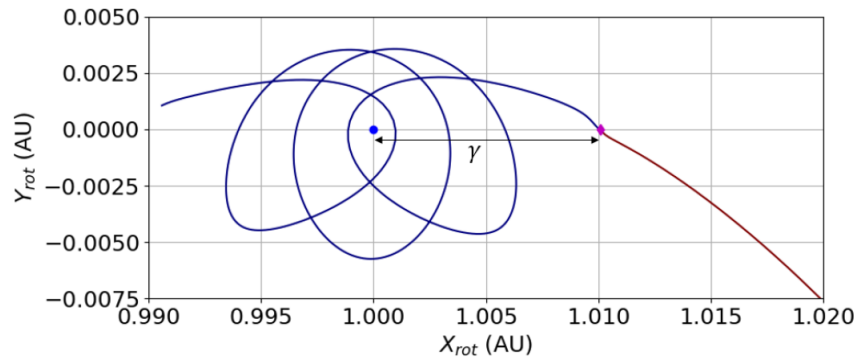


Figure 2.4: SEL2 unstable manifolds. The Earth (blue dot) and SEL2 (purple dot) are shown in the Sun-Earth rotating frame of reference. The interior, Earth-bound manifold is in blue and the exterior manifold in red. Courtesy of GMV and ESA.

The study of the SEL2 escape dynamics reached the following conclusions:

- When escaping towards the I quadrant (comet ahead of Earth at encounter  $\vartheta < 0$ )
  - Escaping radially towards the Earth implies an Earth flyby which can be exploited to provide a high ratio between the  $v_\infty$  when leaving the Earth's sphere of influence and the  $\Delta v$  needed to insert the spacecraft in the correct manifold trajectory;
  - Escaping tangentially to the Earth's velocity is efficient only for  $\Delta v > 1\text{ km s}^{-1}$  but avoids the effect of Earth's gravity;
- When escaping towards the IV quadrant (comet behind Earth at encounter  $\vartheta > 0$ ) a  $\Delta v$  parallel to the Earth's velocity at SEL2 is the most efficient way to increase the heliocentric energy — thus increasing the semi-major axis of the orbit;

### Transfer Strategies

Two transfer strategies were devised in the CReMA regarding the departure from SEL2:

- Direct transfer
  - A manoeuvre performed at SEL2 injects the spacecraft into a transfer orbit, drifting towards the encounter location;
  - In the CReMA, a first estimate for the size of the first manoeuvre is computed using the Hohmann transfer formulation between SEL2 and the encounter location. The Hohmann transfer formulation is valid in the two-body problem framework but is used with the caveat of considering the inertial velocity of SEL2 instead of the actual velocity of a spacecraft parked in SEL2 (the inertial velocity at SEL2 is  $500\text{ m s}^{-1}$  greater than the actual velocity of a spacecraft in that point). The  $500\text{ m s}^{-1}$  difference in orbital speed may be seen as a  $\Delta v$  saving when increasing the semi-major axis of the orbit and as a penalty when decreasing the semi-major

axis of the orbit. Consequently, this estimate is conservative for transfers to encounters with  $R_c > 1 \text{ au}$  and optimistic for transfers to  $R_c < 1 \text{ au}$  encounters.

- Moon Gravity Assist

- Escaping SEL2 towards an Earth bound manifold trajectory (see Figure 2.4) allows for a Moon flyby — sketched in Figure 2.5 — that can provide a  $v_\infty$  of  $1 \text{ km s}^{-1}$  to  $1.4 \text{ km s}^{-1}$  at the exit of the Earth’s sphere of influence and direction opposite to the Earth’s velocity.
- In the CReMA it is specified that “from a two-body heliocentric perspective, the Moon fly-by can be interpreted as a free deviation of the outgoing asymptote, thus modifying the outgoing infinite velocity [ $v_\infty$ ] to leave Earth;”
- The Moon Gravity Assist strategy transfers are optimized within the two-body problem dynamics and departing from the Earth’s sphere of influence with a  $v_\infty < 1.4 \text{ km s}^{-1}$  in the opposite direction of the Earth’s velocity vector. The direction of the escape velocity is fixed but its magnitude is an optimization variable with an upper bound of  $1.4 \text{ km s}^{-1}$ . Consequently, the net effect of the Earth-Moon system in the dynamics is accounted for in the Earth escape velocity.

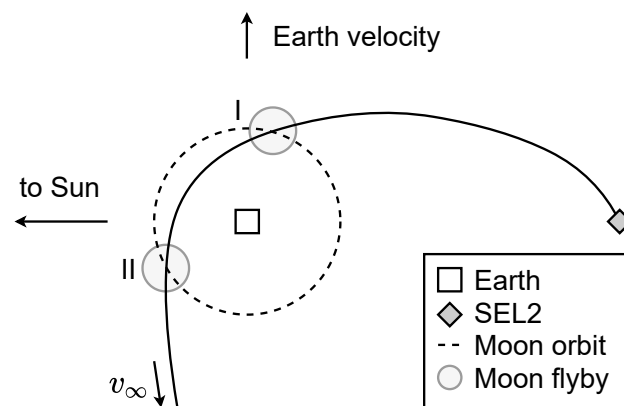


Figure 2.5: Sketch of the Moon flyby strategy. There is the possibility of two encounters with the Moon to modulate the Earth escape velocity,  $v_\infty$ : encounter with the Moon in I or in II.

This work considers the two-body problem framework using real ephemeris from the Earth and SEL2 and carefully defining the departure conditions to replicate the Earth’s gravity net effect in the trajectory efficiency. Nonetheless, the approach followed here regarding the spacecraft at a system level differed from the CReMA.

### 2.3.3 Spacecraft and Propulsion System Assumptions

Two architectures are to be considered for the interplanetary transfer propulsion system: a CP spacecraft configuration and a hybrid system with EP for the transfer to the target and CP for the close approach and flyby phases. This work studies the performance of an EP system, namely a Solar Electric Propulsion system.

In the CReMA, two sets of assumptions are used in the trajectory optimization problem — one for transfers to unknown targets and another for transfer to backup targets. For unknown targets, no detailed EP trajectories were analyzed. Instead, EP results in terms of  $\Delta v$  and time-of-flight were interpolated from the results of the CP analysis. For the backup targets, specifically 73P/Schwassmann-Wachmann, detailed EP trajectories were analysed under the assumptions in Table 2.1.

Table 2.1: CReMA assumptions for detailed EP transfers analysis for backup targets.

Constant thrust and specific impulse	
Three values for thrust to mass ratio: 0.05, 0.1 and 0.2mN kg <sup>-1</sup>	
Thrust applied to the trajectory assumes 100% duty cycle (no penalty/margin included at this stage)	
No thrust applied in the last 60-day arc prior to comet flyby. Respecting this constraint, the CReMA states the following: “[the constraint] is not implemented in the trajectory problem, but compliance has been checked a-posteriori.”	
Transfers with 2 powered arcs	

For the backup target EP transfers analysis, the CReMA uses a simplified spacecraft model (see Table 2.1). Instead, the approach followed here worked with an EP engine model (detailed in Section 3.1.1) that allowed for variable thrust and specific impulse. The CReMA specifies a reference design point for the propulsion system at 1 au based on a single PPS1350 engine and reported in Table 2.2.

Table 2.2: Propulsion system reference design point at 1 au.

Thrust (mN)	40
Specific Impulse (s)	1219
Input power to PPU (W)	800

A model of the PPS1350 engine was available from ESA’s SMART-1 mission [56]. At its 800 W operating point, the PPS1350 engine provides 40 mN of thrust and 1220 s of specific impulse, in agreement with the reference design point in Table 2.2. The available power to the Power Processing Unit (PPU) is 800 W at 1 au and proportional to  $1/r^2$  with  $r$  the distance to the Sun.

The reference value for spacecraft mass is the wet mass which is constrained by the launcher capabilities and by the primary payload (ARIEL spacecraft). The allocated launch mass for the Comet Interceptor spacecraft is 750 kg. Besides the constraints at the propulsion system level, the CReMA specifies a constraint on the thrusting program: there should be a coast-arc (no thrust) of at least sixty days before the flyby for optical navigation purposes.

The Comet Interceptor mission is in its mission design Phase A where feasibility is assessed and requirements are specified culminating with the Preliminary Requirements Review (PRR). At this stage, the spacecraft propulsion system is subject to trade-off and optimization. In this work, the study of a Solar Electric Propulsion transfer is presented in terms of required propellant mass, time-of-flight and thrusting program.



# Chapter 3

## Methods and Models

### 3.1 Solar Electric Propulsion

Solar Electric Propulsion systems exploit electrical energy supplied by solar arrays to accelerate propellant and generate a net thrust on the spacecraft. The physics of Electric Propulsion are not the subject of this thesis, however, an overview of the different technologies is briefly provided for the sake of completeness. The underlying physical principles for electrical engines varies depending on the technology: electrical engines are typically grouped into electrothermal, electrostatic and electromagnetic [57].

Electrothermal engines electrically heat propellant gas which is then expanded through a nozzle where its thermal energy is converted into kinetic energy. For thermal engines, the attainable exhaust velocity (and consequently the specific impulse) is limited mainly by the maximum temperature tolerated by the system's materials and by the thermodynamic properties of the gas. To evade the thermal limitations of electrothermal systems, electrostatic engines exploit electrostatic fields: an electric field established between the source of ions and a negative grid electrode accelerates a beam of positive charged ions. The exiting exhaust speed of the gas is limited by the potential drop between the source and the exit electrode, by the charge-to-mass ratio of the ions and by the space-charge limitation on the mass flow density defined by Child's law [58]. To circumvent the limitations posed by Child's law, electromagnetic engines require no macroscopic net-charge to accelerate gas. The working principle differs depending on how the magnetic field is generated and if the engine works with steady or unsteady flows; steady flow engines use neutral ionized gas and thus are often designated as plasma thrusters. The free electrons in the plasma, in attempting to follow the applied electric field, are turned by the magnetic field towards the direction of the flow. Subsequently, these electrons transfer momentum to the ions in the neutral gas. Unsteady flow thrusters exploit transient magnetoplasma dynamic effects to improve the efficiency relative to steady flow engines. Lastly, standing between electrostatic and electromagnetic engines, Hall effect thrusters exploit a radial magnetic field to accelerate electrons that ionize a gas that is subsequently accelerated by an axial electric field [57].

Despite the difference in underlying physical principles, all SEP technologies can deliver higher specific impulse than chemical propulsion but they all provide very low thrust ( $10 \times 10^{-4}$  N to 3 N).

### 3.1.1 Engine Model

Electric engines work at discrete operation points where the output thrust and resulting mass flow are functions of the input power. Discrete models, however, are not suitable for gradient-based optimizers where the thrust history is unknown a priori [59]. For optimization purposes, polynomial fits for discrete laboratory data are used [32, 48, 56, 60]. Despite ignoring the two-dimensional nature of laboratory models — more than one operating point can exist for the same input power — the polynomial models in Equations (3.1) and (3.2) are continuously differentiable and suitable for gradient-based optimizers.

$$T_E = c_{t0} + c_{t1}P + c_{t2}P^2 + c_{t3}P^3 + c_{t4}P^4 \quad (3.1)$$

$$\dot{m}_E = c_{m0} + c_{m1}P + c_{m2}P^2 + c_{m3}P^3 + c_{m4}P^4, \quad (3.2)$$

where  $T_E$ ,  $\dot{m}_E$  are, respectively, the thrust and mass flow from the engine model and  $P$  is the available power. The engine's specific impulse,  $I_{sp}$ , is computed by Equation (3.3) where  $g_0$  is the standard acceleration due to gravity.

$$I_{sp} = \frac{T_E}{\dot{m}_E g_0}. \quad (3.3)$$

The thrust, mass flow and specific impulse curves for the PPS 1350-G engine model are shown in Figure 3.1. The coefficients for the polynomial model of the PPS 1350-G and other engines considered in this work can be found in the Coefficients for the Engine Models Appendix C.

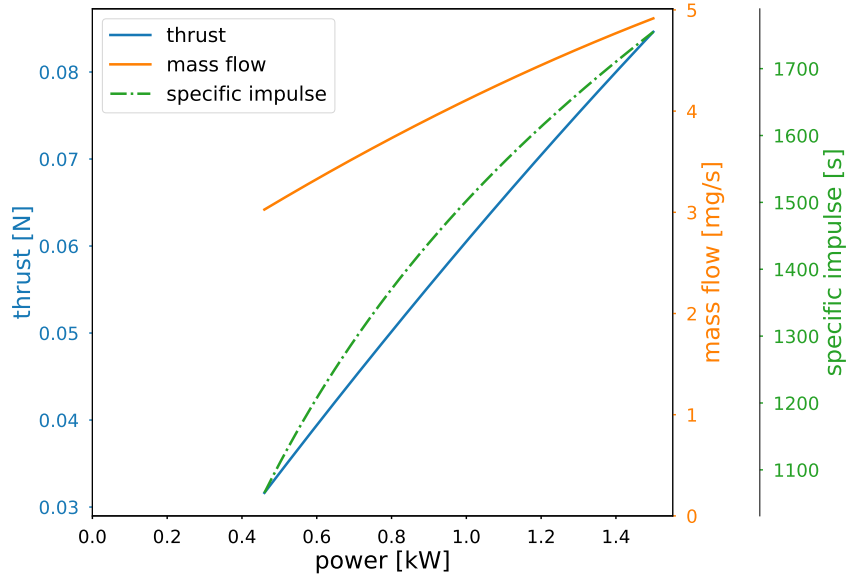


Figure 3.1: Polynomial model of the PPS 1350-G engine [56].

At a given point in the trajectory, the polynomials in Equations (3.1) and (3.2) are evaluated at the available power,  $P_{av}$ . The available power is a function of the available power at 1au,  $P_{1au}$  and the heliocentric distance,  $r$  as in Equation (3.4)

$$P_{av} = \frac{P_{1au}}{r^2}. \quad (3.4)$$

## 3.2 Interplanetary Transfers

The distances in interplanetary trajectories are such that the perturbation of departure and arrival planets or bodies can be neglected in the dynamics. In a first approximation, the departure and arrival points of an interplanetary transfer can be considered as the ephemeris of the departure and arrival bodies at the departure and arrival epochs respectively. This approximation is valid for the majority of the interplanetary missions but is coarse for transfers starting in the Sun-Earth Lagrange points such as The Comet Interceptor Mission (see Chapter 2); such missions have to account for Earth's gravity perturbation in the dynamics. The dynamics for a point mass approximation of a spacecraft under the gravitational influence of the Sun and the Earth, actuated by a SEP system are defined by

$$\ddot{\mathbf{r}} = -\frac{\mu_{\odot}}{\|\mathbf{r}\|^3}\mathbf{r} - \frac{\mu_{\oplus}}{\|\mathbf{r} - \mathbf{r}_{\oplus}\|^3}(\mathbf{r} - \mathbf{r}_{\oplus}) + \frac{\mathbf{T}}{m} \quad (3.5)$$

$$\dot{m} = \frac{\|\mathbf{T}\|}{I_{sp}g_0} \quad (3.6)$$

where  $\mu_{\odot}$  is the Sun Standard Gravitation Parameter,  $\mathbf{r}$  is the spacecraft position vector,  $\mathbf{r}_{\oplus}$  is the Earth position vector,  $\mu_{\oplus}$  is the Earth Standard Gravitation Parameter,  $\mathbf{T}$  is the applied thrust vector and  $m$  is the spacecraft mass. The applied thrust vector  $\mathbf{T}$  is a function of the available thrust,  $T_E$  and the control vector,  $\mathbf{u}$ . The control vector encodes the direction and magnitude of the applied thrust

$$\mathbf{T} = T_E \mathbf{u}. \quad (3.7)$$

The norm of the control should be lower or equal to the unit to ensure that the thrust magnitude upper bound,  $T_E$ , given by Equation (3.1), is respected. The SEP trajectory optimization problem consists in finding the time evolution of the control vector,  $\mathbf{u}(t)$ , that minimizes a cost index, thus it is formulated as an Optimal Control Problem.

## 3.3 Optimal Control Problem

Generally, the Optimal Control Problem can be stated as follows: find the time evolution of the controls,  $\mathbf{u}(t)$ , that minimizes

$$J = \phi(t_f, \mathbf{x}_f) \quad (3.8)$$

subject to

$$\dot{\mathbf{x}} = \mathbf{f}[\mathbf{x}(t), \mathbf{u}(t)], \quad (3.9)$$

$$\mathbf{x}(t_0) = \mathbf{x}_0, \quad (3.10)$$

$$\mathbf{g}[\mathbf{x}(t), \mathbf{u}(t), t] = \mathbf{0}, \quad (3.11)$$

$$\mathbf{h}[\mathbf{x}(t), \mathbf{u}(t), t] \geq \mathbf{0}, \quad (3.12)$$

$$\psi[\mathbf{x}_f, \mathbf{u}_f, t_f] = 0, \quad (3.13)$$

where Equation (3.9) is the dynamic system, Equation (3.10) is the initial value, Equations (3.11) and (3.12) are vector equality and inequality constraints, respectively, and Equation (3.13) are the final boundary conditions;  $t_f$  is free to vary.

Specifically, the interplanetary trajectory optimization problem seeks to maximize the payload by maximizing the final mass,  $m_f$ , consequently minimizing  $-m_f$ . Hence, the cost index Equation (3.8) becomes

$$J = -m_f. \quad (3.14)$$

The final mass is obtained after integrating the set of Ordinary Differential Equations (ODEs) that form the Dynamic System Equation (3.15)

$$\dot{\mathbf{x}} = \begin{Bmatrix} \dot{\mathbf{r}} \\ \ddot{\mathbf{r}} \\ \dot{m} \end{Bmatrix} = \begin{Bmatrix} \dot{\mathbf{r}} \\ -\frac{\mu_{\odot}}{\|\mathbf{r}\|^3} \mathbf{r} + \frac{T_E}{m} \mathbf{u} + \mathbf{\Gamma} \\ -\frac{T}{I_{sp} g_0} \end{Bmatrix}, \quad (3.15)$$

where  $\mathbf{x}$  is the state vector composed by the Cartesian position and velocity vectors and spacecraft mass,  $\mathbf{r}$  is the position vector,  $\ddot{\mathbf{r}}$  is given by Equation (3.5) with  $T_E \mathbf{u}$  substituted into  $\mathbf{T}$ .

The initial conditions for the ODEs are given by the departure Cartesian position,  $[x_0, y_0, z_0]$ , and velocity,  $[v_{x0}, v_{y0}, v_{z0}]$  and spacecraft wet mass,  $m_{wet}$

$$\mathbf{x}(t_0) = [x_0, y_0, z_0, v_{x0}, v_{y0}, v_{z0}, m_{wet}]^T. \quad (3.16)$$

The final boundary conditions are the arrival planet or celestial body position at  $t_f$

$$\psi[\mathbf{x}_f, \mathbf{u}_f, t_f] = \mathbf{x}(t_f) = [x_f, y_f, z_f, v_{xf}, v_{yf}, v_{zf}, m_f]^T. \quad (3.17)$$

The dynamic evolution of the state and the control function must respect equality constraints that vary with the problem being solved. Hence, the equality constraints will depend on the system being modeled and on restrictions imposed by mission designers. An example of a restriction typically required is a coast arc before arrival at destination. Such a restriction is enforced by defining the equality constraint Equation (3.18)

$$\mathbf{u}(t) = \mathbf{0}, \quad t \in [t_f - t^*, t_f], \quad (3.18)$$

where the control vector  $\mathbf{u}$  is constrained to be zero in the time interval  $[t_f - t^*, t_f]$  and  $t^*$  is the duration of the coast arc before the arrival.

Besides equality constraints, the control vector must also respect inequality constraints. Specifically, the norm of the control vector should be lower or equal to 1

$$1 - \|\mathbf{u}(t)\| \geq 0, \quad t \in [t_0, t_f]. \quad (3.19)$$

The general formulation of the Optimal Control Problem in Equations (3.8) to (3.13) is now rewritten as: find the control functions  $\mathbf{u}(t)$  that minimize the cost index Equation (3.8)

$$J = -m_f. \quad (3.14)$$

subject to

$$\dot{\mathbf{x}} = \begin{pmatrix} \dot{\mathbf{r}} \\ \ddot{\mathbf{r}} \\ \dot{m} \end{pmatrix} = \begin{pmatrix} \dot{\mathbf{r}} \\ -\frac{\mu_{\odot}}{\|\mathbf{r}\|^3} \mathbf{r} + \frac{T_E}{m} \mathbf{u} + \mathbf{\Gamma} \\ -\frac{T}{I_{sp} g_0} \end{pmatrix}, \quad (3.15)$$

$$\mathbf{x}(t_0) = [x_0, y_0, z_0, v_{x0}, v_{y0}, v_{z0}, m_{wet}]^T. \quad (3.16)$$

$$\mathbf{u}(t) = \mathbf{0}, t \in [t_f - t^*, t_f], \quad (3.18)$$

$$1 - \|\mathbf{u}\| \geq 0, t \in [t_0, t_f] \quad (3.19)$$

$$\mathbf{x}(t_f) = [x_f, y_f, z_f, v_{xf}, v_{yf}, v_{zf}, m_f]^T .. \quad (3.17)$$

Equations (3.15), (3.18) and (3.19) are continuous functions in time. However, to solve the problem numerically, i.e., to find the control function  $\mathbf{u}(t)$  that minimizes the cost function  $J$ , the problem must be discretized and transcribed into a Nonlinear Programming problem.

### 3.3.1 Transcription to a Nonlinear Programming Problem

The straightforward approach — the direct approach — to solve the Optimal Control Problem in Section 3.3 is to discretize the equations and solve a function minimization problem with a Nonlinear Programming Solver. An alternative approach would be to derive the necessary conditions for optimality and solve the resulting equations (the indirect methods approach) and thus ensure the optimality of the solution. However, as observed in the Review of Trajectory Methods Section 1.2.1, the indirect approach limits the flexibility in handling different problems efficiently because it requires the derivation of analytic conditions for different problems. Accordingly, a direct transcription method will be used here to solve the original Optimal Control Problem as a Nonlinear Programming sub-problem [36].

The Nonlinear Programming problem is a parameter optimization problem concerning a scalar objective function and a vector of constraints [13] where no dynamics is involved. The general Nonlinear Programming problem is stated as [36]: find the  $n$ -vector  $\mathbf{y}^T = (y_1, \dots, y_n)$  to minimize the scalar objective function

$$F(\mathbf{y}) \quad (3.20)$$

subject to the  $m$  constraints

$$\mathbf{c}_L \leq \mathbf{c}(\mathbf{y}) \leq \mathbf{c}_U \quad (3.21)$$

and the simple bounds

$$\mathbf{y}_L \leq \mathbf{y} \leq \mathbf{y}_U, \quad (3.22)$$

equality constraints are imposed by setting  $\mathbf{c}_L = \mathbf{c}_U$ .

The objective is to minimize the symmetric of the final mass. Hence the NLP objective function is

$$F(\mathbf{y}) = -m_f. \quad (3.23)$$

The imposition of the dynamics when solving a NLP problem is made by the transcription method — a direct method in this case. Direct methods handle the dynamics by transcribing the differential equations of the Optimal Control Problem Equation (3.9) into a finite set of equality constraints Equation (3.21): if these equality constraints are respected then the original problem is solved within the degree of accuracy allowed by the discretization scheme [13].

The time domain is uniformly discretized as

$$t_i = t_0 < t_1 < \dots < t_{N-1} = t_f, \quad (3.24)$$

where  $N$  is the number of discretization points. The discretized control and states at  $t_i$  are suitable to be treated as Nonlinear Programming variables.

The discretization of the trajectory is based on the Sims-Flanagan Transcription [29] because the method is fast, robust and has been applied in previous works for preliminary mission design [34]. The trajectory is divided in legs limited by patch points and segments limited by  $N$  control points as in Figure 3.2. To enforce the dynamics, the ODE system Equation (3.15) is replaced by a defect equality constraint Equation (3.25): the discretized states at the patch points,  $\mathbf{x}_p^-, \mathbf{x}_p^+$ , are Nonlinear Programming variables; the ODE system in Equation (3.15) is propagated forward from the departure point to  $\mathbf{x}_p^-$  and backwards from the destination point to  $\mathbf{x}_p^+$  and the residuals,  $\Delta \mathbf{x}_p$ , are driven to zero.

$$\Delta \mathbf{x}_p = \mathbf{x}_p^+ - \mathbf{x}_p^- = 0 \quad (3.25)$$

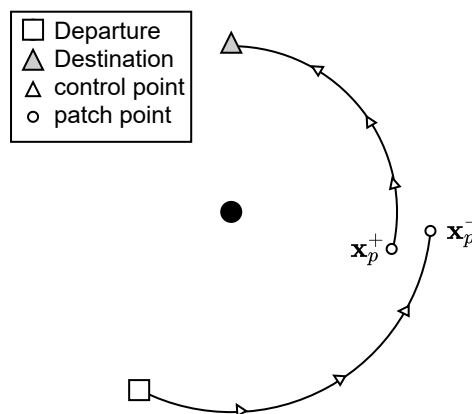


Figure 3.2: Sims-Flanagan transcription [29].

The discrete controls  $\mathbf{u}_i = \mathbf{u}(t_i)$  are considered piece-wise constant over the  $i$ -th trajectory segment and are parameters that go into the  $n$ -vector  $\mathbf{y}$  along with the patch point states  $\mathbf{x}_p^-, \mathbf{x}_p^+$ . Additionally, since the time-of-flight was left free to vary in the original Optimal Control Problem it can be an additional parameter in  $\mathbf{y}$  to be solved for when minimizing the cost index Equation (3.20). Moreover, if the departure infinite velocity,  $v_\infty$  is being optimized it can also be added as a parameter in  $\mathbf{y}$ . Essentially, any mission parameter can be included in the  $n$ -vector  $\mathbf{y}$  as long as all the problem constraints remain linearly independent.

The original problem constraints Equations (3.18) and (3.19) are discretized and enforced at the control points respectively in Equations (3.26) and (3.27)

$$\mathbf{0} \leq \mathbf{u}(t_c) \leq \mathbf{0}, \quad (3.26)$$

$$0 \leq \|\mathbf{u}(t_i)\| \leq 1, \quad (3.27)$$

where  $t_c$  is a time instant in the arrival coast arc.

The general NLP formulation in Equations (3.20) to (3.22) can be now rewritten as: find  $\mathbf{y}$  that minimizes

$$F(\mathbf{y}) = -m_f, \quad (3.23)$$

subject to the constraints

$$\mathbf{x}_p^+ - \mathbf{x}_p^- = \mathbf{0}, \quad (3.25)$$

$$\mathbf{0} \leq \mathbf{u}(t_c) \leq \mathbf{0}, \quad (3.26)$$

$$0 \leq \|\mathbf{u}_i\| \leq 1, \quad (3.27)$$

and the simple bounds

$$-1 \leq \mathbf{u}_{i,x} \leq 1, \quad (3.28)$$

$$-1 \leq \mathbf{u}_{i,y} \leq 1, \quad (3.29)$$

$$-1 \leq \mathbf{u}_{i,z} \leq 1, \quad (3.30)$$

$$\mathbf{x}_L \leq \mathbf{x}_p^-, \mathbf{x}_p^+ \leq \mathbf{x}_U, \quad (3.31)$$

$$\Delta t_{min} < \Delta t < \Delta t_{max}, \quad (3.32)$$

where  $\mathbf{x}_L, \mathbf{x}_U$  constrain the patch point states to remain inside the solar system and with  $\mathbf{y}$  is defined as

$$\mathbf{y} = \{\mathbf{u}_0, \dots, \mathbf{u}_{N-1}, \mathbf{x}_p^-, \mathbf{x}_p^+, \Delta t\}^T, \quad (3.33)$$

and  $\Delta t$  is the time-of-flight.

The NLP solver will use gradient information on the problems functions to find  $\mathbf{y}$  that minimizes  $F(\mathbf{y})$  in Equation (3.23). To do so, an initial guess for  $\mathbf{y}$  must be provided.

## 3.4 Initial Guess Generation

The Ordinary Differential Equation requires an initial guess for the Nonlinear Programming sub-problem variables. The process of generating an initial guess is critical because the quality of the solution is dependent on the guess. Additionally, the initial search for the sub-problem variables may identify interesting regions for the solution: an initial guess search algorithm may find an optimal arrival date or a promising control profile. Accordingly, the initial guess generation process will serve a dual purpose: setup the NLP sub-problem and perform an initial search on the solution space.

### 3.4.1 Grid Search Algorithm

In this work, the design space for a trajectory path is defined by the launch window, the range of admissible time-of-flight and the number of heliocentric revolutions of the trajectory,  $s$ . The launch window — the available dates for the mission launch — define the possible ephemeris of the departure body. The  $\Delta t$  range — the admissible transfer duration interval — defines the arrival body ephemeris for every possible departure date. Evaluating each combination of departure date and time-of-flight is inconceivable because the combinations are infinite. Hence, the design space is discretized. For each combination of departure date,  $t_0$ , and time-of-flight,  $\Delta t$ , there is an additional degree of freedom: the number of heliocentric revolutions,  $s$ , of the trajectory. A grid search evaluates the cost of each  $t_0$ ,  $\Delta t$  and  $s$  combination (see Algorithm 1).

The launch window and time-of-flight range represent mission specific constraints; the number of heliocentric revolutions is related to the time-of-flight. For each  $\Delta t$  a minimum and maximum number of heliocentric revolutions, respectively,  $s_{min}$  and  $s_{max}$ , are computed by

$$s_{min} = \left\lfloor \frac{\Delta t}{\max T_B} \right\rfloor, \quad (3.34)$$

$$s_{max} = \left\lfloor 0.7 \frac{\Delta t}{\min T_B} \right\rfloor + 1, \quad (3.35)$$

where  $T_B = \{\text{Orbital Period of departure body, orbital period of target body}\}$ . Equations (3.34) and (3.35) are based on a heuristic from [49].

The  $t_0$ ,  $\Delta t$ ,  $s$  combinations are used to generate an initial guess for the trajectory path with the Initial Guess Generation Algorithm 2.

The trajectories generated with Algorithm 1 provide a preliminary understanding of the design space. Additionally, these initial guesses can be reused when comparing different spacecraft systems for the same mission because no system constraints are enforced in the trajectories in the Initial Guess Generation Algorithm 2.

### 3.4.2 Describing the Trajectory Path with Chebyshev Polynomials

An efficient analysis of the solution space contrasts with the constraint satisfaction requirements of the Ordinary Differential Equation: enforcing the constraints repeatedly for all the possible solutions

---

**Algorithm 1:** Grid search initial guess generation algorithm [49].

---

$T_B = [\text{Orbital period of departure body, orbital period of target body}]$

```

for  $t_0 \in \text{launch window}$  do
  for  $\Delta t \in [\Delta t_{min}, \Delta t_{max}]$  do
     $s_{min} = \left\lfloor \frac{\Delta t}{\max T_B} \right\rfloor$ 
     $s_{max} = \left\lfloor 0.7 \frac{\Delta t}{\min T_B} \right\rfloor$ 
    for  $s \in [s_{min}, s_{max}]$  do
      Trajectory Generation Algorithm 2
      Store trajectory.
    end
  end
end

```

---

would be cumbersome. Instead, to expedite the initial search, an approximate trajectory model is used. With the approximate trajectory model, the dynamic system equations are respected but the system constraints are not, i.e., the physical laws of celestial motion are enforced, but the limitations on the controls are not. Such an approximate model grants feasible computation times when searching the entire solution space; additionally as it does not enforce system constraints, the initial guesses can be reused when analysing different systems with different constraints. The trajectory path is approximated using Chebyshev polynomials [48].

A generic position coordinate of the spacecraft,  $w$ , is

$$w(t) = \sum_{j=0}^{M-1} b_{w,j} \eta_j(\tau), \quad (3.36)$$

where  $M$  is the number of coefficients and  $M-1$  is the order of the polynomial,  $b_{w,j}$  is the  $j$ -th Chebyshev coefficient and  $\eta_j$  is computed recursively with

$$\eta_j(\tau) = \begin{cases} 1, & \text{if } j = 0 \\ \tau, & \text{if } j = 1 \\ 2\tau\eta_{j-1}(\tau) - \eta_{j-2}(\tau), & \text{if } j \geq 2, \end{cases} \quad (3.37)$$

where  $\tau$  transforms the  $t$  into  $[-1, 1]$ .

The rate of change for the generic position coordinate  $w$  is the time derivative of  $\eta_j(\tau)$

$$\dot{\eta}_j(\tau) = \begin{cases} 0, & \text{if } j = 0 \\ \dot{\tau}, & \text{if } j = 1 \\ 2\dot{\tau}\eta_{j-1}(\tau) + 2\tau\dot{\eta}_{j-1}(\tau) - \dot{\eta}_{j-2}(\tau), & \text{if } j \geq 2. \end{cases} \quad (3.38)$$

The Chebyshev polynomials are the time evolution of  $r$ ,  $\theta$  and  $\varphi$  from the departure to the arrival

ephemerides. The coefficients are computed in three steps: first, the unique set of coefficients that satisfy the boundary conditions are found by Equations (3.43) and (3.44) where it is shown that a unique solution exists for a minimum number of coefficients.

Subsequently, the thrust imposed acceleration,  $\mathbf{a}$ , required to maintain the path described by the Chebyshev coefficients is computed as

$$\mathbf{a} = \ddot{\mathbf{r}} + \frac{\mu_{\odot}}{\|\mathbf{r}\|^3} \mathbf{r}, \quad (3.39)$$

where  $\mathbf{r}$  is the position vector given by the Chebyshev polynomials. The first term of the right hand side of Equation (3.39) is the acceleration felt by a body on the trajectory described by the Chebyshev coefficients; the second term is the acceleration due to the Sun gravity. Hence,  $\mathbf{a}$  in Equation (3.39) is the thrust imposed acceleration required to follow the path described by the Chebyshev polynomials for a spacecraft subject to the gravitational pull of the Sun.

However, the acceleration required to maintain the path described by the minimum number of coefficients may not be admissible for a spacecraft system. Hence, the final step in the initial guess generation process is minimizing  $\mathbf{a}$ : additional coefficients are used, increasing the order of the polynomials and allow for further degree's of freedom that can be optimized to minimize  $\mathbf{a}$ . Algorithm 2 describes the algorithm that incrementally increases the polynomial order and minimizes  $\mathbf{a}$ .

### Trajectory Path: Satisfying Boundary Conditions

The boundary conditions of an interplanetary transfer vary according to the type of trajectory: the position and velocity of the spacecraft must match the target's position and velocity at  $t_f$  for rendezvous trajectories; for flyby trajectories, only the spacecraft position at  $t_f$  is required to match that of the target.

For a rendezvous trajectory, the polynomial description of the trajectory shall verify Equations (3.40) and (3.41) to satisfy the boundary conditions

$$\left[ r(t_0), \dot{r}(t_0), \theta(t_0), \dot{\theta}(t_0), \varphi(t_0), \dot{\varphi}(t_0) \right]^T = \left[ r_0, \dot{r}_0, \theta_0, \dot{\theta}_0, \varphi_0, \dot{\varphi}_0 \right]^T \quad (3.40)$$

$$\left[ r(t_f), \dot{r}(t_f), \theta(t_f), \dot{\theta}(t_f), \varphi(t_f), \dot{\varphi}(t_f) \right]^T = \left[ r_f, \dot{r}_f, \theta_f + s2\pi, \dot{\theta}_f, \varphi_f, \dot{\varphi}_f \right]^T, \quad (3.41)$$

where  $\left[ r_0, \dot{r}_0, \theta_0, \dot{\theta}_0, \varphi_0, \dot{\varphi}_0 \right]^T$  and  $\left[ r_f, \dot{r}_f, \theta_f + s2\pi, \dot{\theta}_f, \varphi_f, \dot{\varphi}_f \right]^T$  are, respectively, the departure and arrival boundary conditions in spherical coordinates. For flyby trajectories  $\dot{r}(t_f)$ ,  $\dot{\theta}(t_f)$  and  $\dot{\varphi}(t_f)$  are free.

If  $\mathbf{B}$  is defined as the vector with the Chebyshev basis functions  $\eta_j(\tau)$  and its time derivative  $\dot{\eta}_j(\tau)$

$$\mathbf{B}(\tau) = \begin{bmatrix} \eta_0(\tau) \dots \eta_{M-1}(\tau) \\ \dot{\eta}_0(\tau) \dots \dot{\eta}_{M-1}(\tau) \end{bmatrix}, \quad (3.42)$$

the satisfaction of the boundary conditions in Equations (3.40) and (3.41) is the solution of the linear equations Equations (3.43) and (3.44), respectively for the initial and final boundary conditions.

$$\begin{bmatrix} \mathbf{B}(-1) & \mathbf{0} & \mathbf{0} \\ \mathbf{0} & \mathbf{B}(-1) & \mathbf{0} \\ \mathbf{0} & \mathbf{0} & \mathbf{B}(-1) \end{bmatrix} \begin{bmatrix} b_{r,0} \\ \vdots \\ b_{r,M-1} \\ b_{\theta,0} \\ \vdots \\ b_{\theta,M-1} \\ b_{\varphi,0} \\ \vdots \\ b_{\varphi,M-1} \end{bmatrix} = \begin{bmatrix} r_0 \\ \dot{r}_0 \\ \theta_0 \\ \dot{\theta}_0 \\ \varphi_0 \\ \dot{\varphi}_0 \end{bmatrix} \quad (3.43)$$

$$\begin{bmatrix} \mathbf{B}(1) & \mathbf{0} & \mathbf{0} \\ \mathbf{0} & \mathbf{B}(1) & \mathbf{0} \\ \mathbf{0} & \mathbf{0} & \mathbf{B}(1) \end{bmatrix} \begin{bmatrix} b_{r,0} \\ \vdots \\ b_{r,M-1} \\ b_{\theta,0} \\ \vdots \\ b_{\theta,M-1} \\ b_{\varphi,0} \\ \vdots \\ b_{\varphi,M-1} \end{bmatrix} = \begin{bmatrix} r_f \\ \dot{r}_f \\ \theta_f \\ \dot{\theta}_f \\ \varphi_f \\ \dot{\varphi}_f \end{bmatrix}. \quad (3.44)$$

From Equations (3.43) and (3.44) two conclusions are drawn: each coordinate requires 4 Chebyshev coefficients to satisfy rendezvous conditions (initial position and velocity plus final position and velocity) and three coefficients for flyby trajectories (initial position and velocity plus final position); there is a unique solution for the coefficients that satisfies the boundary conditions if the number of coefficients,  $M$ , is equal to 4 for rendezvous trajectories or 3 for flyby trajectories.

The presence of a unique solution for the coefficients eliminates the need for an initial guess for the coefficients. Further, the linear relations are simple and thus can be efficiently evaluated. After satisfying the boundary conditions, additional coefficients can be added to the series to minimize  $a$ .

### Optimizing the coefficients

The optimization of the coefficients seeks to increase the likelihood of the initial guess being transformed into a feasible spacecraft trajectory, by minimizing the acceleration required to maintain the trajectory. The coefficients optimization problem may be seen as a parameter optimization problem suitable to be solved by a NLP solver.

The Nonlinear Programming problem for the Chebyshev coefficients can now be defined as: find the  $3M$ -vector  $\mathbf{y}$  that minimizes

$$J = \int_{t_0}^{t_f} \|\mathbf{a}\|^2 dt, \quad (3.45)$$

subject to

$$\mathbf{B}(\tau = -1)\mathbf{y} = [r_0, \dot{r}_0, \theta_0, \dot{\theta}_0, \varphi_0, \dot{\varphi}_0]^T \quad (3.40)$$

$$\mathbf{B}(\tau = 1)\mathbf{y} = [r_f, \dot{r}_f, \theta_f, \dot{\theta}_f, \varphi_f, \dot{\varphi}_f]^T, \quad (3.41)$$

where  $\mathbf{y}$  is defined as

$$\mathbf{y} = \{b_{r,0}, \dots, b_{r,M-1}, b_{\theta,0}, \dots, b_{\theta,M-1}, b_{\varphi,0}, \dots, b_{\varphi,M-1}\}^T. \quad (3.46)$$

Equation (3.45) is used as it is smooth and quadratic and it is numerically simple to solve [49].

When the number of coefficients is equal to four, there is only one solution that satisfies the rendezvous boundary conditions; oppositely, when the number of coefficients is higher than four, there are infinite solutions for the coefficients. The four coefficients unique solution can be used as an initial guess for a path described by five coefficients: the linear equations Equations (3.43) and (3.44) are solved with four coefficients; a fifth coefficient with initial value equal to zero is added; an optimization process takes place to find the five coefficients solution that minimizes a performance index. The process is repeated until a satisfactory solution is achieved: the five coefficients optimized solution serves as the initial guess for the six coefficients path and so on. This incremental search, summarized in Algorithm 2, eliminates the need for a user supplied guess for the coefficients solution.

---

**Algorithm 2:** Chebyshev coefficients optimization algorithm [49].

---

Get boundary conditions

Solve linear relations Equations (3.43) and (3.44) for  $M_{min} = 4$  (rendezvous) or  $M_{min} = 3$  (flyby)

$M = M_{min}$

**while**  $M < M_{max}$  **do**

    set the first  $M$  coefficients equal to the previous solution

    add  $(M + 1)^{th}$  coefficient to each coordinate and set it to zero

    compute thrust imposed acceleration,  $a$ , required to maintain the trajectory

    optimize  $(M + 1)$  coefficients that minimize  $J$  subject to Equations (3.40) and (3.41)

$M = M + 1$

**end**

---

Typically, for  $M > 10$  the solution does not improve [48]. Hence, the NLP problem in the coefficients only has  $3M = 30$  variables. Because the problem is small, an algorithm that efficiently searches for solutions in the launch window and time-of-flight ranges supplied by the user can be employed for a preliminary search of the solution space.

### 3.4.3 Initial Guess Selection Policy

From the initial guesses generated with Algorithms 1 and 2, more than one initial guess is subject to further optimization because the best trajectory from the grid search may not be close to the optimal trajectory to be performed by a spacecraft, i.e., the optimal solution of the OCP in Section 3.3 may

not be obtained with the best solution from the grid search. The set of initial guesses that are further optimized is obtained from the resulting set of Algorithm 1 after applying a selection policy. Two selection policies are considered in this work with the goal of diversifying the pool of trajectories to be considered in the OCP: selection by number of revolutions and selection by time-of-flight.

The selection by number of revolutions policy divides the initial guesses set into subsets of trajectories with the same number of heliocentric revolutions. From each of the subsets, the lowest  $\Delta v$  trajectory is selected and fed to the NLP solver. The selection by time-of-flight policy divides the initial set of trajectories into  $j$  subsets. The  $i$ -th subset contains trajectories with a time-of-flight

$$\Delta t \in \left[ \Delta t_{min} + \Delta t_{range} \frac{i}{n}, \Delta t_{min} + \Delta t_{range} \frac{i+1}{n} \right], \text{ with } i \in [0, j-1]. \quad (3.47)$$

From each subset, the lowest  $\Delta v$  trajectory is selected and fed to the NLP solver.

### 3.4.4 Computing the Initial Guess Control Profile

The final step in the generation of the initial guess for  $y$  in Section 3.3.1 is to compute the control variables  $\mathbf{u}_i$ . This step is specific to the spacecraft system being analysed, namely it requires the initial spacecraft mass and specific impulse of the propulsion system.

---

**Algorithm 3:** Algorithm to convert the acceleration profile of the initial guess into a thrust profile based on the spacecraft system [49].

---

Get propulsion system  $I_{sp}$

Get  $m_0 = m_{wet}$

**for**  $t \in t_i$  **do**

$$\left| \begin{array}{l} \Delta v_i = \int_{t_i}^{t_{i+1}} \|\mathbf{a}\| dt \\ m_{i+1} = m_i \exp\left(-\frac{\Delta v_i}{I_{sp} g_0}\right) \\ \mathbf{u}_i = \frac{1}{T_E} \frac{\mathbf{a}(t_i)}{\|\mathbf{a}(t_i)\|} \frac{m_i - m_{i+1}}{t_{i+1} - t_i} I_{sp} g_0 \end{array} \right.$$

**end**

---



# Chapter 4

## Implementation

One of the goals of this work is to implement the algorithms to generate feasible Solar Electric Propulsion trajectories given the departure and arrival bodies, the launch window and a desired time-of-flight range. The software should be able to perform trade studies, specifically, compare the performance of different engines and different available power conditions. The software is called LowWiz. LowWiz is developed in Python because it is open source and a mature programming language. Besides the built-in python functions, the software extensively uses the standard python libraries NumPy [61] for numerical operations, numba [62] for just in time compilation of computationally intensive functions and matplotlib [63] for plotting.

### 4.1 External software

The majority of the software was developed by the author of this work, namely, the architecture design and the implementation of the algorithms from Chapter 3. The ephemeris system, the NLP solver and the trajectory propagator are implemented using external software.

ESA's PyKEP [64] library is used for trajectory propagation.

#### Ephemerides

The ephemeris for departure and arrival bodies are obtained using SpiceyPy [65], a Python wrapper for JPL's Navigation and Ancillary Information Facility (NAIF) named SPICE [66, 67].

The ephemeris information is stored in kernels. The baseline box version of LowWiz is provided with the kernels for solar system ephemerides; for smaller bodies, Near-Earth Asteroid (NEA), comets and even spacecrafts, the appropriate kernel has to be fetched from the NAIF database and loaded to LowWiz.

#### Nonlinear Programming Solver

The Ordinary Differential Equation and the Chebyshev coefficient optimization problem are transcribed to Nonlinear Programming Parameter Optimization problems solved with the Python Parallel Global

Multiobjective Framework for Optimization (PyGMO), the python wrapper for ESA's Parallel Global Multiobjective Framework for Optimization (PaGMO) [68]. From the algorithms in pygmo, the Sequential Least-Squares Quadratic Programming (SLSQP) [69] is used. The stochastic optimization algorithms available with PyGMO were considered but not used as the problem's nature was not combinatorial and a gradient was available which made convergence faster [12].

PyGMO requires that the problems are translated into a class that implements the software's problem interface. Specifically, objects of the class problem should possess a fitness method that returns the fitness vector

$$\mathbf{f} = \left\{ \begin{array}{c} J \\ \mathbf{c} \end{array} \right\}, \quad (4.1)$$

where  $J$  is the objective function being minimized and  $\mathbf{c}$  is the constraints vector both evaluated for a given value of the  $n$ -vector of problem variables. Additionally, as the SLSQP algorithm is a gradient-based solver, it accepts gradient information. The gradients were computed using PyGMO's builtin finite differences capabilities for numerical differentiation.

## 4.2 Architecture

The software has two entry points: a command line interface and a toolbox. The command line interface encapsulates the complexity of the software, described in Section 4.2.1, and only requires the user to define configuration files. The command line interface runs the set of operations that form the basic capabilities of the software — optimize trajectories and perform trade studies. Oppositely, the toolbox directly exposes the different modules of LowWiz in Figure 4.1 to the user. The toolbox requires the user to understand at least the high level functionalities of the software modules. Nonetheless, the added flexibility of the toolbox can be exploited to develop new applications or to analyse missions with unusual characteristics, such as the Comet Interceptor mission which does not have a known target until the launch.

### 4.2.1 Command Line Interface

The software should have a command line interface to encapsulate the complexity of the algorithms and release the work load of mission analysis engineers.

The command line interface is configured through two input files: one for the software's settings and one for the mission scenario. The settings available for the user to configure are: maximum number of Chebyshev coefficients for the initial guess ( $M_{max}$  in Section 3.4); initial guess selection policy; number of discretization points; maximum number of iterations for the optimizers; post-processing flags to select which plots to store. Regarding the scenario configuration file, the user is required to define the following: departure and target bodies; trajectory type (rendezvous or flyby); flyby relative velocity range (for flyby trajectories); departure escape velocity; duration of arrival coast arc; launch window; minimum and maximum time-of-flight ( $\Delta t_{range} = [\Delta t_{min}, \Delta t_{max}]$ ); spacecraft dry mass; spacecraft input power at 1 au

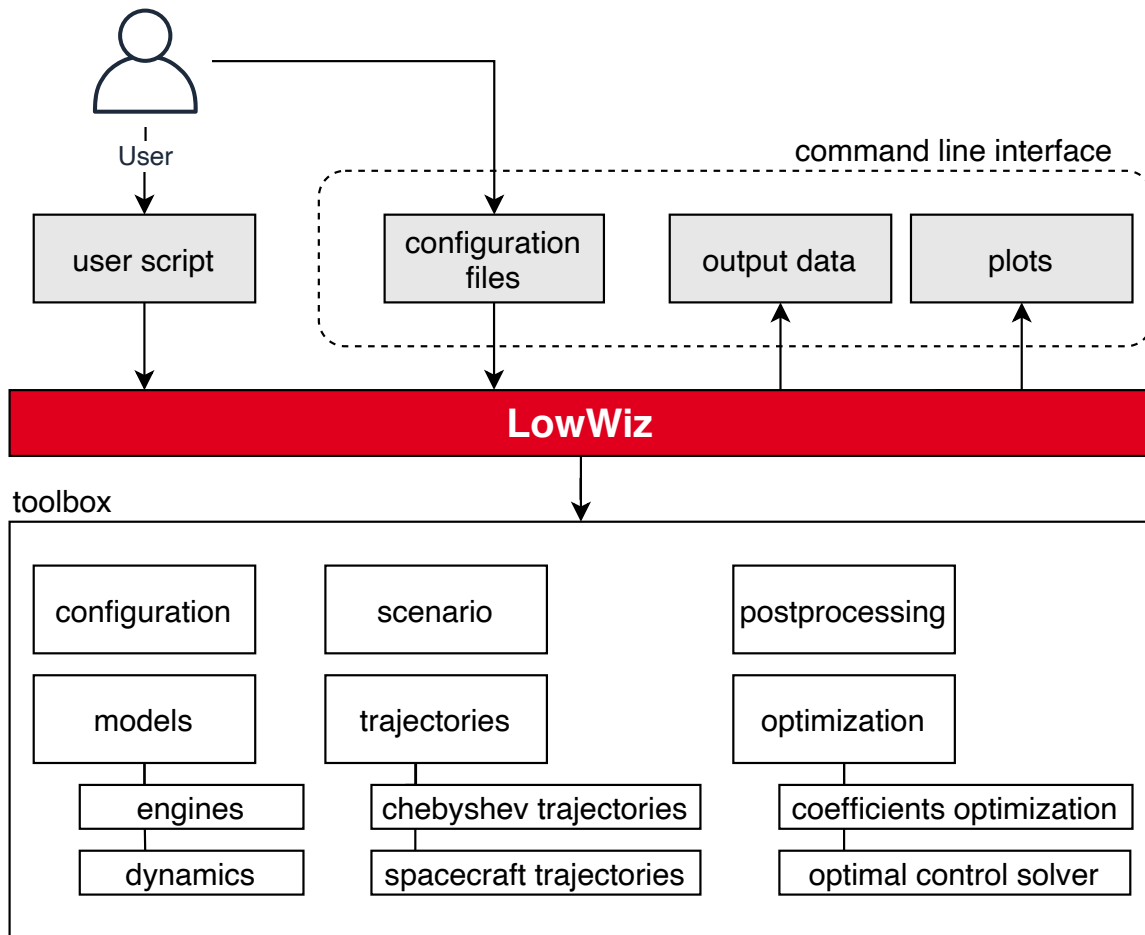


Figure 4.1: LowWiz architecture.

and electric propulsion engine. Additionally, for trade studies, the user shall define the available engines and the range to vary the input power at 1 au.

After parsing the input files, LowWiz follows the logic outlined in Figure 4.2: initial guesses from previous runs are loaded if they were stored, or computed if no previous results are available; a set of trajectories is filtered from the pool of initial guesses according to a selection policy from Section 3.4.3 specified by the user; the initial guesses are transformed into feasible trajectories; the data are post-processed to generate the outputs.

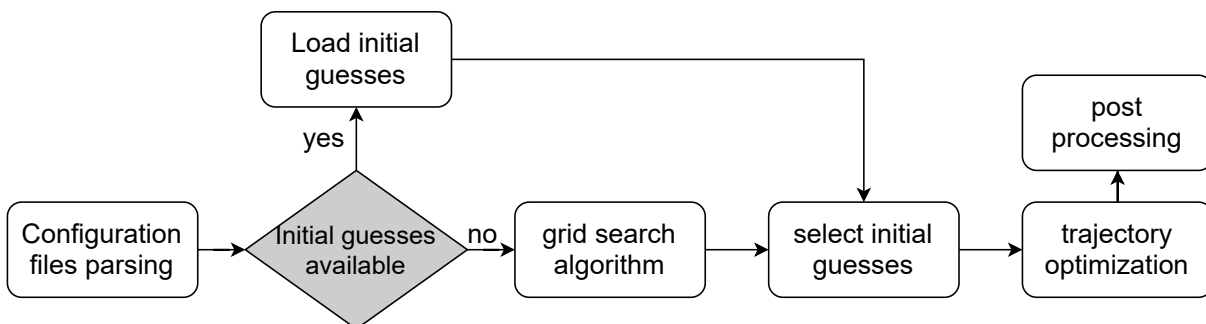


Figure 4.2: LowWiz Command Line Interface Logic

## 4.2.2 Software Modes

LowWiz can be executed in three modes: Trajectory Optimization, Engine Trade Studies, Input Power Trade Studies. The Trajectory Optimization mode generates feasible spacecraft trajectories given the defined mission constraints; the Engine Trade Studies mode compares the performance of different EP engines in the defined mission scenario; the Input Power Trade Studies mode analyzes the impact on performance of increasing or decreasing the input power to the engine.

### Trajectory Optimization

The trajectory optimization mode solves an optimal control problem for each of the pre-selected initial guesses. Feasible spacecraft trajectories are displayed by way of plots of the trajectory in two and three dimensions (see Figures A.1 and A.2), thrust profile plots (see Figure A.3) and required power plots (see Figure A.4). The trajectory and control profile may also be stored as python objects or written into tables in binary files. The initial set of trajectories obtained with the Grid Search Algorithm 1 is also used to plot a  $\Delta v$  contour (Pork Chop Diagram) for the launch window, such as Figure 4.3, mapping each departure date and time-of-flight combinations to an estimate of the  $\Delta v$  required to reach the target.

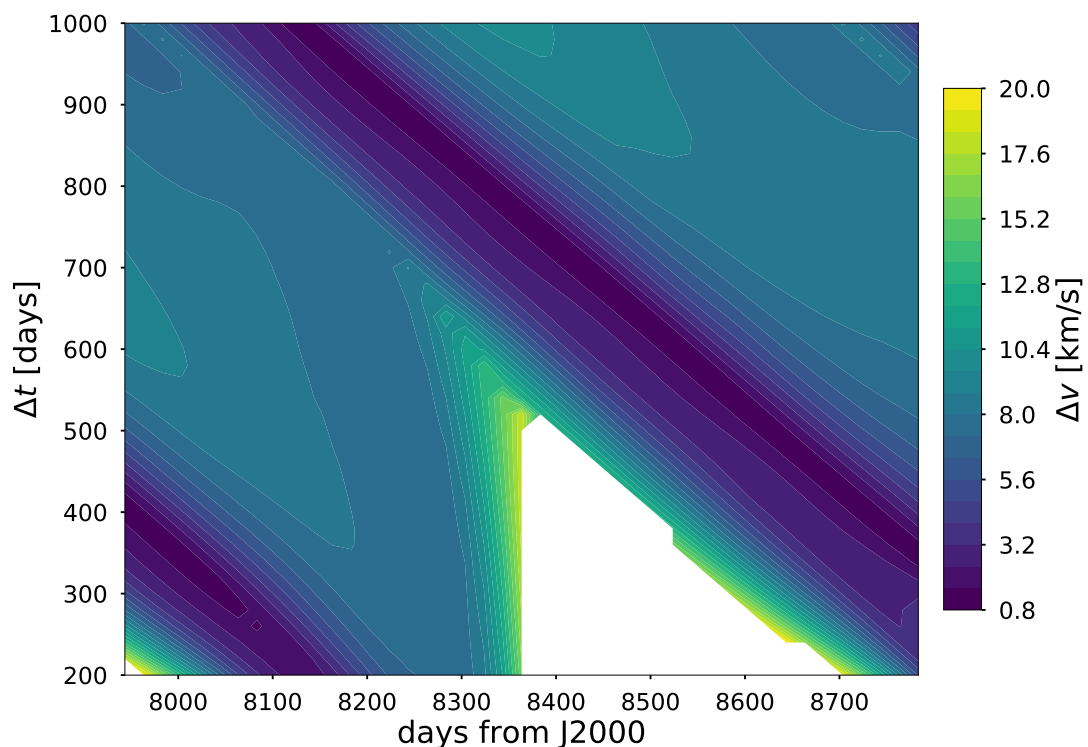


Figure 4.3: Earth to Didymos transfer  $\Delta v$  contour (Pork-Chop Diagram). A transfer to Didymos presents low  $\Delta v$  ( $\Delta v < 1 \text{ km s}^{-1}$ ) opportunities over the entire launch window if the time-of-flight,  $\Delta t$ , is allowed to vary between 200 d and 1000 d.

### Engine Trade Studies

The engine trade studies mode selects the initial guess using the time-of-flight selection policy. The software runs the Trajectory Optimization mode with the same initial guesses, varying the engine model

being used. This strategy results in curves where the propellant mass is a function of time-of-flight for each of the engines, shown in Figure 4.4.

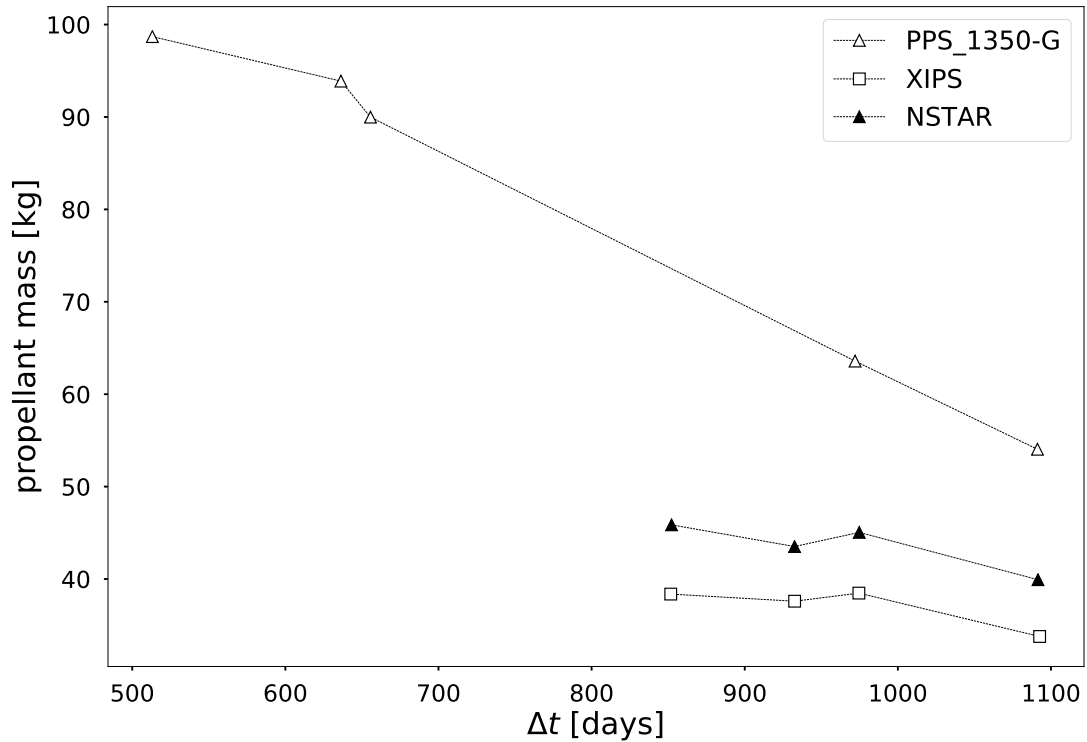


Figure 4.4: Engine Trade Studies mode output example.

Typically the engine that is able to operate at the highest specific impulse, given the power constraints of the trajectory, will correspond to the best solution in Figure 4.4, i.e., the engine that is able to operate at a highest efficiency regime will correspond to lower values in terms of propellant mass.

### Input Power Trade Studies

The available input power for the engine is a function of solar panel area,  $A_{panel}$ , solar panel efficiency  $\eta(t)$ , the Sun incidence angle,  $\Theta$ , and spacecraft position,  $\mathbf{r}(t)$ , given by

$$P_{av} = G_{SC} \frac{A_{panels}}{\|\mathbf{r}(t)\|^2} \eta(t) \cos \Theta, \quad (4.2)$$

where  $G_{SC}$  is the solar constant, the solar energy flux per unit of area measured at 1 au.

In a first approximation, some terms in Equation (4.2) might be neglected: the solar panel area is constant for a given trajectory and solar panel efficiency can be considered constant too. Additionally, the cosine loss,  $\cos \Theta$ , can be neglected as it can be assumed that the attitude constraints allow for proper spacecraft orientation. Consequently, for a single trajectory, the numerator terms in Equation (4.2) are grouped into a constant value, equivalent to the available power at 1 au,  $P_{1au}$ , yielding

$$P_{av} \propto \frac{P_{1au}}{\|\mathbf{r}(t)\|^2}. \quad (4.3)$$

The available power in Equation (4.3) is a function of the spacecraft position and thus time. Comparing transfers based on the available power throughout the trajectory is not representative, given the coupled nature of system and trajectory described in the Solar Electric Propulsion Section 1.1. Instead, the available input power at 1 au,  $P_{1au}$ , is the reference to compare the trajectories in the trade studies.

For the input power trade studies mode, the user supplies the range of available input power at 1 au and the initial guess selection policy. After selecting the trajectories, LowWiz runs the trajectory optimization mode for 10 linearly spaced values in the available power range. If the trajectories are selected according to time-of-flight, the result is displayed as propellant mass curves which are functions of input power for each time-of-flight value of the initial guess; if the selection policy is in accordance to the number of revolutions, the different curves in Figure 4.5 refer to the number of revolutions of the originating initial guess.

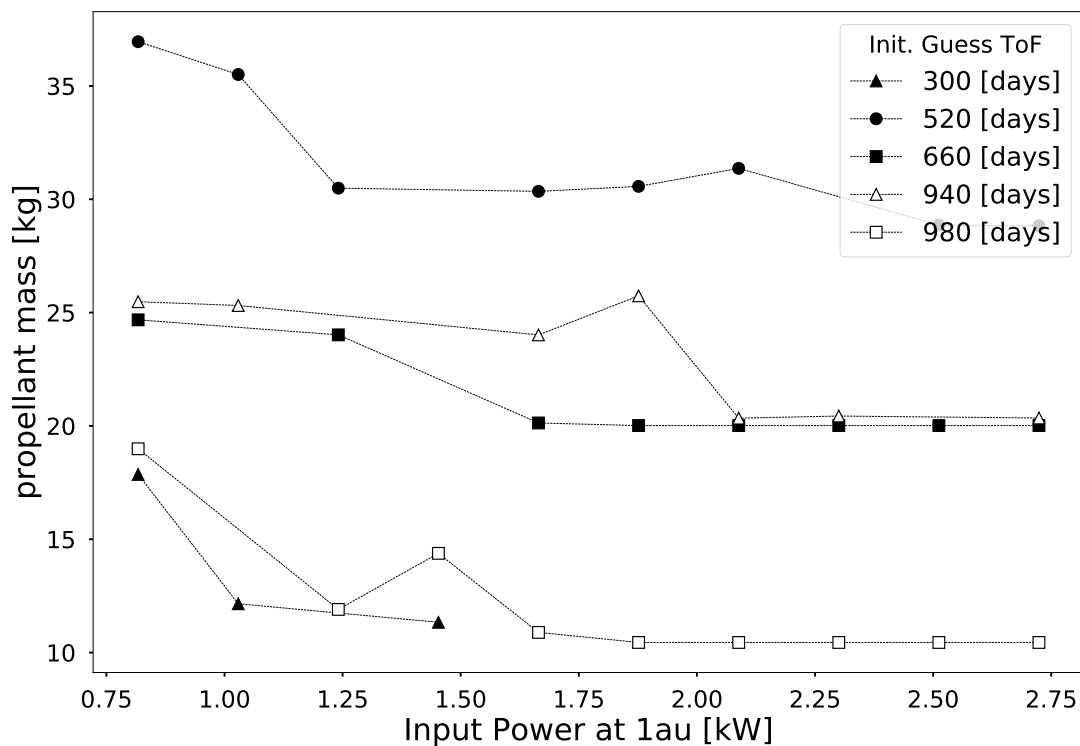


Figure 4.5: Input Power Trade Studies mode output example.

Typically, from a certain value of available input power, the trajectories do not improve, as the engine will already have all of its operating power range below the available power for the entire trajectory.

### 4.3 Software Validation

LowWiz was tested against scenarios found in the literature to validate the software: a comet rendezvous mission (Section 4.3.1), and a Near-Earth Asteroid Flyby (Section 4.3.2). For each scenario, the solutions obtained with LowWiz are compared with solutions available in the literature. The comparison is quantitative in terms of time-of-flight and propellant mass and qualitative in the analysis of the shape of the trajectory and of control profile solutions.

### 4.3.1 Comet Rendezvous Mission

A Comet Rendezvous scenario available from [60] was simulated in LowWiz to evaluate the program's behaviour when dealing with a target in an eccentric orbit: the comet Kopff's orbit has an eccentricity of  $e = 0.54$ . Accordingly, the data extracted from [60] for a LowWiz scenario file is summarized in Table 4.1.

Table 4.1: Kopff rendezvous scenario configuration.

Parameter	Value
Engine	NEXT
Spacecraft launch mass (kg)	1030
Input power at 1 au (kW)	9
time-of-flight range (d)	1100 to 1900
Maximum departure $v_\infty$ (km s <sup>-1</sup> )	4
Launch window	[2006-JAN-01, 2007-JAN-01]

The optimal solution found by LowWiz, shown in Figure 4.6, is comparable to the best result in [60] (see Table 4.2).

Table 4.2: Kopff scenario validation results.

Parameter	LowWiz	Literature Result
arrival mass (kg)	732	784
time-of-flight (d)	1350	1387
departure $v_\infty$ (km s <sup>-1</sup> )	4.0	3.7

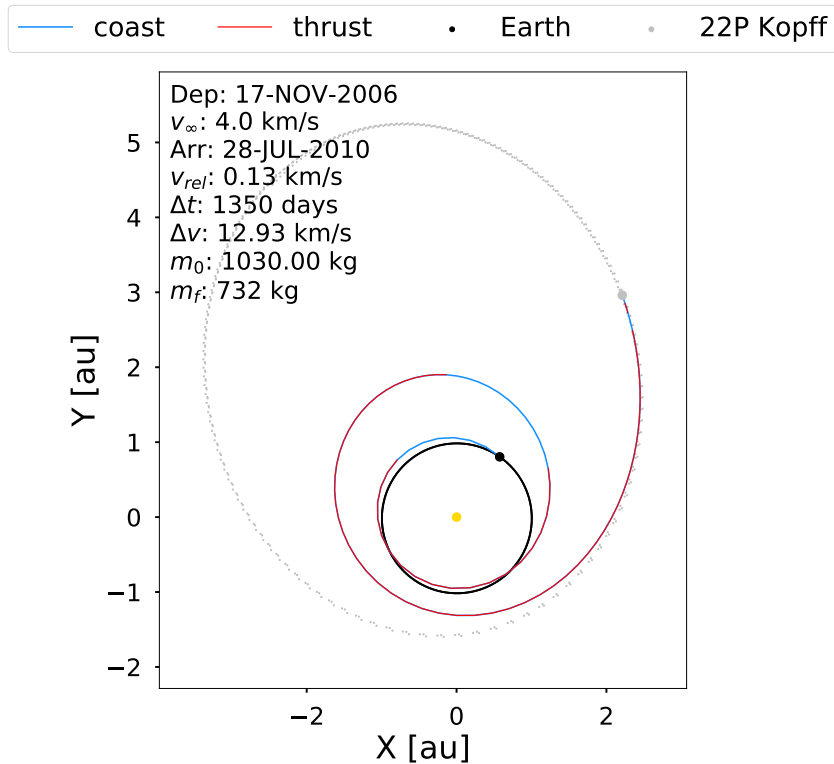


Figure 4.6: Interplanetary transfer to the comet Kopff in the Heliocentric Earth Ecliptic reference frame.

The LowWiz solution, shown in Figure 4.6, delivers less mass to the destination (6.5 % less compared

to [60]). The LowWiz trajectory leaves Earth with a higher escape velocity ( $4.0 \text{ km s}^{-1}$  against  $3.7 \text{ km s}^{-1}$  from [60]); the destination is reached in less than 37 d compared to the literature solution (3% reduction in  $\Delta t$  compared to [60]).

Additionally, the control profile for the LowWiz solution, shown in Figure 4.7, is bang-bang. The bang-bang feature is also noticed in the solutions in [60] and indicates at least local optimality for the solution.

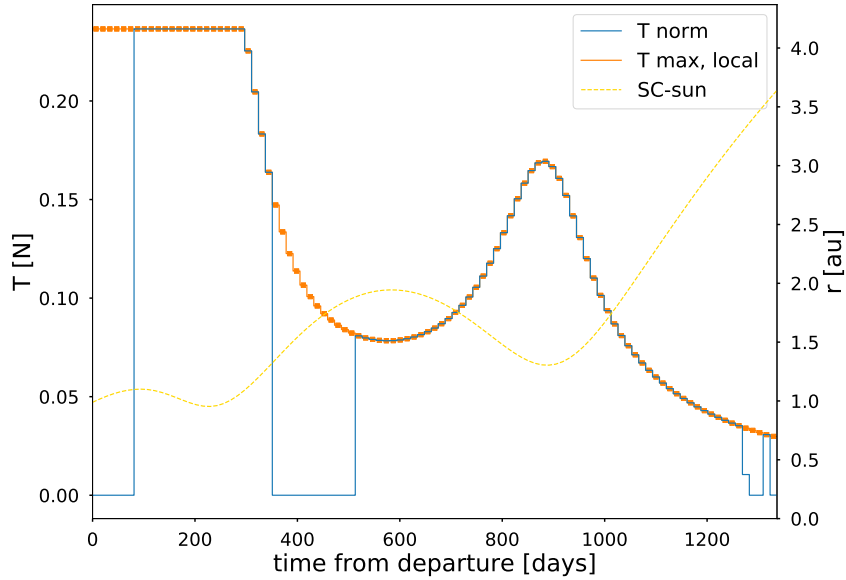


Figure 4.7: Thrust magnitude profile for an interplanetary transfer to the comet Kopff. The available maximum thrust varies with the spacecraft to Sun distance.

### 4.3.2 Near-Earth Asteroid Flyby Mission

The DART mission was chosen to test the optimization of flyby trajectories. The mission is not exactly a flyby mission — it aims at impacting the smaller asteroid in the binary system Didymos — but the spacecraft is expected to encounter the system with a net relative velocity. The scenario was simulated extracting data from [70], summarized in Table 4.3.

Table 4.3: Didymos flyby scenario configuration.

Parameter	Value
Engine	PPS 1350G
Spacecraft wet mass (kg)	354
Input power at 1 au (kW)	10
Flyby velocity range ( $\text{km s}^{-1}$ )	5 to 6
time-of-flight range (d)	400 to 750
Maximum departure $v_\infty$ ( $\text{km s}^{-1}$ )	0
Launch window	[2020-JUL-01, 2020-DEC-01]

The optimal solution found by LowWiz, shown in Figure 4.8, is compared to the literature solution in Table 4.4. The trajectory from [70] is concerned with maximizing the relative momentum for the asteroid impact (thus the solution in [70] arrives with a higher relative velocity at the asteroid) and also takes into

account an intermediate interception of another asteroid; this intermediate encounter and the higher arrival relative velocity in the literature solution should be considered when comparing the difference in the arrival mass.

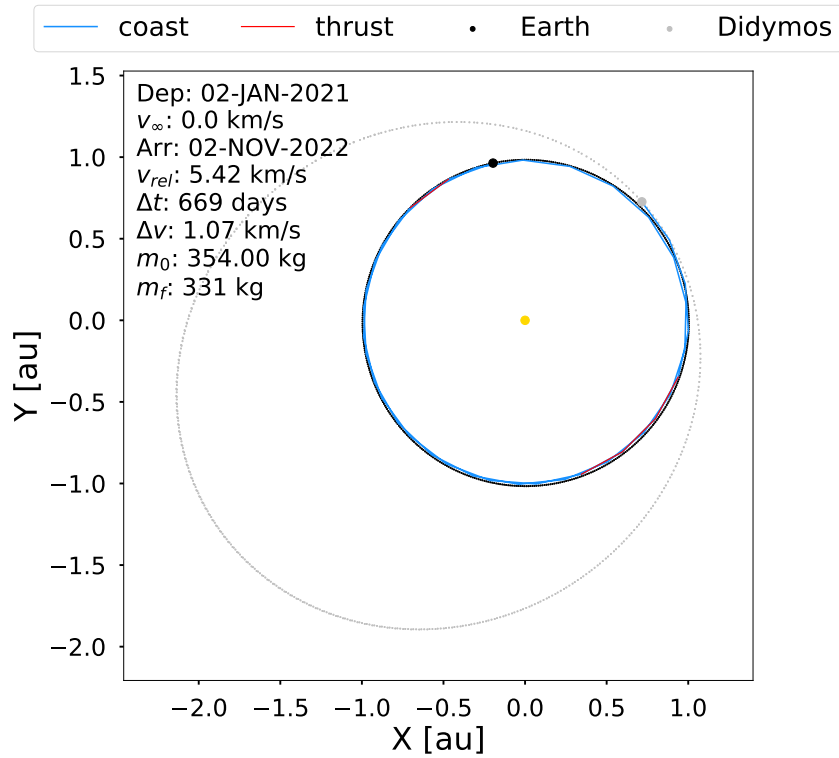


Figure 4.8: Interplanetary transfer to Didymos in the Heliocentric Earth Ecliptic reference frame.

Table 4.4: Didymos scenario validation results.

Parameter	LowWiz	Literature Result
arrival mass (kg)	331	316
time-of-flight (d)	669	636
arrival $v_{rel}$ ( $\text{km s}^{-1}$ )	5.42	6.02

Adding to the high level validation tests performed in Sections 4.3.1 and 4.3.2, the unitary tests performed at the software elements' level grant a fair degree of confidence to exploit the software in the preliminary mission analysis of The Comet Interceptor.



## Chapter 5

# Application to The Comet Interceptor Mission Transfer

The Comet Interceptor transfer optimization is separated into two problems: transfer to main target and transfer to backup targets. As the main target is not yet defined, the respective analysis is concerned with evaluating the cost of reaching possible encounter locations (Section 5.1); preliminary backup targets are already identified — a transfer to 73P/Schwassmann-Wachmann is analysed (Section 5.2).

The assumptions followed for the trajectory optimization results — described in the Transfer Geometry, Transfer Dynamics and Spacecraft and Propulsion System in Sections 2.3.1 to 2.3.3 — are summarized in Table 5.1.

Table 5.1: Trajectory Optimization Assumptions for the Comet Interceptor EP analysis.

Encounter	Unknown target	Arrival at a circular orbit with final position defined by $R_c - \vartheta$
	Backup target	Match comet position ephemeris, free arrival velocity
	Navigation constraint	60 days coast arc prior to encounter
Dynamics	Two-Body Problem	Sun as central body, ephemeris for Earth and SEL2
	Direct Transfer	Departure from SEL2 ephemeris (position and velocity)
	Moon Gravity Assist	Departure from Earth ephemeris with $v_\infty < 1.4 \text{ km s}^{-1}$ opposite to Earth's velocity
Spacecraft	Engine	PPS1350 engine model from SMART-1, 100% duty cycle
	Power at 1 au (W)	800, $P \propto 1/r^2$
	Mass (kg)	750 wet mass

The spacecraft EP reference design point in the Spacecraft and Propulsion System Assumptions Section 2.3.3 is used for all the results here discussed. The trajectory optimization problem is solved with LowWiz (see Implementation Chapter 4). Unless indicated otherwise, each trajectory is divided into 40 segments and the optimizer is allowed to go up to 1000 iterations.

## 5.1 Probing Encounter Locations

As explained in the Target Comets Section 2.1, the mission is being designed without a specific target hence without a specific encounter location. To understand the reachability of encounter locations, the CReMA performs a parametric study relating the impulsive  $\Delta v$  (CP) and time-of-flight to reach a set of positions defined by  $R_c$  and  $\vartheta$ . The encounter locations probe here presented expands the CReMA analysis to continuous propulsion.

The encounter locations are considered for  $R_c \in [0.9, 1.2]$  au with 0.1 au steps and  $\vartheta \in [-150^\circ, 150^\circ]$  with  $15^\circ$  steps yielding a total of 80 points. Encounter locations outside the  $R_c$  range are too costly in terms of  $\Delta v$ ;  $\vartheta$ 's near or close to  $0^\circ$  or  $180^\circ$  are not considered to avoid comet encounters during a solar conjunction.

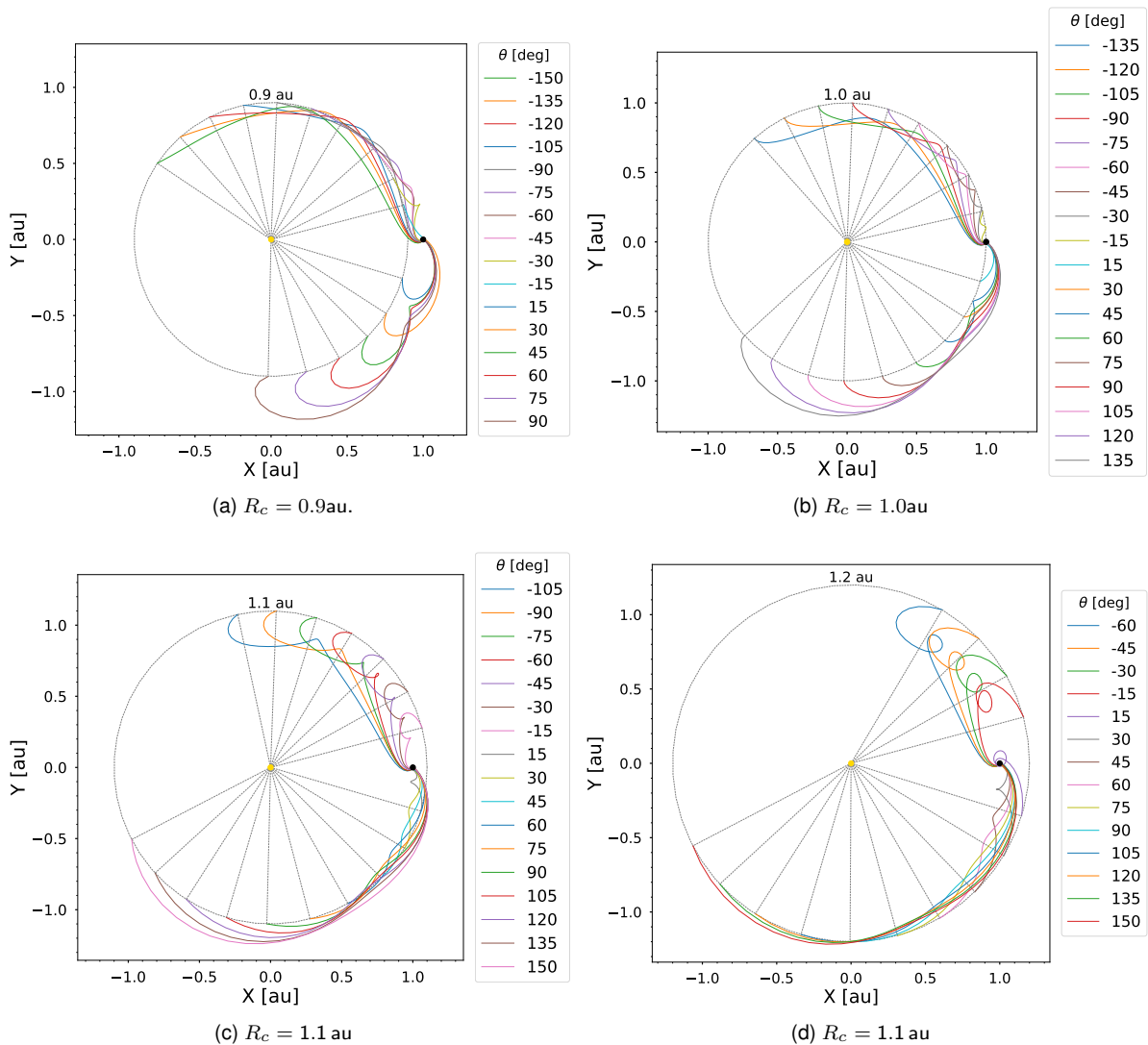


Figure 5.1: Results for a LowWiz run searching for 1-revolution trajectories with the Moon Flyby approach: not all the search grid points are reachable with a 1-revolution transfer.

To assess the cost in terms of propellant mass to reach the 80 encounter locations, LowWiz ran eight times: four runs (0 to 3 revolution trajectories) for the direct transfer strategy, with SEL2 as the departure

point; four runs (0 to 3 revolution trajectories) for the moon gravity assist, departing from Earth's SOI with a  $v_\infty < 1.4 \text{ km s}^{-1}$ . Each LowWiz run solved 80 trajectory optimization problems yielding feasible trajectories as shown in Figure 5.1 for a Moon Flyby 1-revolution transfer run. The optimization was not concerned with the arrival velocity. The CReMA assumes that a spacecraft arriving to a circular orbit with  $r = R_c$  is expected to encounter the Comet at a relative velocity under  $70 \text{ km s}^{-1}$ .

The  $\Delta v$  required to perform the trajectories in Figure 5.1 are used to generate  $\vartheta$ - $m_p$  maps, i.e., maps that specify the propellant mass required to reach a given Comet-Sun-Earth angle. The maps are divided into 0, 1, 2 and 3 revolution trajectories plots. Each map shows the results for different values of  $R_c$  and the trajectories obtained with the Direct Transfer strategy and Moon Flyby strategy.

### 0-revolution transfers

For 0-revolution transfers twenty trajectories were made feasible covering seventeen  $R_c$ - $\vartheta$  pairs of the 80 points in the search grid. Encounters with  $R_c < 1 \text{ au}$  and  $\vartheta < 0^\circ$  are reachable with a Moon gravity assist, whereas transfers to  $R_c > 1 \text{ au}$  and  $\vartheta > 0^\circ$  are favored by a Direct Transfer.

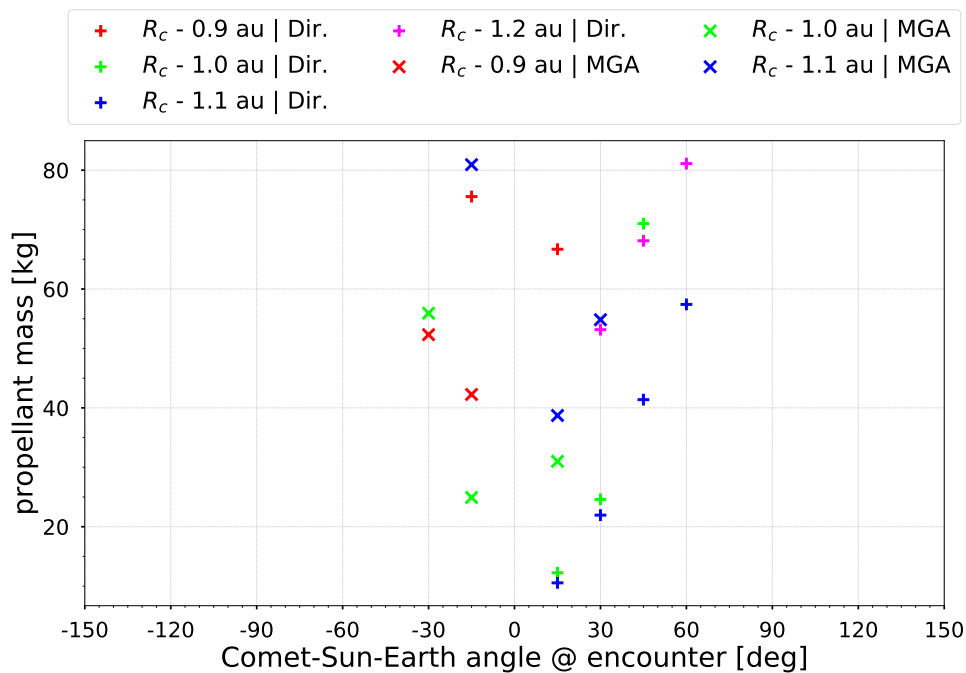


Figure 5.2: 0-revolution propellant mass map for EP transfers. Dir are direct transfers; MGA are Moon Gravity Assist transfers.

### 1-revolution transfers

1-revolution transfers reach more encounter locations: feasible trajectories were found for all but four of the encounter locations, specified in Table 5.2. For 1-revolution transfers, the patterns identified for the 0-revolution case are reiterated: the Moon gravity assist favours encounters with  $R_c < 1 \text{ au}$  and  $\vartheta < 0^\circ$  transfers and the direct transfer strategy favours  $R_c > 1 \text{ au}$  and  $\vartheta > 0^\circ$ . The data in Figure 5.3 exhibit encounter locations reachable with both transfer strategies. Also, the two strategies complement each

other: the Moon gravity assist strategy allows for encounters where they are not possible with a direct transfer and vice-versa.

Table 5.2: Unfeasible encounter locations for 1-revolution trajectories.

$R_c$ (au)	$\vartheta$ ( $^\circ$ )
1	-150
1.1	-120
1.2	-105
0.9	150

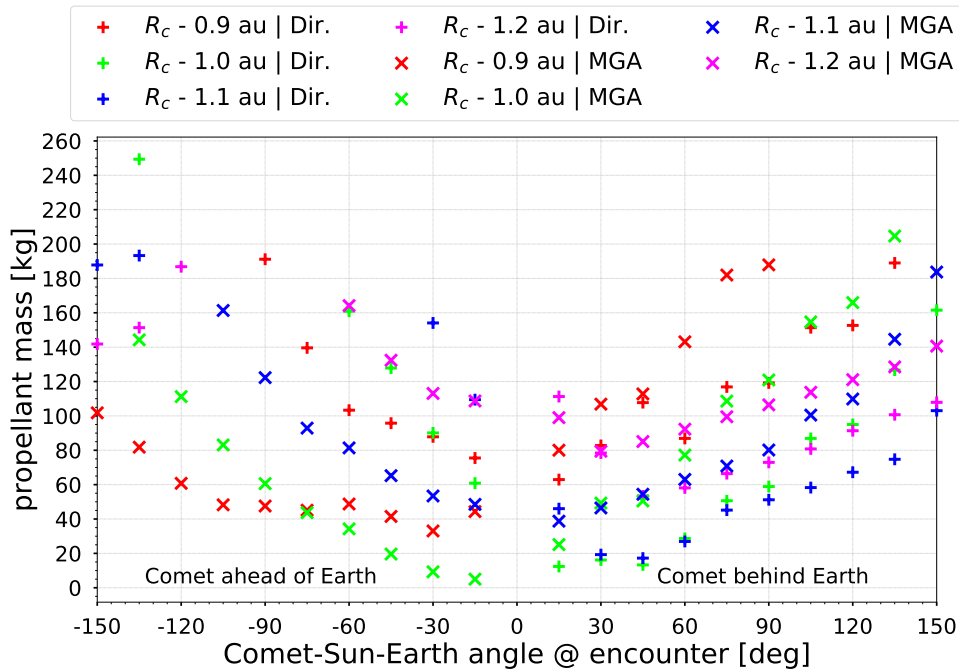


Figure 5.3: 1-revolution propellant mass map for EP transfers. Dir are direct transfers; MGA are Moon Gravity Assist transfers.

## 2-revolution transfers

With 2-revolution trajectories, both strategies cover almost the entire search grid but still the complementary behaviour is noted: the Moon gravity assist strategy performs better where the direct transfer strategy performs poorly and vice-versa. To reach the same encounter location, the 2-revolution trajectory requires less propellant mass than a 1-revolution trajectory.

## 3-revolution transfers

Transfers with 3-revolutions reach the entire search domain with both strategies. The complementary behaviour noted in the 1 and 2-revolution case is again present and the propellant mass requirements are lowered with respect to the 0, 1 and 2-revolution trajectories.

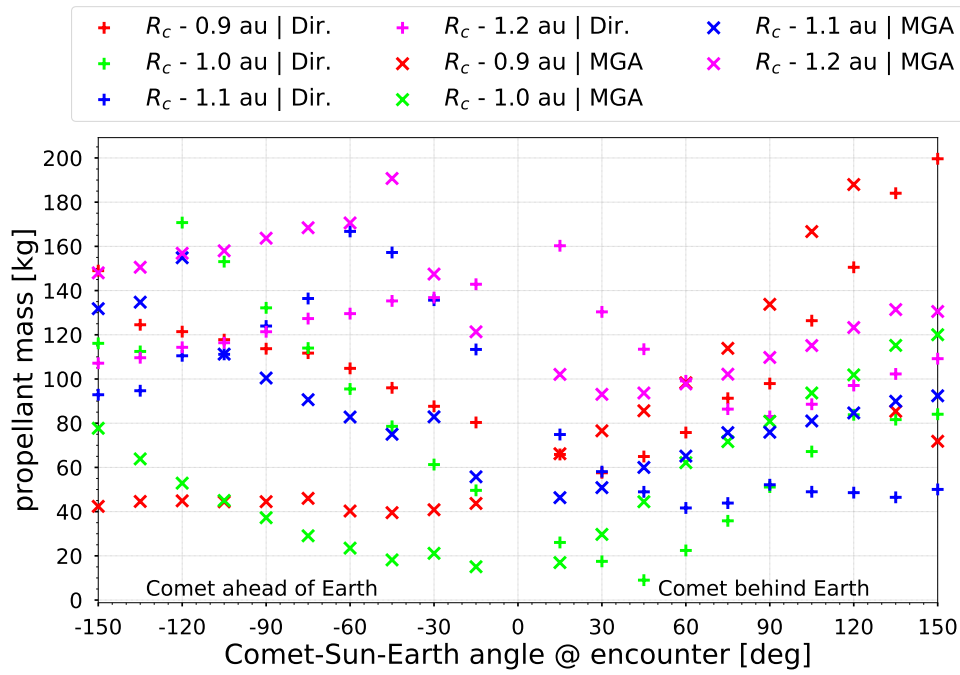


Figure 5.4: 2-revolution propellant mass map for EP transfers. Dir are direct transfers; MGA are Moon Gravity Assist transfers.

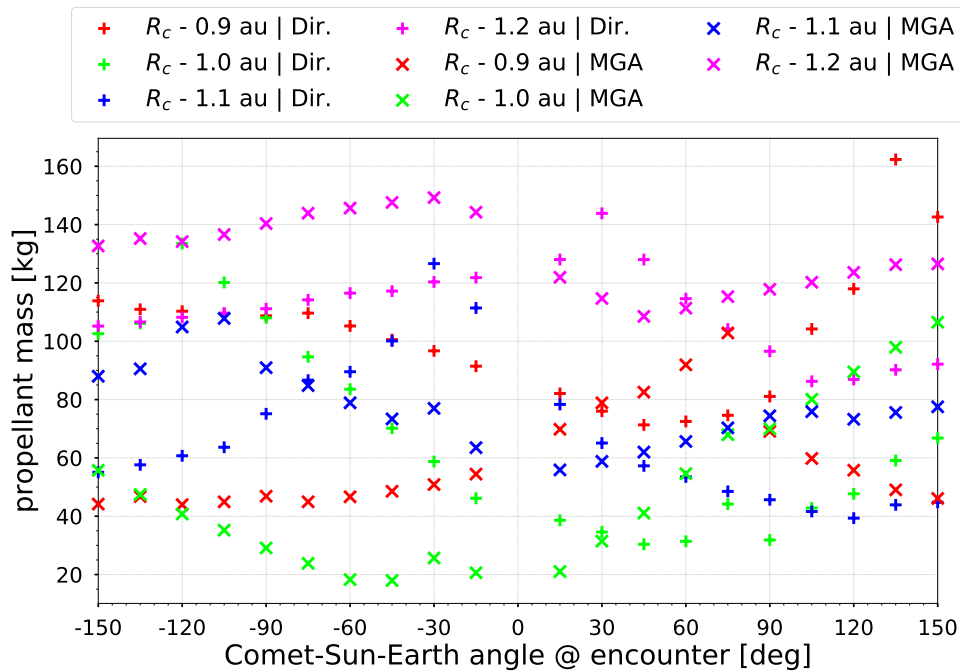


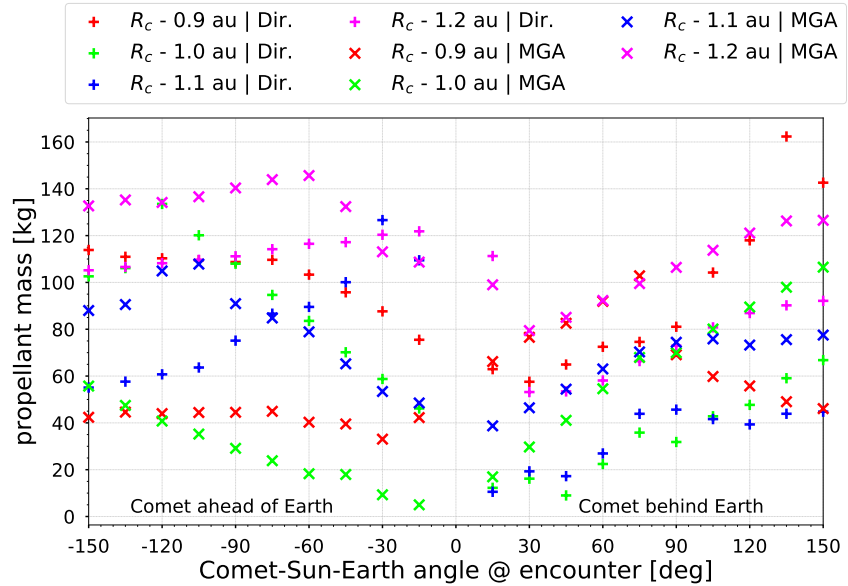
Figure 5.5: 3-revolution propellant mass map for EP transfers. Dir are direct transfers; MGA are Moon Gravity Assist transfers.

### 5.1.1 Selected transfers

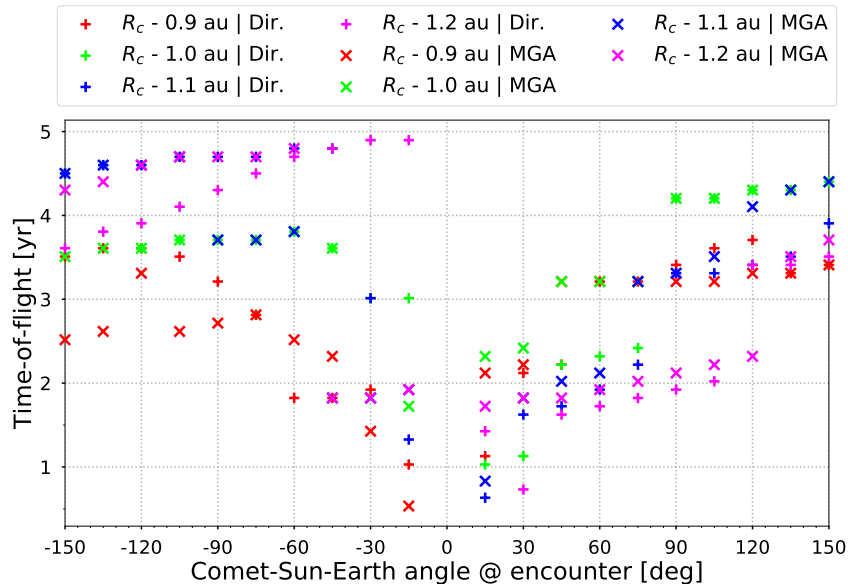
As observed in Figures 5.1 to 5.4, not all the combinations of  $R_c$ ,  $\vartheta$  and number of revolutions yield feasible EP trajectories: the encounter locations defined by these combinations are not reachable, given the propulsion system constraints. When more than one trajectory is found for an  $R_c$ - $\vartheta$  combination the need to define a criteria to select the appropriate solution appears. The criteria can be according to

propellant mass or time-of-flight. If the criteria is the former, the trajectory that minimizes the propellant mass is selected and a bias towards longer, more fuel efficient trajectories is introduced; if it is the latter, the shortest trajectory is selected and a bias to less efficient but shorter trajectories is introduced.

Figure 5.6 illustrates the selection process according to propellant mass. From the set of trajectories in Figures 5.2 to 5.5, if more than one solution for a  $R_c$ - $\vartheta$  pair exists, the one that minimizes  $m_p$  is selected, originating the maps for propellant mass and time-of-flight, respectively in Figures 5.6a and 5.6b.



(a) Propellant mass.



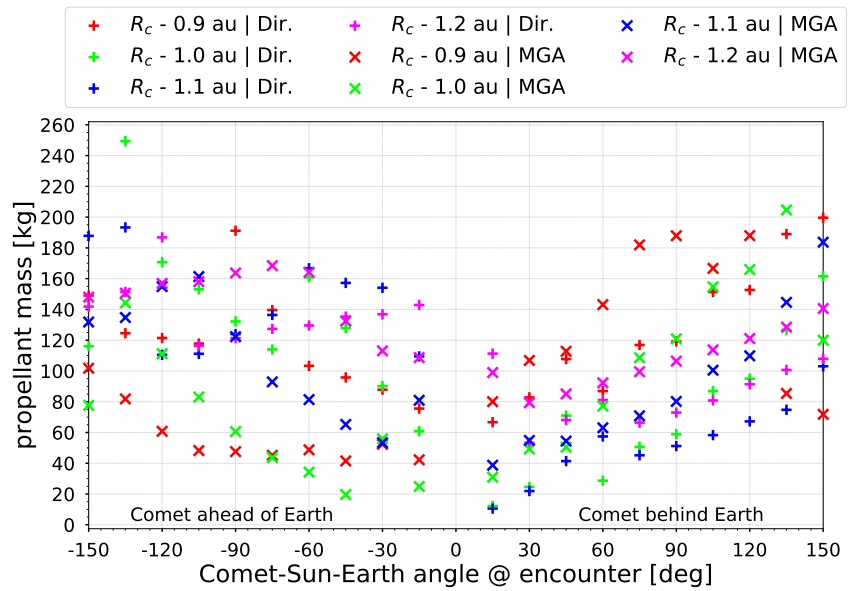
(b) Time-of-flight.

Figure 5.6: Selected EP transfers (lowest propellant mass trajectory is selected for each  $R_c$ - $\vartheta$  pair). Dir are direct transfers; MGA are Moon Gravity Assist transfers.

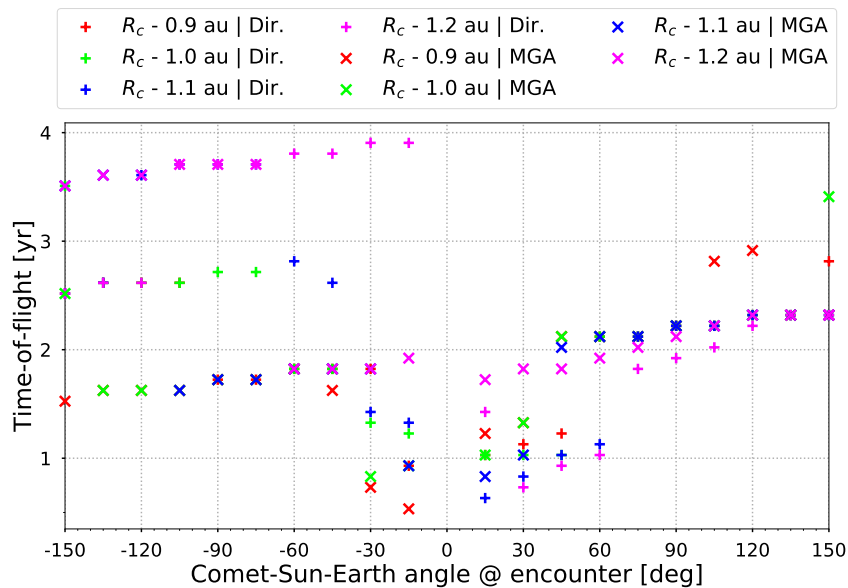
Figure 5.6a shows that all the encounter locations are reached with a propellant mass under 160 kg; Figure 5.6b shows that all encounter locations are reached with a time-of-flight under 5 years.

Figure 5.7 illustrate the selection process according to time-of-flight. From the set of trajectories in

Figures 5.2 to 5.5, if more than one solution for a  $R_c$ - $\vartheta$  pair exists, the one that requires the lowest time-of-flight is selected, originating the maps for propellant mass and time-of-flight, respectively in Figures 5.7a and 5.7b.



(a) Propellant mass.



(b) Time-of-flight.

Figure 5.7: Selected EP transfers (lowest time-of-flight trajectory is selected for each  $R_c$ - $\vartheta$  pair). Dir are direct transfers; MGA are Moon Gravity Assist transfers.

Figure 5.7a shows that the propellant mass to reach all the encounter locations increases in comparison with Figure 5.6a (260 kg against 160 kg); Figure 5.7b shows that all encounter locations are reached with a time-of-flight under 4 years if the bias towards shorter trajectories is chosen.

## 5.1.2 Comparison with Chemical Propulsion transfers

CP systems generally perform high thrust impulsive maneuvers; EP systems work for longer periods of time as a result of their low thrust capabilities hence are continuous propulsion systems. The trajectory dynamics are different.

Considering CP maneuvers as instantaneous is a good first approximation. Consequently, the required  $\Delta v$  for a CP transfer can be easily related to the required propellant mass using the Tsiolkovsky Rocket Equation (5.1)

$$\Delta v = I_{sp}g_0 \ln \left( \frac{m_0}{m_f} \right), \quad (5.1)$$

which can be rewritten as Equation (5.2) to yield the propellant mass,  $m_p$ .

$$m_p = m_0 - m_f = m_0 \left( 1 - \exp \left( -\frac{\Delta v}{I_{sp}g_0} \right) \right) \quad (5.2)$$

For EP continuous propulsion trajectories, the  $\Delta v$  is suitable as a measure of the change in velocity to accomplish a given trajectory. However, there is no direct relation to compute the propellant mass from the  $\Delta v$  for continuous propulsion trajectories. Also, EP trajectories typically have a higher  $\Delta v$  than CP trajectories: EP systems apply thrust in non-optimal locations whereas CP typically perform  $\Delta v$  optimal or close-to-optimal maneuvers at the perigee and apogee of the transfer orbit (Hohmann transfers). Additionally, a greater  $\Delta v$  does not imply higher propellant mass demands thanks to the typically high  $I_{sp}$  values of EP.

The fundamental difference in how the  $\Delta v$  relates to propellant mass for CP and EP systems distorts a comparison between both systems if such comparison is made based on  $\Delta v$ . Instead, the propellant mass itself is a comparable metric for the performance of each of these systems. Moreover, by comparing both systems in terms of required propellant mass, the choice between CP and EP can be objectively assessed in terms of its impact on the spacecraft dry mass.

The available data in the CReMA for CP transfers reports the  $\Delta v$  required to reach different encounter locations. To extract the values for propellant mass the  $\Delta v$  values in the CReMA Data Appendix B, Figure B.1a were inserted in the rewritten Tsiolkovski Rocket Equation (5.2) with an initial mass,  $m_0$ , of 750kg and the  $I_{sp}$  was assumed to be 300s, a typical value for chemical propulsion systems [71, p. 688].

Besides the propellant mass comparison, both systems were compared in terms of time-of-flight. The CReMA results for propellant mass (extrapolated here from the  $\Delta v$  maps) and time-of-flight are available for reference in Figures B.2a and B.2b, respectively. From Figure B.2a the CReMA concludes that 280kg of propellant are required to cover the search domain and from Figure B.2b that transfer times under 4.6yr suffice to reach all the  $R_c$ - $\vartheta$  points.

The results from the selected EP trajectories — for minimum propellant in Figure 5.6 and minimum for time-of-flight in Figure 5.7a — were superimposed to the CReMA results from Figure B.2a and Figure B.2b.

## Comparison of minimum propellant mass trajectories

In Figure 5.8a, the accumulation of red points (EP) below the cluster of black points (CP) asserts the overall tendency: the EP system requires less propellant mass than CP for transfers to the same encounter position. Figure 5.8b shows the boxplot for the propellant mass saving when using EP: each datum in the set of CP and EP solutions corresponding to the  $R_c$ - $\vartheta$  pairs and transfer strategy (direct or moon gravity assist) are compared; positive values in Figure 5.8b (propellant mass) and Figure 5.9b (time-of-flight) correspond to encounter locations where EP reduce the propellant mass and time-of-flight, respectively.

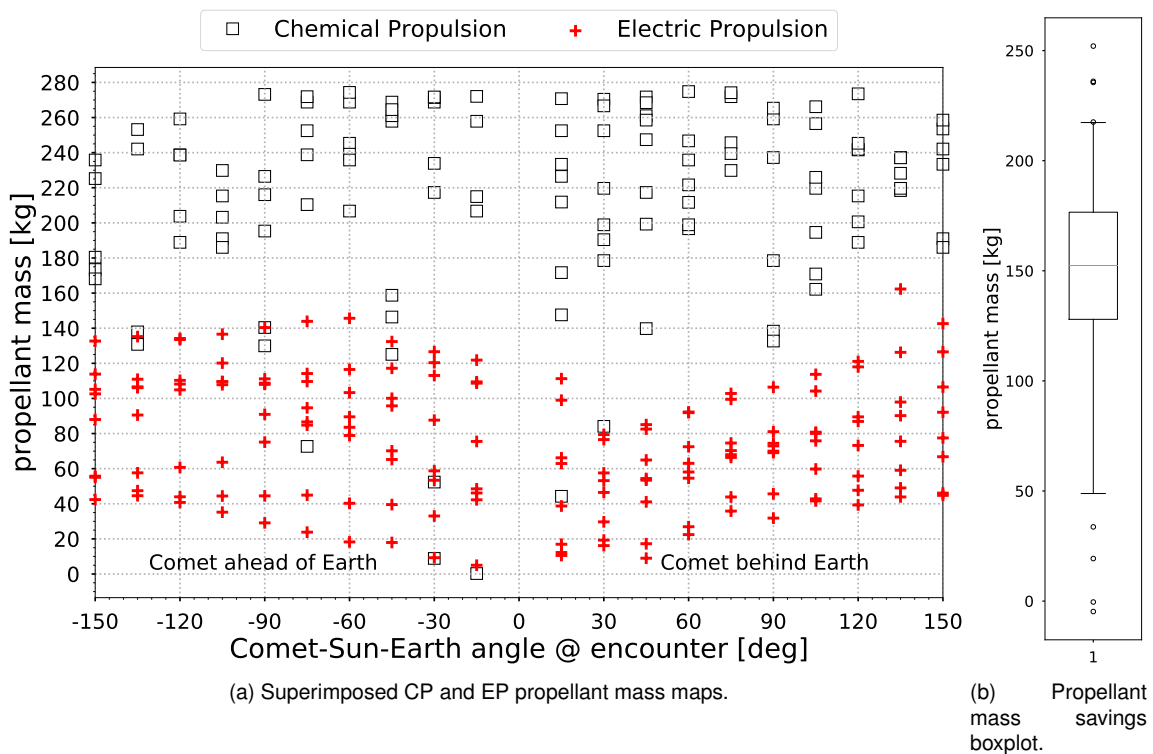


Figure 5.8: CP vs EP propellant mass comparison for minimum propellant mass trajectories.

Particularly, Figure 5.8b tells that the propellant mass saving for 75 % of the encounter locations is greater than 125 kg; for 50 % of the encounter locations the mass saving when using EP is more than 150 kg. In the worst case scenario, the spacecraft would not improve the propellant mass requirements compared to a CP trajectory.

Figure 5.9 shows the time-of-flight comparison between EP and CP transfers. Positive values in Figure 5.9b correspond to trajectories that required less time-of-flight with EP than with CP; negative values correspond to trajectories that require more time using EP. Notably, EP transfers require less time-of-flight for at least 50 % of the encounter locations; the time of flight for 25 % of the encounter locations is decreased in more than 6 months. In the worst case scenario an EP trajectory would require 3 years of additional time-of-flight. The data shows that the savings in propellant mass observed in Figure 5.8 carry an increase in time-of-flight for the remaining 50 % of the trajectories.

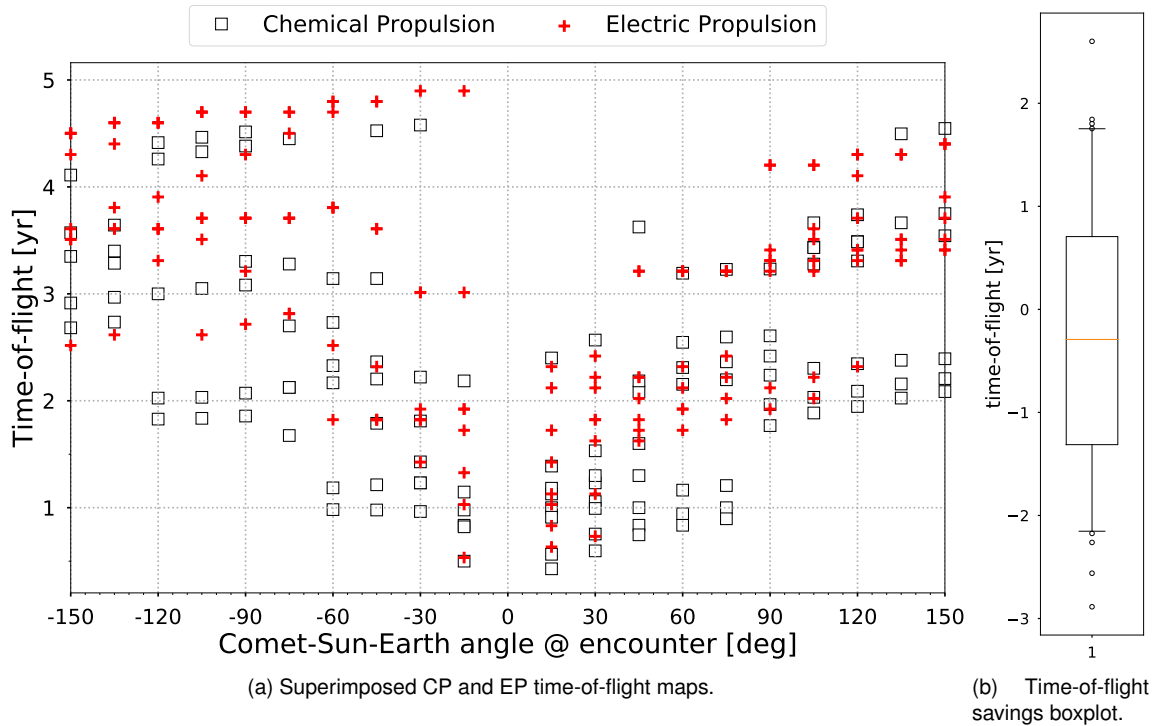


Figure 5.9: CP vs EP time-of-flight comparison for minimum propellant mass trajectories.

### Comparison of minimum time-of-flight trajectories

The overall tendency from Figure 5.8a is maintained in Figure 5.10a, i.e., the propellant mass requirements are lowered by EP. Figure 5.8b shows that minimizing time-of-flight carries penalties in the pro-

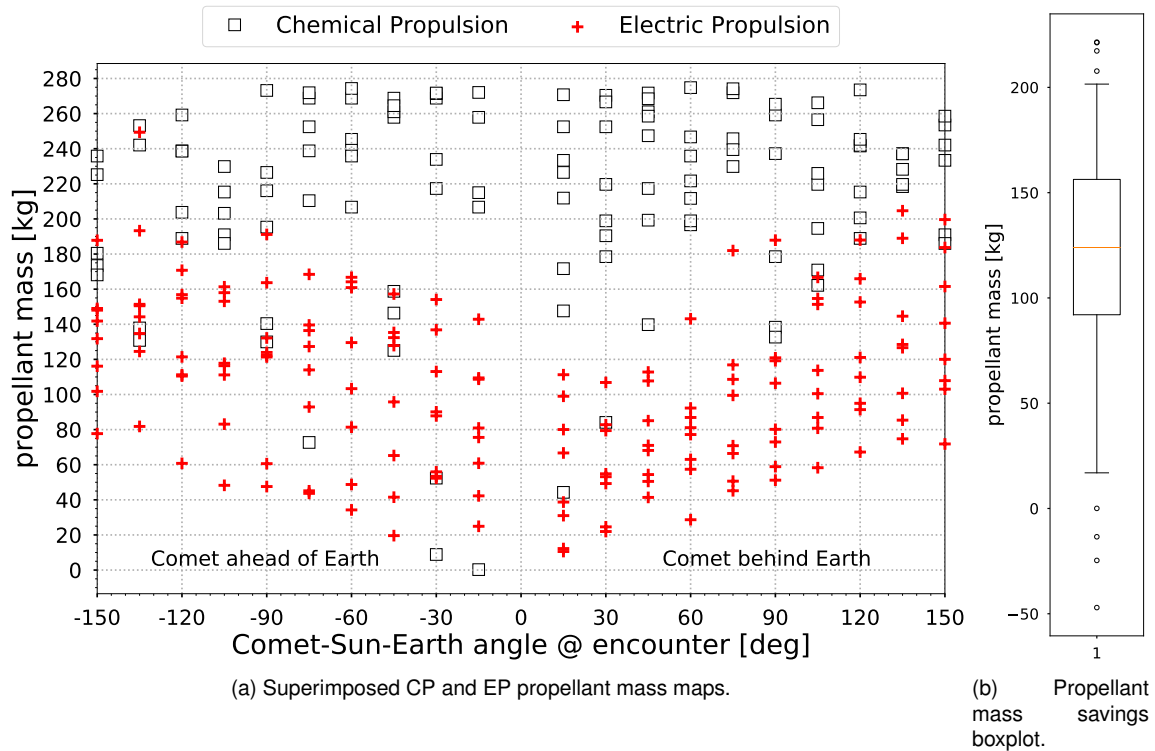


Figure 5.10: CP vs EP propellant mass comparison for minimum time-of-flight trajectories.

pellant mass: in the worst case scenario in Figure 5.10, the spacecraft carries an additional 50 kg of EP propellant to reach the same encounter location with CP. Still, for more than 75 % of the trajectories the propellant mass savings are higher than 90 kg.

Figure 5.9 shows that, when minimizing the time-of-flight, in the worst case scenario EP still under performs compared to CP (more than 1 year). Nonetheless, the, 75 % of the trajectories require less time-of-flight with EP compared to CP.

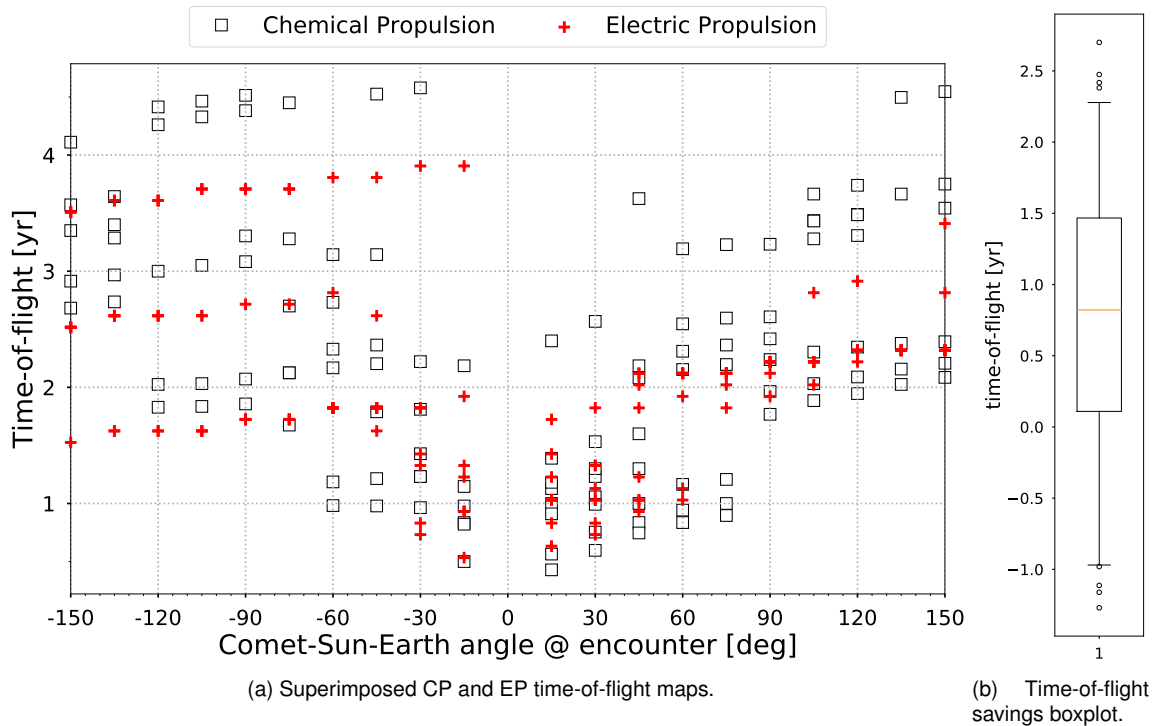


Figure 5.11: CP vs EP time-of-flight comparison for minimum time-of-flight trajectories.

The overall performance comparison is shown in Table 5.3. If the main objective is to minimize the propellant mass, the worst case scenario takes 3 additional years with EP compared to CP. Nonetheless all the EP trajectories improve on the CP solutions. Oppositely, if the main objective is to minimize the time-of-flight, the worst case scenario requires additional 50 kg to perform the transfer. Also, the EP trajectories that minimize time-of-flight do not improve every CP solution: in the worst under-performing case the EP trajectory requires an additional year to reach the target.

Nonetheless, the gains provided by EP can reach 250 kg in propellant mass savings and up to 2.6 years of time-of-flight reduction.

Table 5.3: Overall comparison of EP against CP.

Selection criteria	Minimum $m_p$	Minimum $\Delta t$
Propellant mass savings (kg)	0 to 250	-50 to 220
Time-of-flight difference (years)	-3 to 2.4	-1.3 to 2.6

### 5.1.3 Full Engine Capacity

The Electric Propulsion results obtained in Section 5.1.2 simulated the baseline version of an EP system specified in the CReMA. However, the baseline version does not leverage the engine's full capacity because, at 1 au, it only provides half of the engine's maximum input power. To quantify the possible propellant mass savings of using the engine at its full capacity, the baseline version is compared to an alternative system that provides 2 kW at 1 au.

Figure 5.12a shows that using the engine at its full capacity brings net gains on propellant mass savings. Specifically, Figure 5.12a tells that all encounter locations are reached with less propellant mass with the alternative system; for 50% of the trajectories, the mass saving is higher than 15 kg. Regarding time-of-flight, the improvements cannot be generalized and two encounter locations even require up to 6 months of additional time-of-flight.

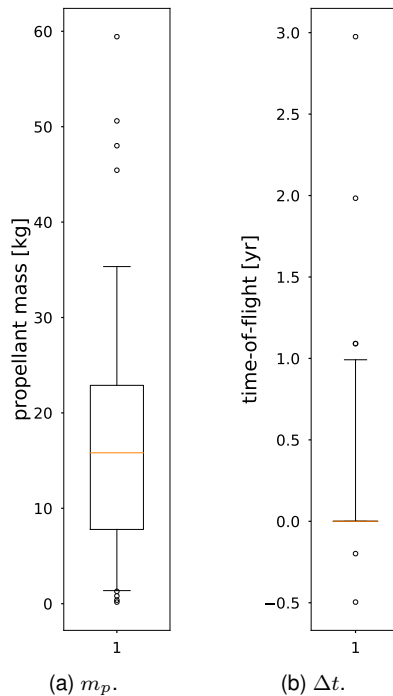


Figure 5.12: Comparison between baseline engine power and engine at full capacity (positive values are a decrease in the quantities for the engine at full capacity system).

## 5.2 Transfer to backup target 73P/Schwassmann-Wachmann

An analysis for the backup target 73P is made in the CReMA. The CReMA analysis considered the propulsion system's limitations in terms of maximum thrust; limited the coast-thrust-coast structure to only two thrust arcs; did not include the pre-arrival coast-arc in the optimization (but verified this a posteriori); included the Earth's effect on the dynamics. The analysis made with LowWiz and here presented aims at expanding the results in the CReMA. Specifically, this analysis considers the available engine model for the propulsion system; does not limit the coast-thrust-coast structure; includes the pre-

arrival coast-arc in the optimization; includes the Earth's effect in the dynamics.

LowWiz searched for trajectories departing in or after 2030 and before 2034 with a time-of-flight between 100 and 1200 days with a step of 20 days for both the departure and time-of-flight search. The search yielded 4478 candidate trajectories using the approximate trajectory model described in the Initial Guess Generation Section 3.4. Approximate trajectories with a  $\Delta v$  below  $20\text{km s}^{-1}$  were used to plot the  $\Delta v$  contour of the departure window in Figure 5.13.

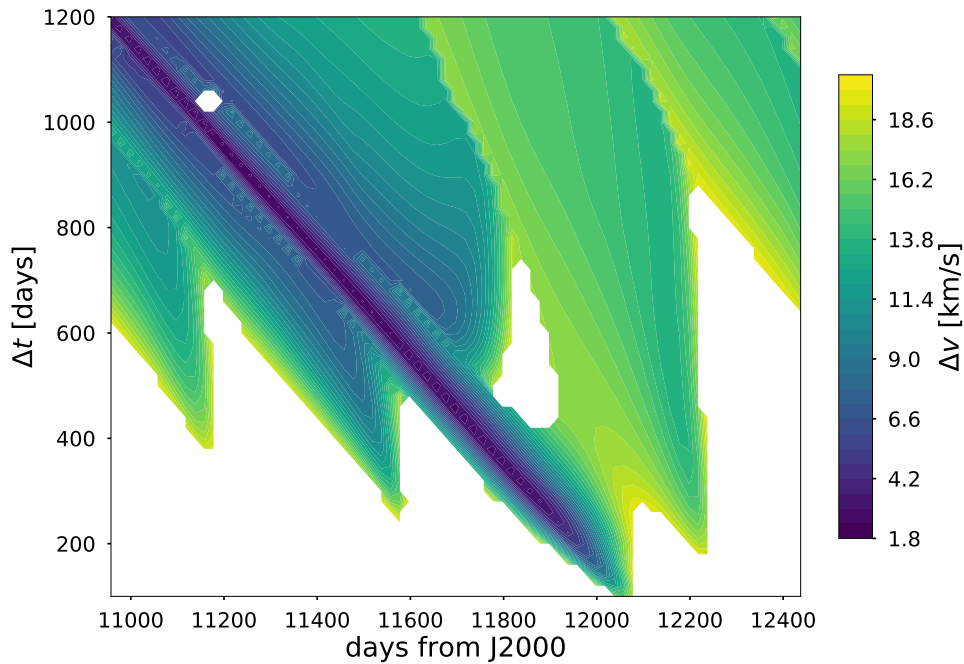


Figure 5.13:  $\Delta v$  contour for candidate trajectories for a 73P transfer.

Figure 5.13 shows that low  $\Delta v$  transfers ( $\Delta v < 2\text{ km s}^{-1}$ ) are possible for a wide range of departure dates and transfer duration. These low  $\Delta v$  trajectories, accumulated in the darkest area of the contour correspond to transfers that encounter the comet at its crossing of the ecliptic in April 2033. By meeting the target at the ecliptic, an inclination change is not required to reach the comet and less  $\Delta v$  is needed.

From the 4478 candidate trajectories, 10 were selected for further optimization, 9 of which were found to be feasible; the optimized trajectories are listed in Table 5.4. The optimization uses 200 discretization. The discretization points are not spaced evenly: at the beginning of the trajectory the segments are shorter (smaller time step) to account for rapidly changing dynamics caused by the Earth's gravity effect when departing from SEL2. The optimized trajectories differ in terms of launch dates, time-of-flight,  $\Delta v$  requirements and coast-thrust-coast structure. However, as predicted by Figure 5.13, all the solutions encounter the comet in April 2033 because this period contains the asteroid's crossing of the ecliptic.

The trajectories in Table 5.4 are ordered according to increasing propellant mass. It was expected that the time-of-flight evolved inversely: the higher the time-of-flight, the lower the required propellant mass. However, the trade-off between time-of-flight and propellant mass is not noticeable in the trajectories in Table 5.4. This behaviour was predicted in the contour plot Figure 5.13, where low  $\Delta v$  trajectories were possible for the majority of the time-of-flight values.

Table 5.4: Feasible trajectories for 73P.

Departure	Encounter	time-of-flight (d)	$\Delta v$ (km s <sup>-1</sup> )	Propellant Mass (kg)	# thrust arcs
29-MAY-2032	08-APR-2033	314	0.29	16	1
18-SEP-2030	28-APR-2033	954	0.29	17	2
18-JUN-2032	05-APR-2033	291	0.30	17	1
09-AUG-2030	29-APR-2033	995	0.36	20	3
24-JUN-2031	08-APR-2033	654	0.58	32	3
12-NOV-2031	11-APR-2033	516	0.61	33	3
15-JUL-2031	11-APR-2033	637	0.63	34	3
07-DEC-2030	26-APR-2033	871	1.12	61	4
10-APR-2030	15-APR-2033	1100	1.66	85	4

### Comparison with the CReMA solutions

The solutions presented in the CReMA for the transfer to 73P are grouped into 0 and 1-revolution transfers where three solutions were presented for three different values of the thrust-to-mass ratio,  $T/m$ . The thrust-to-mass ratio restriction is actually a simplification and is not implemented in LowWiz. Instead, LowWiz uses the engine performance model. The  $T/m$  value for the LowWiz trajectories is computed a posteriori. Additionally, the thrust program of the trajectories are compared; in Tables 5.5 and 5.6, T and C indicate respectively, a thrust and a coast arc.

Quantitatively, the performance metrics to compare the trajectories are the time-of-flight and required  $\Delta v$ . Comparing the propellant mass as in the Probing Encounter Locations Section 5.1 is not possible because there is no available data to integrate the acceleration profile of the CReMA solutions. Nevertheless, the  $\Delta v$  comparison is fair because both solutions simulated an EP system.

The 0-revolution trajectories are reported in Table 5.5. The trajectory obtained with LowWiz requires less  $\Delta v$  and time-of-flight than the trajectories proposed in the CReMA. Additionally, the trajectory requires only one thrust arc at the start of the transfer, shown in Figure 5.14. Figure 5.15 shows that the initial thrust arc exploits the Earth's gravity and sets the spacecraft on course to encounter the target, delivering the best trajectory in terms of  $\Delta v$ .

Table 5.5: 0-revolution transfers from the CReMA (CR) and best LowWiz solution (L).

Source	$T/m$ (mN kg <sup>-1</sup> )	Thrust Program (Arc duration in days)	$\Delta t$ (d)	$\Delta v$ (km s <sup>-1</sup> )
CR	0.05	T-C-T-C (187-106-215-48)	452	1.036
CR	0.1	T-C-T-C (93-144-166-19)	384	0.985
CR	0.2	T-C-T-C (50-168-49-3)	359	0.923
L	0.065	T-C (50-264)	314	0.29

For 0-revolution transfers (see Table 5.5), a significantly cheaper trajectory (requiring 30% of the  $\Delta v$

from the CReMA solutions) is found with LowWiz: this result is possible because there is no constraint on the number of thrust arcs, whereas the CReMA solutions assume two powered arcs.

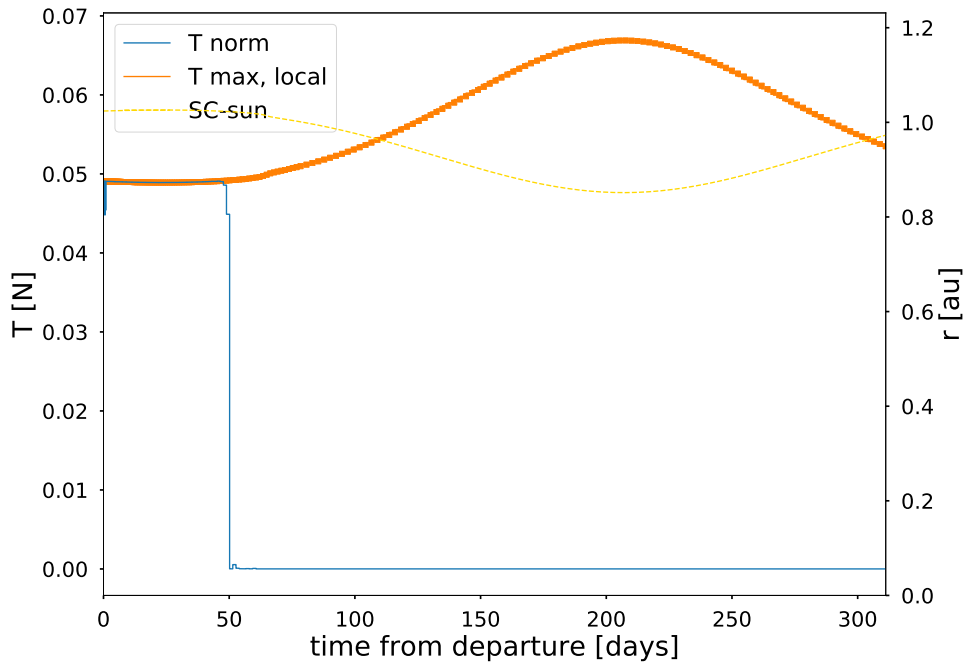


Figure 5.14: Thrust profile for minimum  $\Delta v$  transfer for 73P

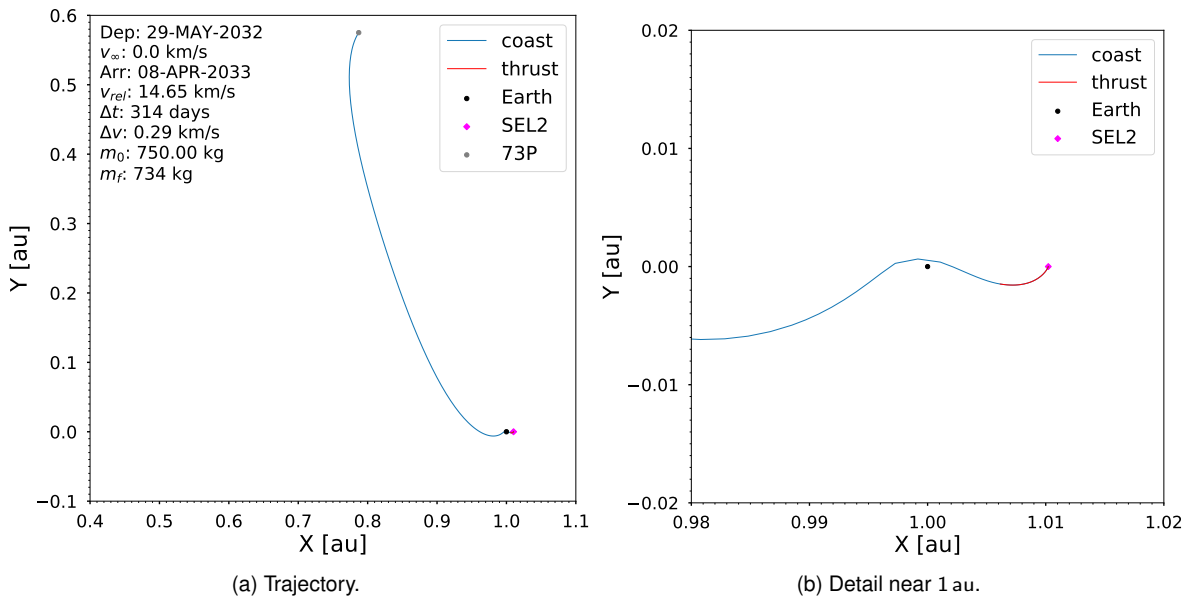


Figure 5.15: Minimum  $\Delta v$  trajectory for a 73P transfer.

1-revolution solutions are listed in Table 5.6. As in the 0-revolution case, the LowWiz solution requires less than 200 d of time-of-flight compared to the CReMA trajectories; in terms of  $\Delta v$  the CReMA solution for  $T/m = 0.05$  performs the transfer with  $20 \text{ m s}^{-1}$  less than the LowWiz solution but the LowWiz trajectory requires  $60 \text{ m s}^{-1}$  less than the remaining trajectories. Additionally, the thrust program of the solution here presented differs to the solutions from the CReMA: all the 1-revolution trajectories require two short thrust arcs ( $\Delta t_{thrust} < 100 \text{ d}$ ) whereas the LowWiz trajectory implements one thrust arc to

leave SEL2, a second thrust-arc when leaving the Earth's Sphere of Influence and a mid-course thrust arc, show in Figure 5.17. Thus the solution found by LowWiz favours a longer intermediate coast arc ( $\Delta t_{coast} > 200$  d) delivering an arrival coast-arc more than 300 d shorter than all the CReMA solutions and consequently reducing the transfer duration.

Table 5.6: 1-revolution transfers from the CReMA (CR) and best LowWiz solution (L).

Source	$T/m$ ( $\text{mN kg}^{-1}$ )	Thrust Program (Arc duration in days)	$\Delta t$ (d)	$\Delta v$ ( $\text{km s}^{-1}$ )
CR	0.05	T-C-T-C (86-173-43-496)	798	0.56
CR	0.1	T-C-T-C (57-170-20-528)	775	0.677
CR	0.2	T-C-T-C (29-205-10-527)	771	0.691
L	0.075	T-C-T-C-T-C (15-15-30-285-63-108)	516	0.61

The best 1-revolution solution from LowWiz is shown in Figure 5.16 where the initial thrust arc is shown to drift the spacecraft towards positions that exploit the dynamics of the three-body problem. When compared with the 0-revolution solution, the 1-revolution trajectory requires  $\approx 200$  d of additional time-of-flight and twice the  $\Delta v$  but the arrival velocity relative to 73P is decreased from  $14.65 \text{ km s}^{-1}$  to  $11.49 \text{ km s}^{-1}$ .

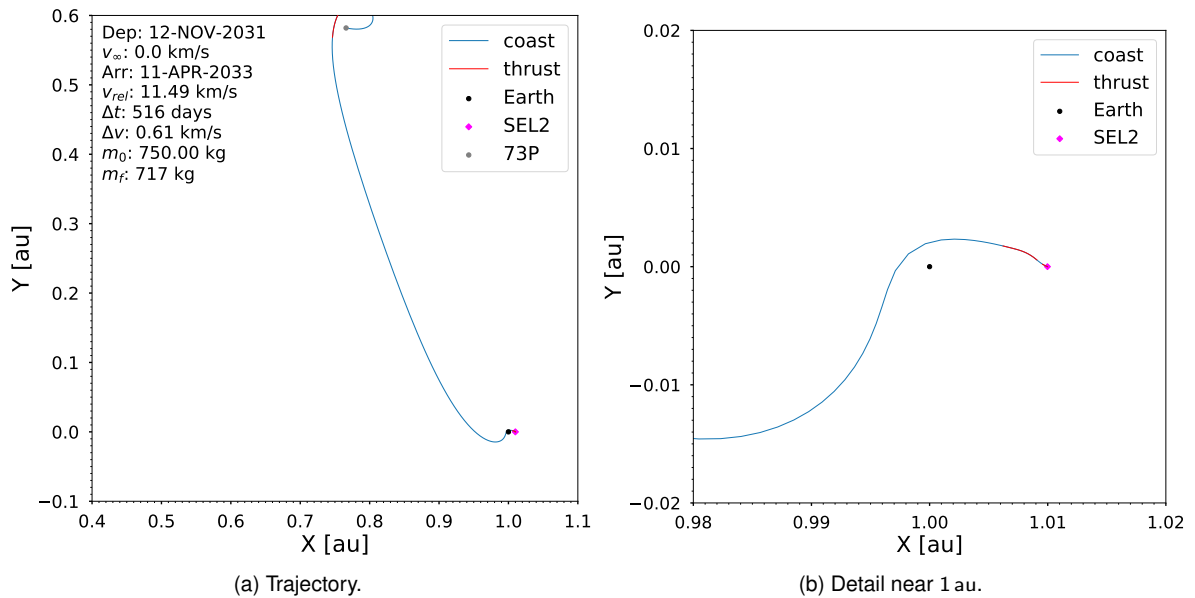


Figure 5.16: Best 1-revolution solution found with LowWiz.

The control profile for the best 1-revolution solution, show in Figure 5.17, is made of three powered arcs: one to leave SEL2 and drift towards Earth; one to leave the Earth SOI and a third to adjust the trajectory before the arrival coast arc. Despite the irregularities in the control, the solution in Figure 5.17 is still very close to a bang-bang control profile.

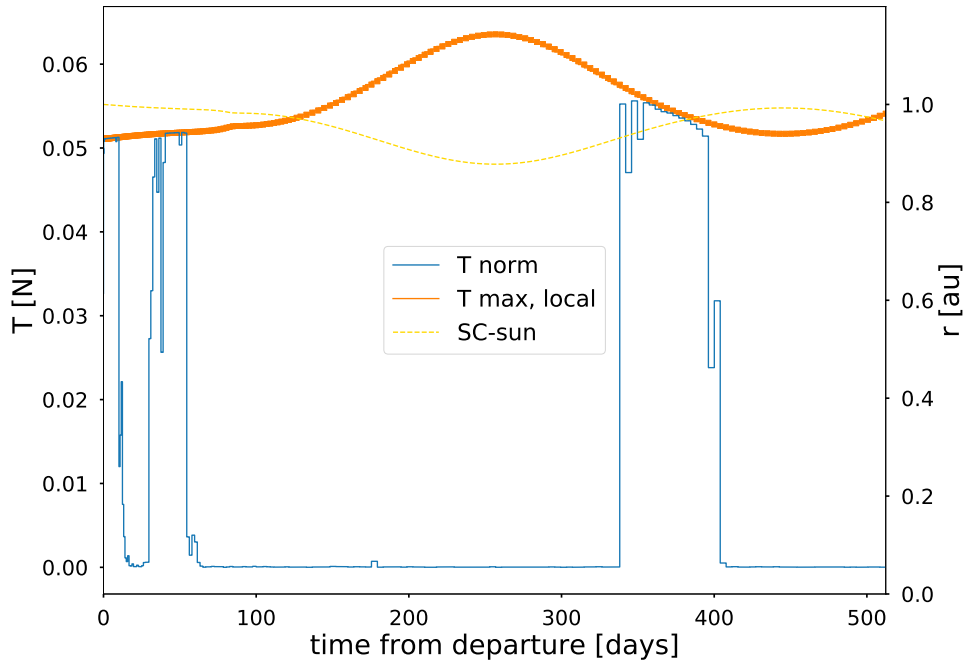


Figure 5.17: Thrust profile for minimum  $\Delta v$  transfer for 73P

### 5.3 Trade Studies

For the backup target analysis the baseline capabilities of LowWiz — engine and input power trade studies — were exploited to perform trade studies. These two analysis are relevant to quantify the performance gain of realistic alternatives to the baseline propulsion system.

#### Alternative engines

From the available engines in LowWiz, the choice for the trade study are the XIPS and NSTAR engines. These two engines, together with the BPT-4000 have operating power ranges compatible with the mission baseline. The chosen engines are preferred over the BPT-4000 because they deliver approximately twice the specific impulse of the BPT-4000 at nominal input power.

Table 5.7: Considered engines data for the engine trade study.

Engine	PPS 1350-G	XIPS	NSTAR
Thrust (mN)	40	29	28
Specific Impulse (s)	1219	2550	2174
Operating Power Range (kW)	0.46 to 1.5	0.436 to 5.03	0.450 to 3.8
EP Unit Mass (kg)	29	112	151
Reference	[56] <sup>1</sup>	[60, 72] <sup>2</sup>	[60]

The output of the analysis are propellant mass curves as a function of time-of-flight for the different engines. These results were obtained incrementally: a first LowWiz run was made neglecting the Earth's

<sup>1</sup>EP Unit Mass obtained from <https://earth.esa.int/web/eoportal/satellite-missions/s/smart-1>, last accessed on December 20th, 2020.

<sup>2</sup>EP Unit Mass computed with data from [72] following the method in [60].

gravity effect on the dynamics, bringing forth the results in Figure 5.18; subsequently, a new run where the Earth effect was included generated the curves in Figure 5.19.

In Figure 5.18 a clear trend emerges: the required propellant mass decreases as the time-of-flight increases. This trend is expected as more time-of-flight leaves a bigger margin for the optimization to turn on the engine only at optimal segments of the trajectory. Also, for shorter trajectories (time-of-flight below 800 d) only the PPS 1350-G engine delivers feasible trajectories: for the nominal input power the PPS 1350-G engine delivers approximately 40 % more thrust as the other two engines. For time-of-flight values above 800 d the XIPS and NSTAR engines deliver feasible trajectories, decreasing the required propellant mass by at least 15 kg (25 %) compared to the baseline option. The difference in specific impulse explains the decrease in propellant mass relative to the PPS 1350-G engine and also the better performance of the XIPS compared to the NSTAR.

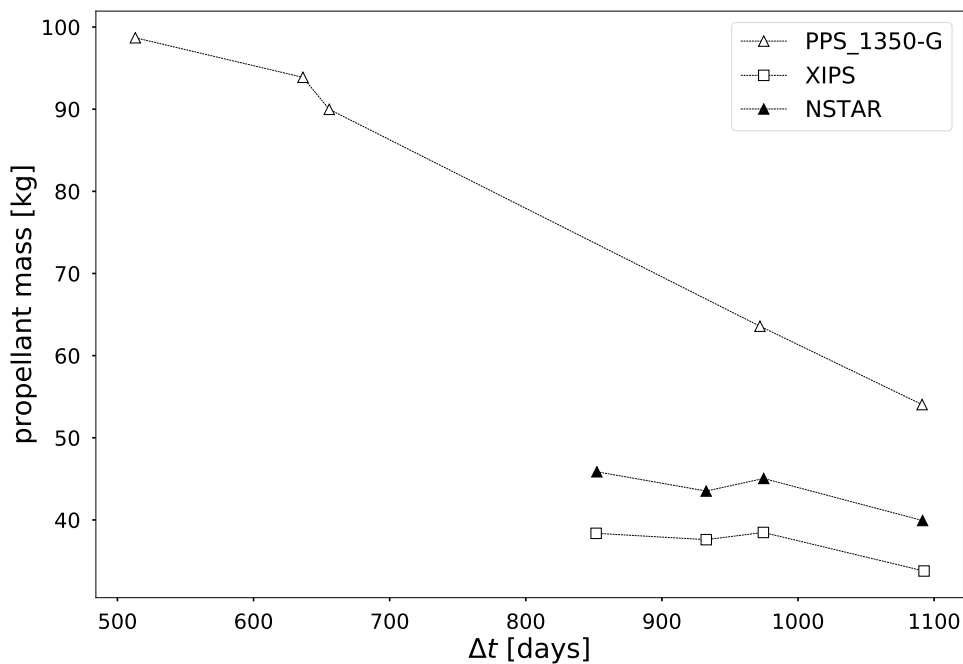


Figure 5.18: Engine trade study output (neglecting Earth's gravity).

The minimum propellant mass savings for the XIPS and NSTAR engines are in Table 5.8; Table 5.8 also shows the net mass gain on the spacecraft mass computed by

$$\text{Net mass gain} = m_{\text{baseline}} - m_{\text{alt.engine}} + \Delta m_p, \quad (5.3)$$

where  $m_{\text{baseline}}$  and  $m_{\text{alt.engine}}$  are, respectively, the PPS 1350 and alternative engine EP unit mass and  $\Delta m_p$  is the propellant mass saving when using the alternative engine.

The net mass gain informs on the performance impact after taking into account the EP unit mass of each propulsion system: despite the alternative options providing minimum propellant mass savings of 25 kg and 19 kg — respectively for the XIPS and NSTAR engines —, the additional unit mass of these systems outweighs their performance gains thus increasing the overall mass of the propulsion subsystem (negative Net mass gain).

Table 5.8: Minimum propellant mass savings for the different engines compared to the baseline option (neglecting Earth's gravity).

Engine	PPS 1350-G	XIPS	NSTAR
$\Delta m_p$ (kg)	-	25	19
Net mass gain (kg)	-	-58	-103

The results considering Earth's gravity are in Figure 5.19: there is no longer a trend for the evolution of propellant mass with time-of-flight. The effect of the Earth's gravity coupled with the target's trajectory is the most likely cause and this is investigated after. Two major considerations are now possible by inspecting the effect of Earth's gravity in the curves: the propellant mass is decreased by at least 50% for analogous trajectories and now the alternative engines (XIPS and NSTAR) deliver trajectories across a wider range of time-of-flight (between 300 d and 1100 d). Besides increasing the fidelity of the analysis, the results in Figure 5.19 show that the dynamics of SEL2 are being leveraged to decrease propellant mass requirements. Additionally, the highest propellant mass saving in Figure 5.19 (31 kg) is not enough to compensate the additional mass of the alternative engines (83 kg and 122 kg for the XIPS and NSTAR, respectively).

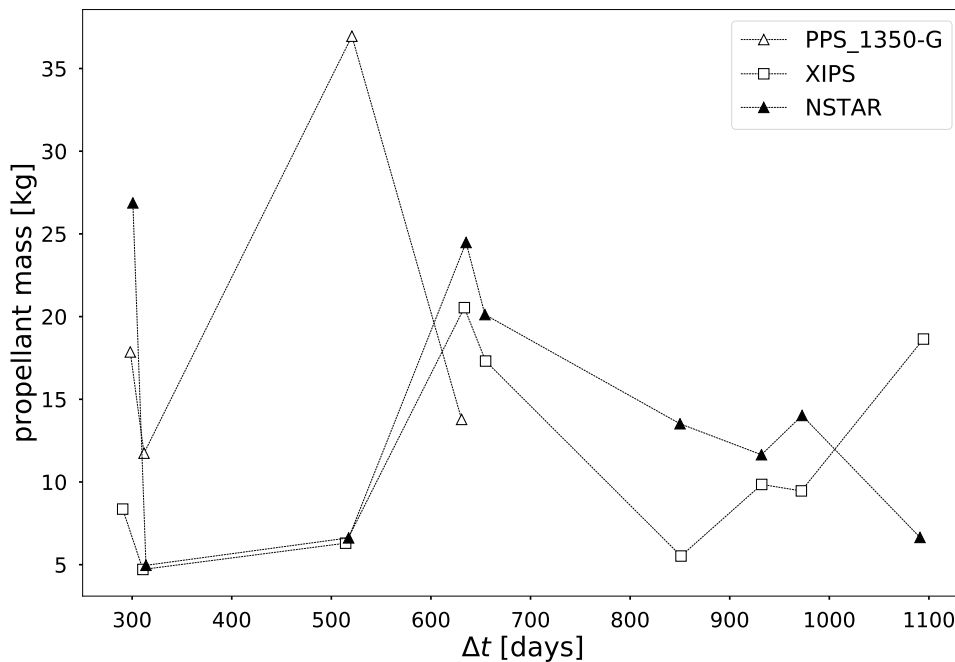


Figure 5.19: Engine trade study output (considering Earth's gravity).

A careful inspection of the Earth's effects on the trajectories explains the difference between the curves in Figure 5.18 and Figure 5.19. Specifically, in Figure 5.20, by analysing the first three trajectories for the PPS 1350-G curve in Figure 5.19 the decrease in propellant mass and the absence of a monotonic curve of propellant mass versus time-of-flight is justified.

The trajectories shown in Figure 5.20 are the first three trajectories of the PPS 1350-G curve in Figure 5.19. These trajectories have similar encounter positions with the comet: the optimization pushes the arrival date to April 2033, as expected from the results in Figure 5.13. Consequently, because the

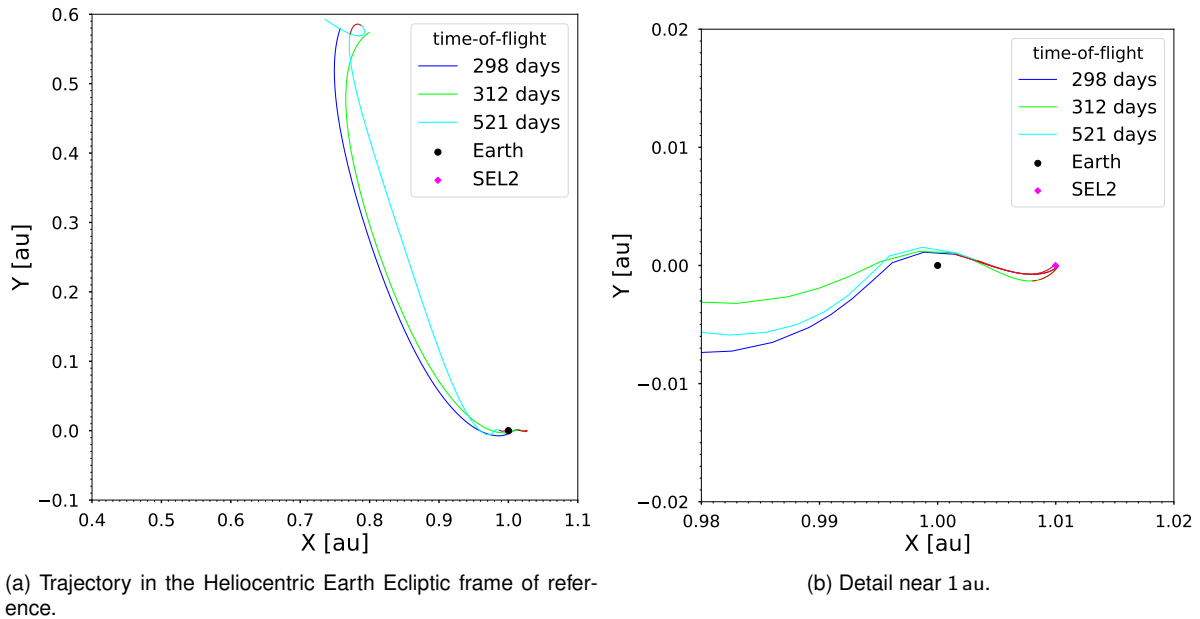


Figure 5.20: Trade study trajectories for the baseline engine (thrust arcs in red).

departure date is fixed by the initial guess, it is concluded that the trajectories are optimal or close to optimal in terms of time-of-flight (or arrival date). Further, the absence of monotonically descendent curves in Figure 5.19 is explained by the relative geometry of the departure position and comet encounter and how this geometry impacts the escape from the Earth's sphere of influence: trajectories with longer time-of-flight values might start the transfer in less favorable positions compared to shorter trajectories. In Figure 5.20a it is shown that the 521 d trajectory requires a second thrust-arc to match the comet position at the encounter. Further, in Figure 5.20b it is shown that the same trajectory requires the longest powered arc to start the interplanetary trajectory leveraging Earth's gravity. Subsequently, the 521 d trajectory, despite taking more time to reach the target, requires more propellant mass than the 312 d and 298 d trajectories. The same rationale explains why the 312 d trajectory needs less propellant than the 298 d: both trajectories only need one powered arc leaving SEL2 but the longer trajectory does so with a shorter thrust arc.

Following the analysis of the Earth's gravity on the results, a closer inquiry into the quality of the solutions of the individual trajectories was made. From it emerged a common element across the solutions: all the control profiles possessed a bang-bang feature. This feature grants at worst an indication of local optimality and at best it is an assurance of a global optimum. Another common feature across the trajectories was that the engines were not working in the optimal regime, i.e., at maximum power. Hence, an examination of the available input power impact on trajectory performance is deemed relevant.

### Increasing the Input Power

The baseline input power at 1 au to be delivered to the engine as per the CReMA specifications is 800 W. This value corresponds to 53% of the engine's maximum power. Consequently, the full potential of the engine is not leveraged: the engine's highest specific impulse is obtained when the input power is

equal to the maximum engine power. Specifically, at 800 W the specific impulse is 78 % of the maximum specific impulse obtained with 1500 W, the maximum engine power for the PPS 1350-G.

The range of values where the input power at 1 au varies is  $P_{1au} \in [800, 2700]$  W. The input power at 1 au is varied up to a value higher than the maximum engine power because the available power varies with  $P_{1au}/r^2$ : 1500 W at 1 au would not allow the engine to work at maximum power at distances  $r > 1$  au. The choice of 2700 W, allows the spacecraft to deliver the maximum engine power up to 1.3 au. The results in Figure 5.21 show the evolution of propellant mass with available input power at 1 au; the five lines in Figure 5.21 correspond to trajectories generated using different initial guesses.

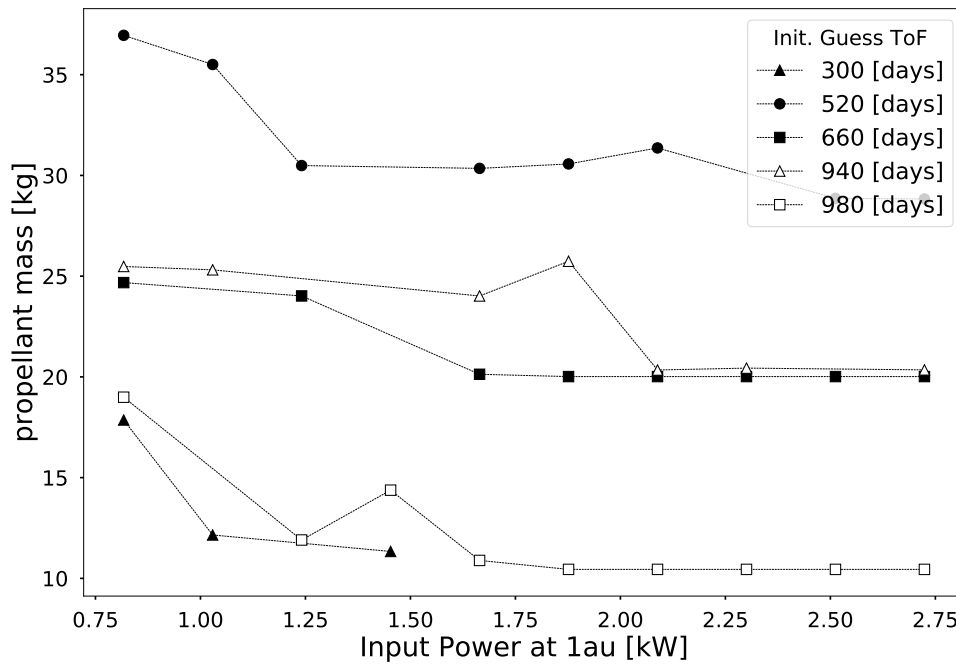


Figure 5.21: Propellant mass vs. Available input power at 1 au for different time-of-flight trajectories.

The overall trend in Figure 5.21 is of decreasing propellant mass requirements with increasing available power. Missing data points or points opposing the overall trend correspond to trajectories where the solver did not converge. Additionally, the curves asymptotically converge to a constant value: increasing the available power beyond a certain point does not carry further gains as the engine has its maximum power available for the entire trajectory. The minimum possible gain by increasing the available input power from baseline (800 W) to 1500 W is 6 kg.

## 5.4 Discussion

A few caveats that define the scope of this work must be established. Firstly, a cost analysis is not done; different propulsion systems carry different costs that vary with technology readiness level, production costs and system integration and validation processes. The long SEP maneuvers may also have an effect in the overall mission cost because Deep Space Maneuvers are typically monitored by teams in the mission's ground segment thus carrying increased personnel costs. Further, the continuous nature of low-thrust propulsion brings navigation concerns where they were not present with impulsive propulsion:

the spacecraft's GNC system has to assure the correct attitude profile for the thrust to be applied in the appropriate direction throughout the powered arcs. Hence the analysis here presented is concerned with assessing the requirements for a Comet Interceptor transfer made by a SEP system in terms of propellant mass and time-of-flight.

It should be further noted that theoretical results were not always confirmed by the numerical simulations in this work: in theory, longer trajectories are more efficient for low thrust propulsion systems; also, relaxed constraints on the system — such as more available power — should give room for increasingly optimal solutions to be found. Nevertheless, problem constraints such as departure windows and imposition of coast arcs or problem particularities such as optimal arrival dates, as seen in Figure 5.13, and peculiar departure dynamics, as observed in Figure 5.15b, blur the first order phenomena predicted theoretically and enforce the need for numerical modelling at a preliminary mission design stage to either confirm or refute theoretical results.

The fundamental question of this analysis is “Is a Solar Electric Propulsion System better for the Comet Interceptor transfer?” The answer to the question within the scope of this analysis is yes. The CReMA reference design point for SEP system delivers trajectories with higher payload mass fractions (less propellant mass) to a wider range of encounter locations — when compared to a chemical propulsion system. Figures 5.8 and 5.9, respectively, show that using SEP allows for a saving of more than 125 kg for 50 % of the encounter locations and that 75 % of the encounter locations do not require additional time-of-flight compared to CP transfers. Table 5.3 shows that the worst case scenario takes 3 additional years with EP compared to CP, if the main objective is to minimize the propellant mass. Oppositely, if the main objective is to minimize time-of-flight, the worst case scenario requires additional 50 kg to perform the transfer. However, the gains provided by EP can reach 250 kg in propellant mass savings and up to 2.6 years of time-of-flight reduction.

The savings in propellant mass are possible because SEP systems have at least twice the specific impulse of chemical propulsion systems. The baseline electric engine for the mission has a specific impulse of 1219 s whereas the chemical propulsion system was assumed to have 300 s.

Regarding the performance when reaching different encounter locations, Figures 5.2 to 5.5 show that encounter locations farther from the Earth are harder to achieve, i.e., they require more fuel mass and time-of-flight. Nonetheless, the entire range of encounter locations is reachable with less than 200 kg for 2-revolution trajectories and less than 160 kg for 3-revolution trajectories.

Additionally, increasing the available power to the engine from 800 W at 1 au to 2000 W decreases the required propellant mass (more than 15 kg for 50 % of the trajectories).

For backup targets, the results confirm if not improve the CReMA solutions. Contrarily to the CReMA, the optimization in Section 5.2 does not assume any coast-thrust-coast structure and uses the variable specific impulse polynomial engine model from LowWiz instead of a fixed thrust magnitude assumption. The difference in the approach results in a better trajectory for 0-revolution transfers in Table 5.5: the LowWiz trajectory requires 30 d less than the CReMA solution and only 1/3 of the  $\Delta v$ ; for 1-revolution trajectories in Table 5.6, no major improvements are brought by the followed approach. By including the Earth's ephemerides in the simulations, the optimizer finds solutions that leverage the Earth's gravity

field to lower the propellant mass required to reach the target, as seen in Figure 5.15.

From the two delta analysis performed on the transfer to backup targets two conclusions emerge: the XIPS and NSTAR engine reduce the required propellant mass up to 30 kg but are too heavy to provide a net mass saving on the overall propulsion system; increased available power to the engine reduces the propellant mass between 6 kg and 18 kg compared to the baseline system.



## Chapter 6

# Conclusions

The design and implementation of a Solar Electric Propulsion optimization software was carried out successfully. The software's dual implementation — toolbox and command line interface — leveraged PyGMO's Nonlinear Programming Solver SLSQP to solve Optimal Control Problems with a direct transcription method. The formulation of initial guesses for the Optimal Control Problem was automated using Chebyshev polynomials and simple algebraic relations, eliminating the need for a priori user information regarding the solution. After validation, the software was used for a preliminary analysis of the Comet Interceptor transfer to the main target and a backup target, and to perform trade studies on the backup target scenario; the toolbox was extended to deal with the particularities of the mission (unknown target) mapping each possible encounter location to a value of propellant mass and time-of-flight required to reach it.

The preliminary analysis of a Comet Interceptor transfer concluded that Solar Electric Propulsion, when compared to Chemical Propulsion, delivers trajectories that require less propellant mass. Additionally, it was shown that:

- encounter locations farther from the Earth are harder to achieve, i.e., they require more fuel mass and time-of-flight;
- a SEP system allows savings of more than 125 kg for 50 % of the comet encounter locations; 75 % of the encounter locations do not require additional time-of-flight compared to CP transfers;
- the entire range of encounter locations is reachable with less than 160 kg and a time-of-flight under 4 years for an EP system compared to 280 kg and 4.6 years with CP;
- Earth's gravity field can be leveraged when departing SEL2 to lower the propellant mass required to reach the target;
- for the backup target 73P, the XIPS and NSTAR performance gains do not compensate the additional mass associated with these systems;
- for the backup target 73P, increased available power to the engine results carries a performance gain between 6 kg and 18 kg compared to the baseline system.

## Future Work

Future work should include improved thruster modelling [59]. The software should also be extended to deal with multiple gravity assists missions such as Bepi-Colombo: this could be done by employing a hybrid optimization approach with Genetic Algorithms in an outer loop to solve the discrete problem (number and combination of gravity assists) and an inner loop (to solve for the control profile) using the gradient-based strategy already implemented in the software. Additionally, the optimization can be tweaked to take into account missed thrust scenarios [73]. Finally, implementing a sparse NLP solver would decrease computation times.

# Bibliography

- [1] M. D. Rayman and S. N. Williams. Design of the First Interplanetary Solar Electric Propulsion Mission. *Journal of Spacecraft and Rockets*, 39(4):589–595, July 2002. doi: 10.2514/2.3848.
- [2] H. Kuninaka and J. Kawaguchi. Lessons learned from round trip of Hayabusa asteroid explorer in deep space. In *2011 Aerospace Conference*, pages 1–8, Mar. 2011. ISBN 1095-323X. doi: 10.1109/AERO.2011.5747599.
- [3] D. L. Estublier. The SMART-1 Spacecraft Potential Investigations. *IEEE Transactions on Plasma Science*, 36(5):2262–2270, Oct. 2008. ISSN 1939-9375. doi: 10.1109/TPS.2008.2002032.
- [4] J. Brophy. The Dawn Ion Propulsion System. In C. Russell and C. Raymond, editors, *The Dawn Mission to Minor Planets 4 Vesta and 1 Ceres*, pages 251–261. Springer, New York, NY, 2012. ISBN 978-1-4614-4903-4. doi: 10.1007/978-1-4614-4903-4\_11.
- [5] J. Benkhoff, J. van Casteren, H. Hayakawa, M. Fujimoto, H. Laakso, M. Novara, P. Ferri, H. R. Middleton, and R. Ziethe. BepiColombo—Comprehensive exploration of Mercury: Mission overview and science goals. *Comprehensive Science Investigations of Mercury: The scientific goals of the joint ESA/JAXA mission BepiColombo*, 58(1):2–20, Jan. 2010. ISSN 0032-0633. doi: 10.1016/j.pss.2009.09.020.
- [6] H. Gray and S. Kemble. Using Electric Propulsion to get to Mercury - the BepiColombo Mission. In *43rd AIAA/ASME/SAE/ASEE Joint Propulsion Conference & Exhibit*, Joint Propulsion Conferences. American Institute of Aeronautics and Astronautics, Cincinnati, OH, July 2007. doi: 10.2514/6.2007-5229.
- [7] D. Y. Oh, J. S. Snyder, D. M. Goebel, R. R. Hofer, and T. M. Randolph. Solar Electric Propulsion for Discovery-Class Missions. *Journal of Spacecraft and Rockets*, 51(6):1822–1835, Oct. 2014. doi: 10.2514/1.A32889.
- [8] S. Kemble. *Interplanetary Mission Analysis and Design*. Number 2365-9599 in Astronautical Engineering. Springer-Verlag Berlin Heidelberg, 1 edition, 2006. ISBN 978-3-662-50022-4.
- [9] B. A. Conway, editor. *Spacecraft Trajectory Optimization*. Cambridge Aerospace Series. Cambridge University Press, Cambridge, 2010. ISBN 978-0-521-51850-5. doi: 10.1017/CBO9780511778025.

- [10] B. J. Wall and B. A. Conway. Genetic algorithms applied to the solution of hybrid optimal control problems in astrodynamics. *Journal of Global Optimization*, 44(4):493, Sept. 2008. ISSN 1573-2916. doi: 10.1007/s10898-008-9352-4.
- [11] M. D. Rayman, P. Varghese, D. H. Lehman, and L. L. Livesay. Results from the Deep Space 1 technology validation mission. *Space an Integral Part of the Information Age*, 47(2):475–487, July 2000. ISSN 0094-5765. doi: 10.1016/S0094-5765(00)00087-4.
- [12] J. T. Betts. Survey of Numerical Methods for Trajectory Optimization. *Journal of Guidance, Control, and Dynamics*, 21(2):193–207, Mar. 1998. doi: 10.2514/2.4231.
- [13] F. Topputo and C. Zhang. Survey of Direct Transcription for Low-Thrust Space Trajectory Optimization with Applications. *Abstract and Applied Analysis*, 2014:1–15, June 2014. doi: 10.1155/2014/851720.
- [14] A. Shirazi, J. Ceberio, and J. A. Lozano. Spacecraft trajectory optimization: A review of models, objectives, approaches and solutions. *Progress in Aerospace Sciences*, 102:76–98, Oct. 2018. ISSN 0376-0421. doi: 10.1016/j.paerosci.2018.07.007.
- [15] D. Izzo, M. Märtens, and B. Pan. A survey on artificial intelligence trends in spacecraft guidance dynamics and control. *Astrodynamics*, 3(4):287–299, Dec. 2019. ISSN 2522-0098. doi: 10.1007/s42064-018-0053-6.
- [16] R. Chai, A. Savvaris, A. Tsourdos, and S. Chai. Overview of Trajectory Optimization Techniques. In *Design of Trajectory Optimization Approach for Space Maneuver Vehicle Skip Entry Problems*, pages 7–25. Springer, Singapore, Jan. 2020. ISBN 978-981-13-9844-5. doi: 10.1007/978-981-13-9845-2.2.
- [17] S. Gong and M. Macdonald. Review on solar sail technology. *Astrodynamics*, 3(2):93–125, June 2019. ISSN 2522-0098. doi: 10.1007/s42064-019-0038-x.
- [18] T. N. Edelbaum. Propulsion Requirements for Controllable Satellites. *ARS Journal*, 31(8):1079–1089, Aug. 1961. doi: 10.2514/8.5723.
- [19] F. W. Boltz. Orbital motion under continuous radial thrust. *Journal of Guidance, Control, and Dynamics*, 14(3):667–670, May 1991. doi: 10.2514/3.20690.
- [20] J. A. Kechichian. Reformulation of Edelbaum’s Low-Thrust Transfer Problem Using Optimal Control Theory. *Journal of Guidance, Control, and Dynamics*, 20(5):988–994, Sept. 1997. doi: 10.2514/2.4145.
- [21] Y. Gao and C. A. Kluever. Analytic Orbital Averaging Technique for Computing Tangential-Thrust Trajectories. *Journal of Guidance, Control, and Dynamics*, 28(6):1320–1323, Nov. 2005. doi: 10.2514/1.14698.
- [22] A. E. Bryson and Y.-C. Ho. *Applied Optimal Control : Optimization, Estimation, and Control*. Taylor & Francis Group, New York, NY, 1975. ISBN 0-89116-228-3.

- [23] R. P. Russell. Primer Vector Theory Applied to Global Low-Thrust Trade Studies. *Journal of Guidance, Control, and Dynamics*, 30(2):460–472, Mar. 2007. doi: 10.2514/1.22984.
- [24] A. Petropoulos and R. Russell. Low-Thrust Transfers Using Primer Vector Theory and a Second-Order Penalty Method. In *AIAA/AAS Astrodynamics Specialist Conference and Exhibit*, Guidance, Navigation, and Control and Co-located Conferences. American Institute of Aeronautics and Astronautics, Aug. 2008. doi: 10.2514/6.2008-6955.
- [25] E. Taheri, N. I. Li, and I. Kolmanovsky. Co-state initialization for the minimum-time low-thrust trajectory optimization. *Advances in Space Research*, 59(9):2360–2373, May 2017. ISSN 0273-1177. doi: 10.1016/j.asr.2017.02.010.
- [26] C. L. Ranieri and C. A. Ocampo. Indirect Optimization of Spiral Trajectories. *Journal of Guidance, Control, and Dynamics*, 29(6):1360–1366, Nov. 2006. doi: 10.2514/1.19539.
- [27] Z. Zhu, Q. Gan, X. Yang, and Y. Gao. Solving fuel-optimal low-thrust orbital transfers with bang-bang control using a novel continuation technique. *Acta Astronautica*, 137:98–113, Aug. 2017. ISSN 0094-5765. doi: 10.1016/j.actaastro.2017.03.032.
- [28] M. Diehl, H. Bock, H. Diedam, and P.-B. Wieber. Fast Direct Multiple Shooting Algorithms for Optimal Robot Control. In M. Diehl and K. Mombaur, editors, *Fast Motions in Biomechanics and Robotics: Optimization and Feedback Control*, pages 65–93. Springer, Berlin, Heidelberg, 2006. ISBN 978-3-540-36119-0. doi: 10.1007/978-3-540-36119-0\_4.
- [29] J. Sims and S. Flanagan. Preliminary Design of Low-Thrust Interplanetary Missions. In *Astrodynamics 1999: proceedings of the AAS/AIAA Astrodynamics Conference*, volume 103, Girdwood, AK, 2000. Univelt. ISBN 0-87703-467-2.
- [30] J. Sims, P. Finlayson, E. Rinderle, M. Vavrina, and T. Kowalkowski. Implementation of a Low-Thrust Trajectory Optimization Algorithm for Preliminary Design. In *AIAA/AAS Astrodynamics Specialist Conference and Exhibit*, Guidance, Navigation, and Control and Co-located Conferences. American Institute of Aeronautics and Astronautics, Aug. 2006. doi: 10.2514/6.2006-6746.
- [31] R. Beeson, J. Englander, S. Hughes, and M. Schadeegg. An Automatic Medium To High Fidelity Low-Thrust Global Trajectory Tool-Chain; EMTG-GMAT. In *Spaceflight Mechanics 2015: Proceedings of the 25th AAS/AIAA Space Flight Mechanics Meeting*, Williamsburg, VA, Jan. 2015. Univel. ISBN 0-87703-623-3.
- [32] J. A. Englander and B. A. Conway. Automated Solution of the Low-Thrust Interplanetary Trajectory Problem. *Journal of Guidance, Control, and Dynamics*, 40(1):15–27, Sept. 2016. doi: 10.2514/1.G002124.
- [33] T. T. McConaghy, T. J. Debban, A. E. Petropoulos, and J. M. Longuski. Design and Optimization of Low-Thrust Trajectories with Gravity Assists. *Journal of Spacecraft and Rockets*, 40(3):380–387, May 2003. ISSN 0022-4650. doi: 10.2514/2.3973.

- [34] C. H. Yam, D. Izzo, and F. Biscani. Towards a High Fidelity Direct Transcription Method for Optimisation of Low-Thrust Trajectories. In *Astrodynamics Beyond Borders*, pages 1–7, Madrid, Spain, 2010. European Space Agency.
- [35] A. Mereta and D. Izzo. Target selection for a small low-thrust mission to near-Earth asteroids. *Astrodynamics*, 2(3):249–263, Sept. 2018. ISSN 2522-0098. doi: 10.1007/s42064-018-0024-y.
- [36] J. T. Betts. *Practical Methods for Optimal Control and Estimation Using Nonlinear Programming*. Advances in Design and Control. Society for Industrial and Applied Mathematics, Philadelphia, PA, Jan. 2010. ISBN 978-0-89871-688-7. doi: 10.1137/1.9780898718577.
- [37] J. Englander, B. Conway, and T. Williams. *Automated Interplanetary Mission Planning*. Aug. 2012. doi: 10.2514/5.9781624102714.0669.0706.
- [38] C. M. Chilan and B. A. Conway. Automated Design of Multiphase Space Missions Using Hybrid Optimal Control. *Journal of Guidance, Control, and Dynamics*, 36(5):1410–1424, June 2013. doi: 10.2514/1.58766.
- [39] S. A. Wagner. *Automated trajectory design for impulsive and low thrust interplanetary mission analysis*. PhD thesis, Iowa State University, 2014.
- [40] R. Chai, A. Savvaris, A. Tsourdos, S. Chai, and Y. Xia. A review of optimization techniques in spacecraft flight trajectory design. *Progress in Aerospace Sciences*, 109, Aug. 2019. ISSN 0376-0421. doi: 10.1016/j.paerosci.2019.05.003.
- [41] A. E. Petropoulos and J. M. Longuski. Shape-Based Algorithm for the Automated Design of Low-Thrust, Gravity Assist Trajectories. *Journal of Spacecraft and Rockets*, 41(5):787–796, Sept. 2004. doi: 10.2514/1.13095.
- [42] B. J. Wall and B. A. Conway. Shape-Based Approach to Low-Thrust Rendezvous Trajectory Design. *Journal of Guidance, Control, and Dynamics*, 32(1):95–101, Jan. 2009. doi: 10.2514/1.36848.
- [43] D. M. Novak and M. Vasile. Improved Shaping Approach to the Preliminary Design of Low-Thrust Trajectories. *Journal of Guidance, Control, and Dynamics*, 34(1):128–147, Jan. 2011. doi: 10.2514/1.50434.
- [44] D. J. Gondelach and R. Noomen. Hodographic-Shaping Method for Low-Thrust Interplanetary Trajectory Design. *Journal of Spacecraft and Rockets*, 52(3):728–738, Feb. 2015. doi: 10.2514/1.A32991.
- [45] E. Taheri and O. Abdelkhalik. Shape Based Approximation of Constrained Low-Thrust Space Trajectories using Fourier Series. *Journal of Spacecraft and Rockets*, 49(3):535–546, May 2012. doi: 10.2514/1.58789.
- [46] O. Abdelkhalik and E. Taheri. Approximate On-Off Low-Thrust Space Trajectories Using Fourier Series. *Journal of Spacecraft and Rockets*, 49(5):962–965, Sept. 2012. doi: 10.2514/1.A32307.

- [47] E. Taheri and O. Abdelkhalik. Initial Three-Dimensional Low-Thrust Trajectory Design. *Advances in Space Research*, 57, Dec. 2015. doi: 10.1016/j.asr.2015.11.034.
- [48] P. Patel. *Automating Interplanetary Trajectory Generation for Electric Propulsion Trade Studies*. PhD Thesis, University of Michigan, Jan. 2008.
- [49] P. Patel, A. D. Gallimore, T. H. Zurbuchen, and D. J. Scheeres. An Algorithm for Generating Feasible Low Thrust Interplanetary Trajectories. In *Proceedings of the 31st International Electric Propulsion Conference*, Ann Arbor, Michigan, 2009.
- [50] J. P. Boyd. *Chebyshev and Fourier Spectral Methods*. Dover Books on Mathematics. Dover Publications, Inc, Michigan, second edition edition, 2000. ISBN 978-0-486-41183-5.
- [51] C. Snodgrass and G. H. Jones. The European Space Agency's Comet Interceptor lies in wait. *Nature Communications*, 10(1):5418, Nov. 2019. ISSN 2041-1723. doi: 10.1038/s41467-019-13470-1.
- [52] H. U. Keller and E. Kührt. Cometary Nuclei—From Giotto to Rosetta. *Space Science Reviews*, 216(1):14, Jan. 2020. ISSN 1572-9672. doi: 10.1007/s11214-020-0634-6.
- [53] M. A. Barucci and M. Fulchignoni. Major achievements of the Rosetta mission in connection with the origin of the solar system. *The Astronomy and Astrophysics Review*, 25(1):3, Oct. 2017. ISSN 1432-0754. doi: 10.1007/s00159-017-0103-8.
- [54] M. Mumma, P. Weissman, and S. Stern. Comets and the origin of the solar system - Reading the Rosetta Stone. *Protostars and Planets III*, Feb. 1993.
- [55] M. E. Schwamb, M. M. Knight, G. H. Jones, C. Snodgrass, L. Bucci, J. M. S. Perez, and N. Skuppin. Potential Backup Targets for Comet Interceptor. *Research Notes of the AAS*, 4(2), 2020. doi: 10.3847/2515-5172/ab7300.
- [56] C. Koppel, F. Marchandise, D. Estublier, and L. Jolivet. The Smart-1 Electric Propulsion Subsystem In Flight Experience. In *40th AIAA/ASME/SAE/ASEE Joint Propulsion Conference and Exhibit*, Joint Propulsion Conferences. American Institute of Aeronautics and Astronautics, Fort Lauderdale, FL, July 2004. doi: 10.2514/6.2004-3435.
- [57] R. Jahn. *Physics of Electric Propulsion*. McGraw-Hill Series in Missile and Space Technology. McGraw-Hill, 2006. ISBN 978-0-486-45040-7.
- [58] C. D. Child. Discharge From Hot CaO. *Physical Review (Series I)*, 32(5):492–511, May 1911. doi: 10.1103/PhysRevSeriesI.32.492.
- [59] J. Knittel, J. Englander, M. Ozimek, J. Atchison, and J. Gould. Improved Propulsion Modeling for Low-Thrust Trajectory Optimization. In 7, volume 160 of *Advances in the Astronautical Sciences*, page 4290, San Antonio, TX, Feb. 2017. Univelt. ISBN 978-0-87703-637-1.

- [60] D. Y. Oh. Evaluation of Solar Electric Propulsion Technologies for Discovery-Class Missions. *Journal of Spacecraft and Rockets*, 44(2):399–411, Mar. 2007. doi: 10.2514/1.21613.
- [61] C. R. Harris, K. J. Millman, S. J. v. d. Walt, R. Gommers, P. Virtanen, D. Cournapeau, E. Wieser, J. Taylor, S. Berg, N. J. Smith, R. Kern, M. Picus, S. Hoyer, M. H. v. Kerkwijk, M. Brett, A. Haldane, J. F. d. R'io, M. Wiebe, P. Peterson, P. G'erard-Marchant, K. Sheppard, T. Reddy, W. Weckesser, H. Abbasi, C. Gohlke, and T. E. Oliphant. Array programming with NumPy. *Nature*, 585(7825): 357–362, Sept. 2020. doi: 10.1038/s41586-020-2649-2.
- [62] S. K. Lam, A. Pitrou, and S. Seibert. Numba: A LLVM-Based Python JIT Compiler. In *Proceedings of the Second Workshop on the LLVM Compiler Infrastructure in HPC*, LLVM '15, New York, NY, USA, 2015. Association for Computing Machinery. ISBN 978-1-4503-4005-2. doi: 10.1145/2833157.2833162.
- [63] J. D. Hunter. Matplotlib: A 2D graphics environment. *Computing in Science & Engineering*, 9(3): 90–95, 2007. doi: 10.1109/MCSE.2007.55.
- [64] D. Izzo. *esa/pykep: The Gym and more.*, Dec. 2019.
- [65] A. M. Annex, B. Pearson, B. Seignovert, B. T. Carcich, H. Eichhorn, J. A. Mapel, J. L. F. v. Forstner, J. McAuliffe, J. D. d. Rio, K. L. Berry, K.-M. Aye, M. Stefko, M. d. Val-Borro, S. Kulumani, and S.-y. Murakami. Spicypy: a Pythonic Wrapper for the SPICE Toolkit. *Journal of Open Source Software*, 5(46):2050, 2020. doi: 10.21105/joss.02050.
- [66] C. H. Acton. Ancillary data services of NASA's Navigation and Ancillary Information Facility. *Planetary data system*, 44(1):65–70, Jan. 1996. ISSN 0032-0633. doi: 10.1016/0032-0633(95)00107-7.
- [67] C. Acton, N. Bachman, B. Semenov, and E. Wright. A look towards the future in the handling of space science mission geometry. *Enabling Open and Interoperable Access to Planetary Science and Heliophysics Databases and Tools*, 150:9–12, Jan. 2018. ISSN 0032-0633. doi: 10.1016/j.pss.2017.02.013.
- [68] F. Biscani and D. Izzo. A parallel global multiobjective framework for optimization: pagmo. *Journal of Open Source Software*, 5(53):2338, 2020. doi: 10.21105/joss.02338.
- [69] D. Kraft. A software package for sequential quadratic programming. Technical, Oberpfaffenhofen, 1988.
- [70] J. Atchison, M. Ozimek, B. Kantsiper, and A. Cheng. Trajectory Options for the DART Mission. *Acta Astronautica*, 123, Apr. 2016. doi: 10.1016/j.actaastro.2016.03.032.
- [71] J. R. Wertz and W. J. Larson, editors. *Space Mission Analysis and Design*. Space Technology Library. Microcosm and Kluwer Academic Publishers, El Segundo, CA, 3rd edition, 1999. ISBN 978-0-7923-5901-2 978-1-881883-10-4.

- [72] D. M. Goebel, J. E. Polk, I. Sandler, I. G. Mikellides, J. R. Brophy, W. G. Tighe, and K.-R. Chien. Evaluation of 25-cm XIPS thruster life for deep space mission applications. In *Proceedings of the 31st International Electric Propulsion Conference*, Ann Arbor, Michigan, 2009.
- [73] C. Venigalla and D. Scheeres. Low-Thrust Trajectory Optimization for Maximum Missed Thrust Recovery Margin. Aug. 2020.
- [74] D. Oh and D. Goebel. Performance Evaluation of an Expanded Range XIPS Ion Thruster System for NASA Science Missions. In *42nd AIAA/ASME/SAE/ASEE Joint Propulsion Conference & Exhibit*, Joint Propulsion Conferences, Sacramento, CA, July 2006. American Institute of Aeronautics and Astronautics. ISBN 978-1-62410-038-3. doi: 10.2514/6.2006-4466.
- [75] R. Hofer. High-Specific Impulse Operation of the BPT-4000 Hall Thruster for NASA Science Missions. In *46th AIAA/ASME/SAE/ASEE Joint Propulsion Conference & Exhibit*, Joint Propulsion Conferences, Nashville, TN, July 2010. American Institute of Aeronautics and Astronautics. doi: 10.2514/6.2010-6623.



# Appendix A

## Trajectory Optimization Mode outputs

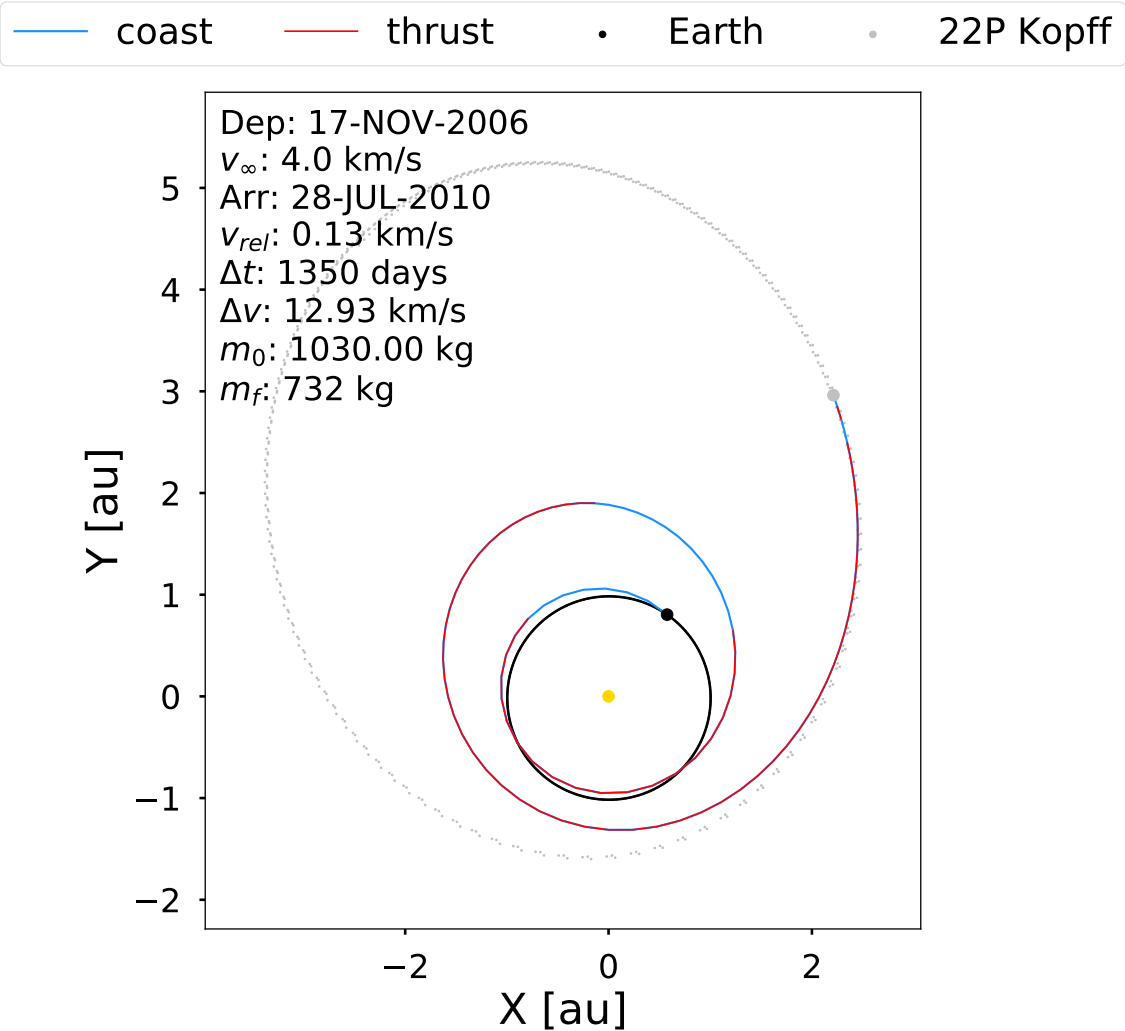


Figure A.1: Earth to Kopff transfer.

Dep: 17-NOV-2006  
 $v_{\infty}$ : 4.0 km/s  
 Arr: 28-JUL-2010  
 $v_{rel}$ : 0.13 km/s  
 $\Delta t$ : 1350 days  
 $\Delta v$ : 12.93 km/s  
 $m_0$ : 1030.00 kg  
 $m_f$ : 732 kg

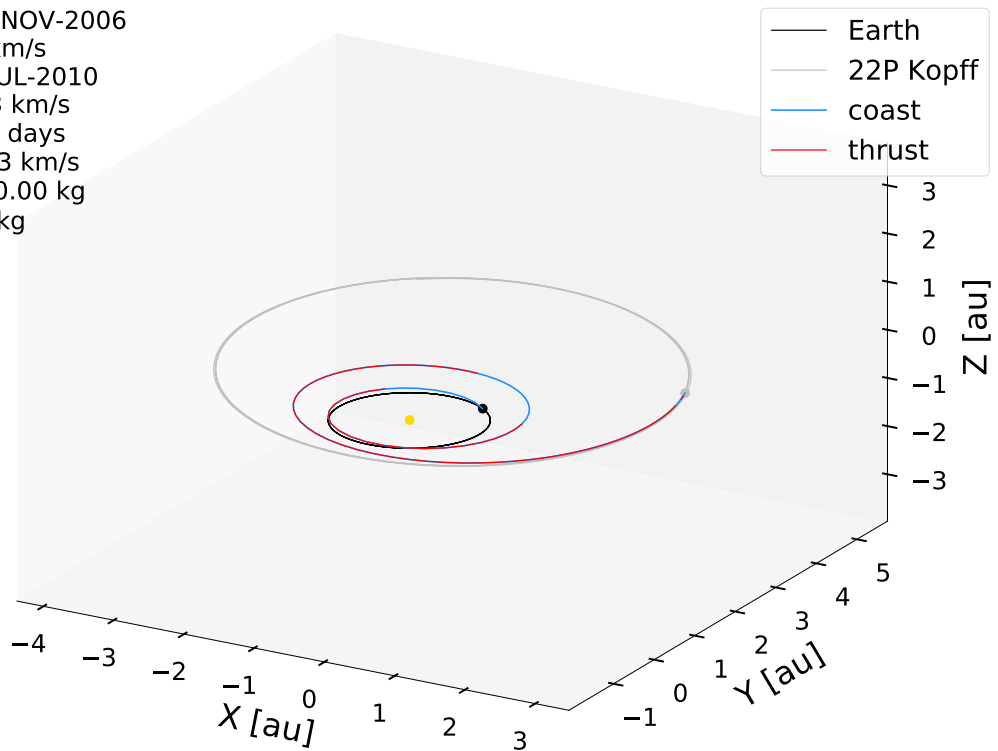


Figure A.2: Earth to Kopff transfer (3D).

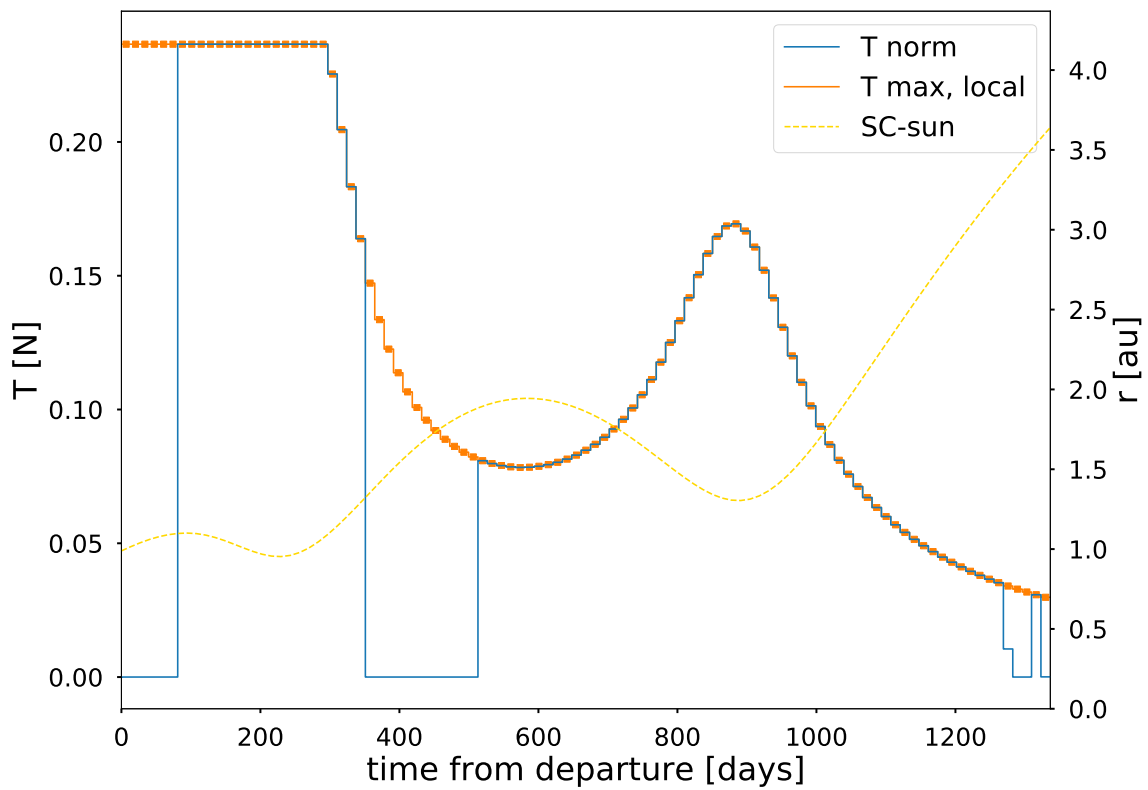


Figure A.3: Control profile for a transfer to Kopff.

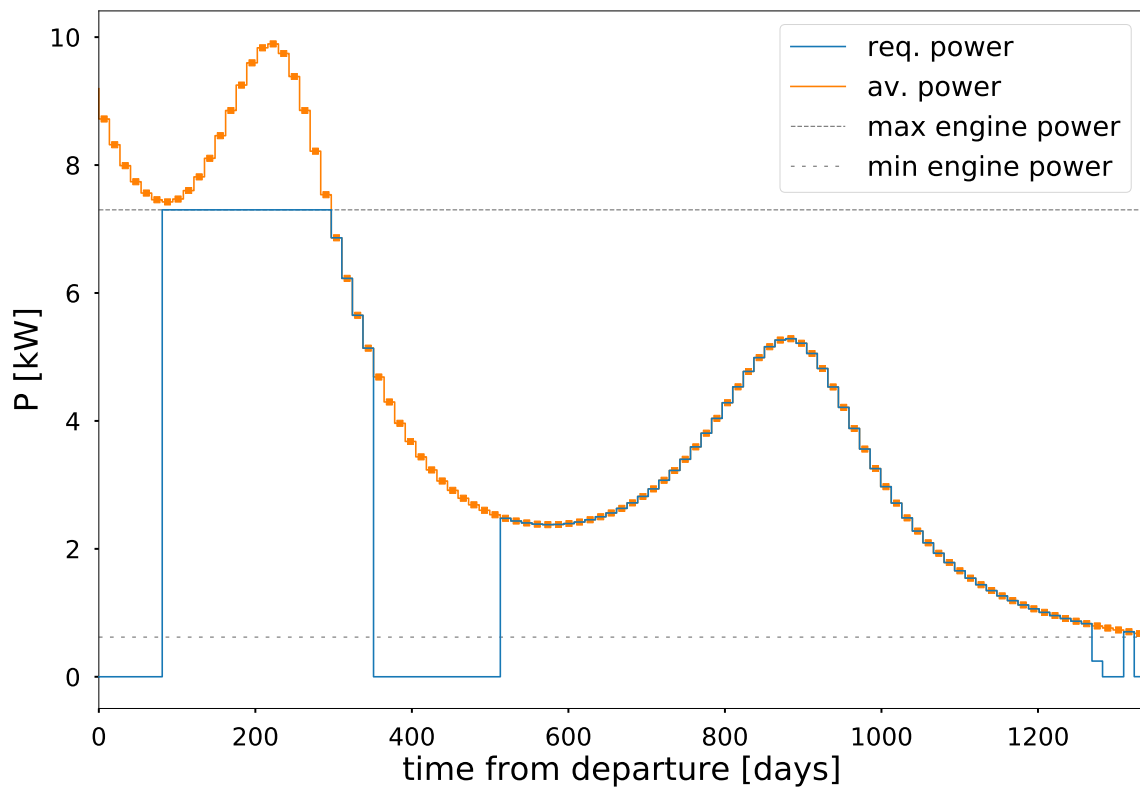
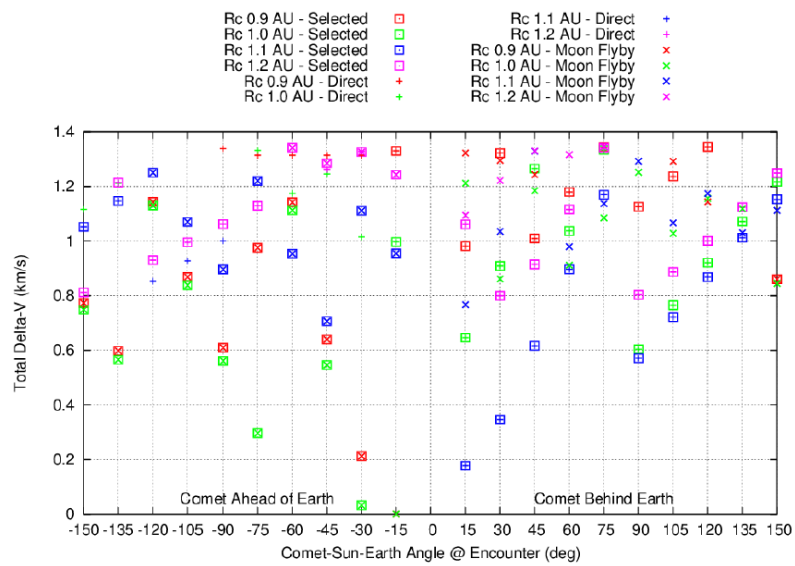


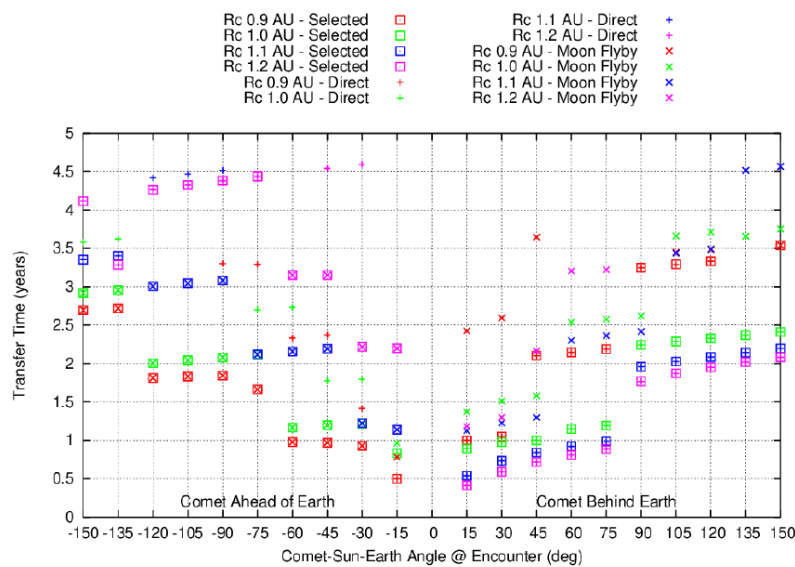
Figure A.4: Required power profile for a transfer to Kopff.

# Appendix B

## CReMA data

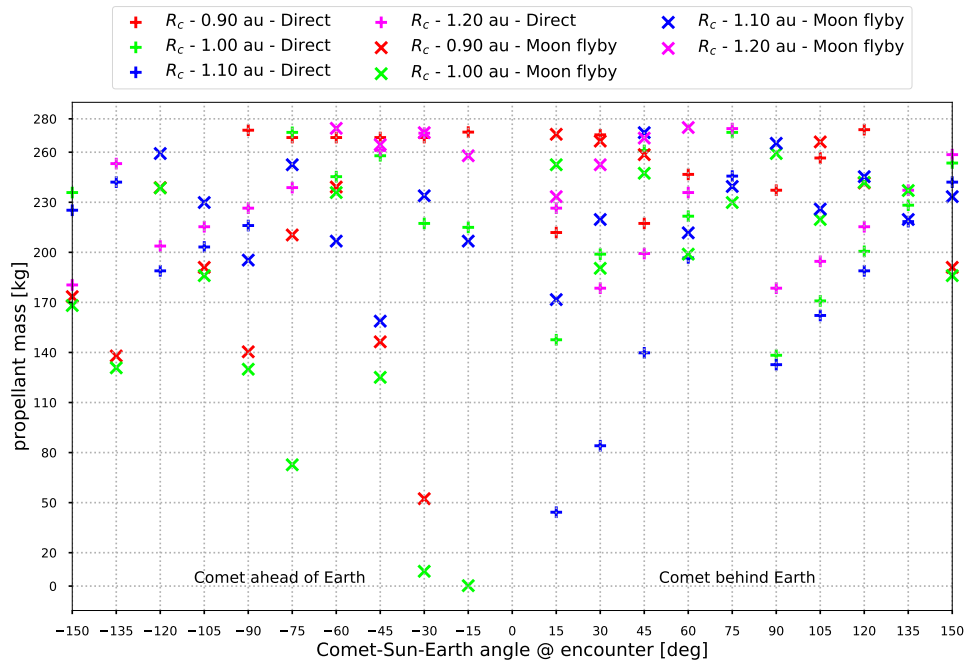


(a) Impulsive  $\Delta v$ .

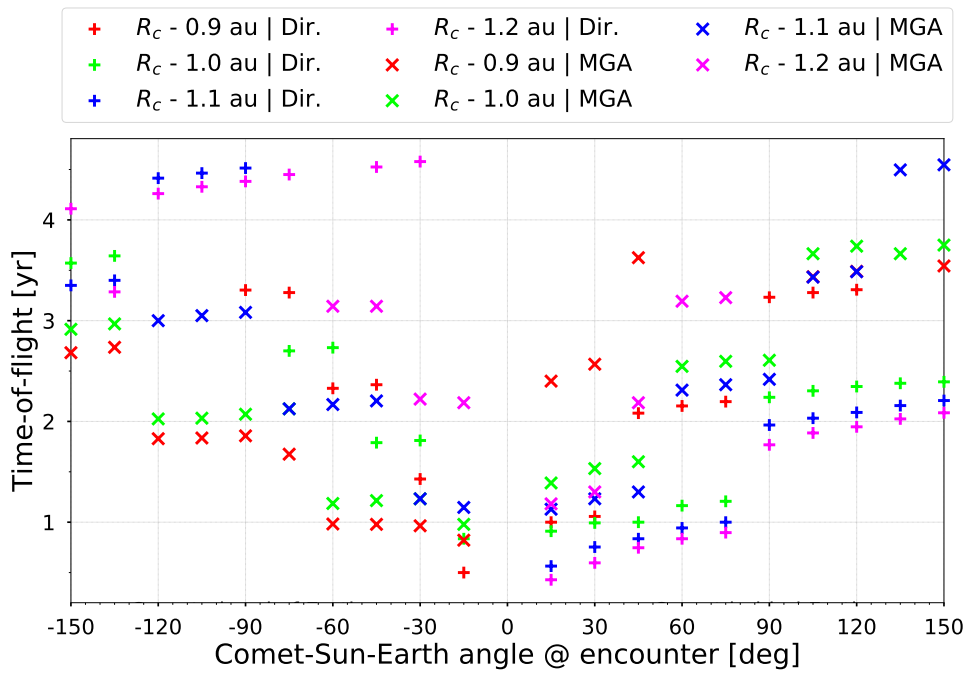


(b) Time-of-flight.

Figure B.1: Selected CP transfers.



(a) Selected CP trajectories. Data extrapolated from the CReMA.



(b) Time-of-flight.

Figure B.2: Selected CP transfers. Data from the CReMA. Dir are direct transfers; MGA are Moon Gravity Assist transfers.

# Appendix C

## Coefficients for the Engine Models

Table C.1: Engine Model Coefficients: Mass Flow

Engine	$c_{m,0}$	$c_{m,1}$	$c_{m,2}$	$c_{m,3}$	$c_{m,4}$	Source
NEXT	1.944	0.1768	-0.1898	0.076 37	-0.006 02	[60]
NSTAR	0.3594	1.5665	-0.5941	0.157 74	-0.016 47	[60]
XIPS	0.8211	0.0426	0.5402	-0.1219	0.0091	[74]
BPT-4000	1.653 105	1.998 082	1.328 508	-0.727 280	0.086 106	[75]
PPS 1350-G	1.935	2.545	-0.3716	-	-	[56]

Table C.2: Engine Model Coefficients: Thrust

Engine	$c_{t,0}$	$c_{t,1}$	$c_{t,2}$	$c_{t,3}$	$c_{t,4}$	Source
NEXT	-0.089 54	52.32	-14.02	2.926	-0.1889	[60]
NSTAR	-2.2822	38.4804	0.082 67	-1.554	0.2340	[60]
XIPS	-0.3984	35.3591	1.4111	-0.4966	0.0367	[74]
BPT-4000	-1.454 064	47.927 765	19.422 224	-10.102 479	1.174 296	[75]
PPS 1350-G	4.68	60.94	-5.10	-	-	[56]

Table C.3: Engine Model: Minimum and Maximum Power

Engine	$P_{min}$ (kW)	$P_{max}$ (kW)	Source
NEXT	0.620	7.3	[60]
NSTAR	0.450	3.8	[60]
XIPS	0.436	5.03	[74]
BPT-4000	0.302	4.839	[75]
PPS 1350-G	0.46	1.5	[56]